UCLA
UCLA Electronic Theses and Dissertations

Title
Passenger Exposures to Ultrafine Particles and In-cabin Air Quality Control

Permalink
https://escholarship.org/uc/item/1jx30578

Author
Lee, Eon Song

Publication Date
2013

Peer reviewed|Thesis/dissertation

eScholarship.org Powered by the California Digital Library
University of California

UNIVERSITY OF CALIFORNIA

Los Angeles

Passenger Exposures to Ultrafine Particles and In-cabin Air Quality Control

A dissertation submitted in partial satisfaction of the requirements for the degree Doctor of Philosophy in Civil Engineering

by

Eon Song Lee

2013

© Copyright by

Eon Song Lee

2013

ABSTRACT OF THE DISSERTATION

Passenger Exposures to Ultrafine Particles

and In-cabin Air Quality Control

by

Eon Song Lee

Doctor of Philosophy in Civil Engineering

University of California, Los Angeles, 2013

Professor Yifang Zhu, Co-Chair

Professor Michael K. Stenstrom, Co-Chair

Ultrafine particles (UFPs, diameter $\leq$ 100nm) have been a significant health concern because of their adverse health effects. Since UFPs primarily origin from traffic emissions in urban environment, previous research efforts have dedicated to study UFPs in near-freeway and on-freeway environments. Despite improved understanding of UFPs in last two decades, UFPs in the in-cabin environment, whereby passenger exposures occur, has been largely overlooked.

Although modern passenger vehicles are commonly equipped with cabin air filters, in-cabin UFP reduction is low (i.e., 40-60%) in outdoor air (OA) mode and commuting exposure

alone can account for a significant level of total daily exposure (i.e., up to 45-50%). Although setting the ventilation system to recirculation (RC) mode can reduce in-cabin UFPs by 80-95%, carbon dioxide (CO_2) from the exhaled breath of passengers can quickly accumulate in the passenger cabin.

In order to reduce passenger exposures to UFPs and CO_2, this dissertation work investigated the in-cabin environment experimentally and quantitatively. From experimental measurements, this work quantified automotive envelope leakage and ventilation systems across a wide range of vehicle models / types from various manufacturers. The infiltration was found specific to location and also conditionally occurred as a result of two competing pressures: in-cabin pressure and aerodynamic pressure on vehicle envelope. The aerodynamic pressure also changed as a function of driving speed. To extend the findings, this dissertation work developed a quantitative model to simulate in-cabin air quality and evaluated the effects of infiltration and passive ventilation in wide range of driving speed and ventilation conditions. Parametric analysis using the model elucidated the fractional significance of in-cabin UFP gain/loss mechanisms affected by driving speed. Finally, the dissertation work proposed a novel simultaneous control method and demonstrated in-cabin concentration reduction of 93% on average for UFPs in filed conditions while reducing CO_2 level by a factor of 3-4.

The dissertation of Eon Song Lee is approved.

Keith D. Stolzenbach

Jennifer A. Jay

Yifang Zhu, Committee Co-Chair

Michael K. Stenstrom, Committee Co-Chair

University of California, Los Angeles

2013

To

my parents, parents-in-law

and

my beloved wife, Hyunjung Kwon

TABLE OF CONTENTS

TABLE OF CONTENTS vi
LIST OF FIGURES viii
ACKNOWLEDGMENTS xi
VITA xiii
PUBLICATIONS xiii
PRESENTATIONS xiv

1. INTRODUCTION 1
    1.1. Passenger Exposures to Ultrafine Particles 1
    1.2. Background and Motivation 3
    1.3. Objectives 6
    1.4. Organization of the Dissertation 6
    References 8

2. IN-CABIN ULTRAFINE PARTICLE INFILTRATION 12
    2.1. Abstract 12
    2.2. Introduction 13
    2.3. Methods 16
        2.3.1. Vehicle Selections and Quartile Fan Settings 16
        2.3.2. Instrumentation 17
        2.3.3. Stationary Measurements 19
        2.3.4. Mobile Measurements 21
        2.3.5. Analytical 23
    2.4. Results and Discussion 25
        2.4.1. Variability in the Mechanical Ventilation Systems 25
        2.4.2. Leakage Function and Equivalent Leakage Area 27
        2.4.3. Aerodynamic Differential Pressure Changes on Moving Vehicles 32
        2.4.4. Ultrafine Particle Infiltration under the Mobile Condition 35
    References 41

3. IN-CABIN ULTRAFINE PARTICLE TRANSPORT 43
    3.1. Abstract 43
    3.2. Introduction 44

3.3. Methods 46
3.3.1. In-cabin Ultrafine Particle Gain / Loss Mechanisms 46
3.3.2. Model Development 47
3.3.3. Modeling Assumptions 49
3.3.4. Driving-speed-dependent Sub-models 50
3.3.5. Model Calibration 54
3.3.6. Validation Data Collection 55
3.4. Results and Discussion 57
3.4.1. Model Validation 57
3.4.2. Recirculation Mode Air Exchange Rates 61
3.4.3. Infiltration with Different Fan Setting and Driving Speed 63
3.4.4. Fractional Impact by Different Mechanisms 68
References 75

4. APPLICATION OF HIGH EFFICIENCY AIR FILTER 78
4.1. Abstract 78
4.2. Introduction 79
4.3. Methods 80
4.3.1. Automotive Cabin HEPA Filters 80
4.3.2. Test Vehicle Selections 85
4.3.3. Field Measurements 86
4.4. Results and Discussion 87
4.4.1. Particle Size Distributions under Different Conditions 87
4.4.2. In-cabin Reduction for UFPs, Black Carbon, and $PM_{2.5}$ 89
4.4.3. Ventilation Air-flow Rate Reduction 94
4.4.4. Size-resolved In-cabin UFP Reduction 96
4.4.5. In-cabin Reduction of Nucleation Mode Particles 98
4.4.6. Simultaneous Control of In-cabin UFPs and CO_2 100
References 103

5. CONCLUSIONS 105

APPENDICES 107

LIST OF FIGURES

Figure 2.1 Graphical illustrations of the in-cabin air flow path..... 18
Figure 2.2 Variability of mechanical ventilation air-flow rates and the associated differential pressures across different vehicle models 26
Figure 2.3 Automotive envelope leakage functions derived from the measurements of ventilation inlet air flow rate and corresponding differential pressure 28
Figure 2.4 Linear correlations of outdoor air mode air exchange rates and equivalent leakage areas 30
Figure 2.5 Aerodynamic differential pressure changes as a function of the driving speed 33
Figure 2.6 Observation of ultrafine particle infiltration in recirculation mode 36
Figure 2.7 Observation of ultrafine particle infiltration in outdoor air mode..... 39
Figure 3.1 Graphical illustrations of the modeling domain and modeling parameters. 47
Figure 3.2 Linear function of passive ventilation air exchange rates with respect to driving speed..... 53
Figure 3.3 Empirical validation results of the proposed model for UFPs and CO_2..... 57
Figure 3.4 Concentration sensitivity of the proposed model for UFPs and CO_2..... 59
Figure 3.5 Model bias weighted by frequency distributions of the in-cabin measurements..... 59
Figure 3.6 Recirculation mode air exchange rates as a function of driving speed 60
Figure 3.7 Differential pressure changes as a function of speed at given ventilation air-flow rates..... 64
Figure 3.8 Ultrafine particle I/O ratio as a function of driving speed..... 65
Figure 3.9 Changes of fractional impacts of in-cabin particle gain/loss mechanisms in outdoor air mode as a function of driving speed..... 69
Figure 3.10 Changes of fractional impacts of in-cabin particle gain/loss mechanisms in recirculation mode as a function of driving speed 72
Figure 4.1 Scanning electron microscope (SEM) image of HEPA A filter..... 81
Figure 4.2 Scanning electron microscope (SEM) image of HEPA B filter..... 82
Figure 4.3 Lab testing results of the particle size-specific filtration efficiency of HEPA A filter 83
Figure 4.4 Lab testing results of the particle size-specific filtration efficiency of HEPA B filter 84
Figure 4.5 Particle size distributions for the on-road and in-cabin environments with

different filter types..... 88
Figure 4.6 In-cabin particle concentration reductions with different filters and driving conditions..... 89
Figure 4.7 In-cabin ultrafine particle reductions and the changes in ventilation air-flow rates..... 94
Figure 4.8 Size-specific particle removal efficiency of the four different filter types.. 96
Figure 4.9 Size-resolved ultrafine particle number concentration changes in time series contour..... 99
Figure 4.10 Simultaneous reduction of the in-cabin ultrafine particles and carbon dioxide..... 100

LIST OF TABLES

Table 2.1 A summary of the test vehicle models and specifications 17
Table 3.1 A summary of the modeling equations for particle and gas under different ventilation modes 49
Table 3.2 A summary of the test vehicle models and specifications 55
Table 4.1 A summary of the test vehicle models and specifications 85
Table 4.2 A summary of the in-cabin concentration reductions for UFP, BC, and $PM_{2.5}$ 93

ACKNOWLEDGMENTS

I would like to express my deepest gratitude to my two advisors Prof. Michael K. Stenstrom and Prof. Yifang Zhu for their guidance, support and encouragement throughout my Ph.D. study. It was my great privilege to learn academically and non-academically from both exceptional scholars during my doctoral research at UCLA. I would also like to appreciate two other professors at UCLA: Prof. Keith D. Stolzenbach and Prof. Jennifer A. Jay for their time, support, and service in my Ph.D. committee. What they have taught me became strong fundamentals for this Ph.D. work.

I wish to extend my appreciation to my former professors at the University of Texas at Austin: Richard Corsi, Jeffrey Siegel, and Atila Novoselac who trained me with great motivation and desire for air quality research.

I gratefully acknowledge my co-workers David Fung, Nu Yu, David Quiros, Zoe Zhang, and Bin Xu for their dedicated assistance in the field; Andrea Polidori, Michael Koch, Philip M. Fine in the South Coast Air Quality Management District; Frank Hammes in the IQAir for their collaboration efforts.

Finally, I acknowledge the funding agencies: the California Air Resources Board (contract #11-310) and the National Science Foundation (contract #32525-A6010) for the financial support throughout my doctoral research.

The Appendices provide reprints of my publications. I deeply appreciate the Elsevier Publishing for granting reprint permission on the following articles:

Quiros, D.C., **Lee, E.S.**, Wang, R., Zhu, Y.F., 2013. Ultrafine particle exposure of street users walking, cycling, and driving along an urban residential roadway. Atmospheric Environment. 73, 185-194.

Lee, E.S., Polidori, A., Koch, M., Fine, P.M., Mehadi, A., Hammond, D., Wright, J.N., Miguel, A.H., Ayala, A., Zhu, Y.F., 2013. Water-based condensation particle counter comparisons in a near freeway with significant heavy duty diesel traffic. Atmospheric Environment. 68, 151-161.

Lee, E.S., Xu, B., Zhu, Y.F., 2012. Measurement of electric charge distributions on ultrafine particles in on- and near-roadway atmospheres. Atmospheric Environment. 60, 564-572.

VITA

1998 – 2003	B.E. Civil Engineering
	Kyoungpook National University, Daegu, Republic of Korea
2005 – 2007	M.S.E. Environmental Engineering
	University of Texas at Austin
2007 – 2008	Modeling & Assessment Engineer
	Texas Commission on Environmental Quality
2010 – 2011	Teaching Assistant
	University of California, Los Angeles
2011 – 2013	Graduate Student Researcher
	University of California, Los Angeles

PUBLICATIONS

Lee, E.S., Stenstrom, M.K., Zhu, Y.F., 2013. Ultrafine particle infiltration into passenger vehicles: the effects of driving speed and ventilation condition. Environmental Science and Technology (in review)

Lee, E.S., Zhu, Y.F., 2013. Application of a high-efficiency cabin air filter for simultaneous control of ultrafine particles and carbon dioxide in passenger vehicles. Environmental Science and Technology (in review)

Lee, E.S., Stenstrom, M.K., Zhu, Y.F., 2013. Development of a dynamic in-cabin ultrafine particle model incorporating infiltration and passive ventilation. Indoor Air (in review)

Quiros, D.C., **Lee, E.S.**, Wang, R., Zhu, Y.F., 2013. Ultrafine particle exposure of street users walking, cycling, and driving along an urban residential roadway. Atmospheric

Environment. 73, 185-194.

Lee, E.S., Polidori, A., Koch, M., Fine, P.M., Mehadi, A., Hammond, D., Wright, J.N., Miguel, A.H., Ayala, A., Zhu, Y.F., 2013. Water-based condensation particle counter comparisons in a near freeway with significant heavy duty diesel traffic. Atmospheric Environment. 68, 151-161.

Lee, E.S., Xu, B., Zhu, Y.F., 2012. Measurement of electric charge distributions on ultrafine particles in on- and near-roadway atmospheres. Atmospheric Environment. 60, 564-572.

PRESENTATIONS

Lee, E.S., Fung, D.C., and Zhu, Y.F., "Application of high efficiency cabin air filter for simultaneous control of ultrafine particles and carbon dioxide in passenger vehicles", AAAR annual conference, Portland, OR, Oct 2013 (Accepted)

Lee, E.S., Stenstrom, M.K., and Zhu, Y.F., "Dynamic modeling study for in-cabin ultrafine particle transport: evaluation of infiltration and passive ventilation in a wide range of driving speed", AAAR annual conference, Portland, OR, Oct 2013 (Accepted)

Lee, E.S., Polidori, A., Koch, M., Fine, P.M., Mehadi, A., Hammond, D., Wright, J.N., Miguel, A.H., Ayala, A., and Zhu, Y.F., "Inter- and intra-model comparisons of water-based condensation particle counters near a major freeway with significant heavy-duty diesel traffic", AAAR annual conference, Minneapolis, MN, Oct 2012

Lee, E.S., Xu, B., and Zhu, Y.F., "Quantification of ultrafine particles with electric charges in on- and near-freeway environments", AAAR annual conference, Minneapolis, MN, Oct 2012

Lee, E.S. and Zhu, Y.F., "Ultrafine particle infiltration to passenger vehicle cabins: the effects of driving speed and ventilation setting", AAAR annual conference, Minneapolis, MN, Oct 2012

Quiros, D.C., **Lee, E.S.**, Zhu, Y.F., and Wang, R., "Ultrafine particle exposure of street users walking, cycling, and driving along an urban residential roadway", AAAR annual conference, Minneapolis, MN, Oct 2012

Lee, E.S., Stenstrom, M.K., and Zhu, Y.F., "Automotive envelope leakage and infiltration of ultrafine particles: the effects of ventilation settings and driving conditions", UKC, Los Angeles, CA, Aug 2012

1. INTRODUCTION

1.1. Passenger Exposures to Ultrafine Particles

Ultrafine particles (UFPs, diameter ≤ 100 nm) constitute a significant health concern due to their adverse health effects. Elevated ambient UFP concentrations are well known to cause pulmonary[1-3] and cardiovascular diseases.[4,5] Recently, an increasing number of findings have also reported that the adverse health effects of UFPs are not limited to the pulmonary and cardiovascular problems because UFPs can also damage other organs through inter-organ translocation.[6-13] The cardiovascular system is considered a target to which UFPs can translocate from the lungs, as demonstrated in animal models[6-8,11,12] and human subjects.[9,10] Once inhaled, UFPs can penetrate the epithelium, enter the circulatory system, and deposit into other organs, including the brain.[13] The small size and large surface area of UFPs enable them to penetrate cell walls and localize in mitochondria.[14] Due to the numerous redox-active chemicals present in motor-vehicle-emitted UFPs, systemic inflammation can also occur.[15,16]

UFPs originate primarily from traffic emissions in urban environments.[17] Accordingly, UFP concentrations have been most significantly observed on the roadway where UFP concentration is usually an order of magnitude higher on the roadway than in the urban

background.[18] The on-road UFP concentration typically ranges from 100,000 to 500,000 particles/cm^3 [19-21] because motor-vehicle emissions usually constitute the most significant source of primary UFPs in urban areas.[22,23] In results, the on-road concentration is much higher than the ambient background typically on the order of 5,000-50,000 particles/cm^3.

Modern vehicle models are mostly equipped with a cabin air filter[24]; however, its filtration is not effective for UFPs. Under outdoor air (OA) mode, automotive ventilation system supplies ambient air into the passenger cabin and strains airborne particles. However, even after the cabin air filtration, the UFP concentration still remains an order of magnitude higher in the passenger cabin than in the urban background.[18] It is also important to note that the in-cabin UFP concentration can further increase in a confined environment such as a tunnel.[25] Accordingly, studies have showed that the commuting exposure alone may account for up to 45-50 % of the total daily exposure to UFPs in spite of the short commuting time (1.3 h/day).[20,26]

1.2. Background and Motivation

High level of passenger exposure occurs largely due to the followings: high air exchange rates (AERs),[27,28] vehicle envelope leakage,[29,30] and low filter efficiency.[24,31] AER is defined as the number of air turn-over per time and often has a unit of 1/h. In automotive passenger cabin, air exchange occurs primarily through the ventilation system under OA mode but also through the vehicle envelope leakage (i.e., infiltration). Under recirculation (RC) mode, the infiltration becomes the primary air path whereby on-road pollutants can also penetrate. Therefore, the selection of ventilation setting determines the in-cabin air quality.

Previous studies on automotive cabin air quality have focused on AERs. Most of these studies adopted the tracer gas decay method and found that the in-cabin AER differs by vehicle models, ventilation modes (i.e., the OA and RC modes), fan settings, and driving speeds.[27,32,33] The RC mode AER is also known as a function of the manufacturer origin, vehicle age, mileage, and driving speed.[34] Saber et al.[28] well summarized the reported in-cabin AERs in previous studies.

Although AER is an important measure, it is limited to explain the UFP infiltration to the passenger cabin. First, AER is not specific to leakage locations whereas the infiltration is. Considering the aerodynamic effects on a moving vehicle envelope and the associated changes in

pressure fields, the infiltration can highly depend on the leakage location and envelope surface pressure changes on the vehicle envelope. Second, AER acquired from the widely-used tracer gas tests does not describe particle loss during infiltration processes. Although limited to lab-scale idealized automotive leakage, Xu et al.[35] demonstrated that the particle loss also changes with respect to the particle size, leakage geometry, and pressure difference. Therefore, the difficulties quantifying the UFP infiltration and automotive envelope leakage had been a major challenge to better understand the in-cabin air quality.

The knowledge gaps in the automotive leakage and infiltration have also limited previous modeling studies. A few modeling studies have proposed a dimensionless in-cabin UFP model but often neglected infiltration terms[36] or required challenging measurements for the infiltration air-flow rate.[37] Because infiltration typically occurs through unknowingly distributed leakage in the vehicle envelope, direct instrumental measurements are not experimentally feasible for the infiltration air-flow rates. The aerodynamic surface pressure on the moving vehicle also increases substantially with driving speed[38] and, as anticipated, changes the infiltration air-flow rate. To incorporate infiltration as a function of driving speed, an idealized leakage model[39] has previously been utilized.[35,40] However, application of this model is also limited because the required model inputs include difficult measurements of leakage geometry dimensions and infiltration air-flow rates as a function of driving speed.

It is possible to prevent the infiltration by maintaining an appropriate level of cabin pressurization; however, the manufacturer-installed cabin air filters demonstrated very low UFP filtration efficiency only at 40-60%.[31] In this case, the passengers are still exposed to the unfiltered portion of UFPs even if the infiltration is successfully prevented by high in-cabin pressurization in OA mode. Although the RC mode of the automotive ventilation system can achieve the maximum protection (~85%) using the manufacturer-installed cabin air filters,[20,36] this setting causes passenger-exhaled CO_2 to accumulate rapidly in the vehicle cabin. Therefore, the current automotive ventilation systems and cabin air filters cannot control both UFPs and CO_2 simultaneously while preventing the infiltration of on-road UFPs.

1.3. Objectives

The fundamental goal of this dissertation is to reduce passenger exposures to on-road pollutants. To achieve this goal, this study included the three major objectives. The first objective is to quantify UFP infiltration by evaluating the effects of driving speed and ventilation conditions. The second objective is to develop an in-cabin air quality model incorporating the infiltration and passive ventilation in order to examine dynamic changes of in-cabin air quality in a wide range of driving speed using the developed model. Finally, the last objective is to develop a simultaneous control strategy to reduce passenger exposures to UFPs and CO_2.

1.4. Organization of the Dissertation

This dissertation contains five chapters. Chapter 1 summarizes the problems and motivations of this dissertation work leading to develop the three major objectives. In Chapter 2, this work experimentally evaluated in UFP infiltration in both stationary and mobile conditions and discusses dynamic behavior of UFP infiltration in terms of the ventilation modes, fan settings, driving speed, and vehicle types. In Chapter 3, from the experimental observations on UFP infiltration, this work quantitatively formulated an infiltration model and coupled it with a dimensionless pseudo-steady-state in-cabin UFP model. Then, using the developed model, the

work in this Chapter investigated the effects of driving speed and passive ventilation on UFP infiltration and evaluated the parametric significance of different particle gain/loss mechanisms, including active and passive OA ventilation, RC filtration, infiltration, and surface deposition. Chapter 4 investigated a novel / low-cost in-cabin air quality control method, which allows for simultaneous control of both UFPs and CO_2 using high-efficiency particulate air (HEPA) filtration in outdoor air (OA) mode. From the field measurements in a wide range of vehicle models of different vehicle types from several automobile manufacturers, this dissertation work compared different levels of in-cabin exposure reductions under three driving conditions (i.e., stationary, local roadway, and freeway) with four different filter types: no filter, in-use original equipment manufacturer (OEM), and two types of HEPA filters. Finally, Chapter 5 provides the overall summary and conclusion of this dissertation work.

References

(1) Penttinen, P.; Timonen, K. L.; Tiittanen, P.; Mirme, A.; Ruuskanen, J.; Pekkanen, J. Ultrafine particles in urban air and respiratory health among adult asthmatics. *European Respiratory Journal* **2001**, *17*, 428-435.

(2) Peters, A.; Wichmann, H. E.; Tuch, T.; Heinrich, J.; Heyder, J. Respiratory effects are associated with the number of ultrafine particles. *American Journal of Respiratory and Critical Care Medicine* **1997**, *155*, 1376-1383.

(3) von Klot, S.; Wolke, G.; Tuch, T.; Heinrich, J.; Dockery, D. W.; Schwartz, J.; Kreyling, W. G.; Wichmann, H. E.; Peters, A. Increased asthma medication use in association with ambient fine and ultrafine particles. *European Respiratory Journal* **2002**, *20*, 691-702.

(4) Andersen, Z. J.; Olsen, T. S.; Andersen, K. K.; Loft, S.; Ketzel, M.; Raaschou-Nielsen, O. Association between short-term exposure to ultrafine particles and hospital admissions for stroke in copenhagen, denmark. *European Heart Journal* **2010**, *31*, 2034-2040.

(5) Stolzel, M.; Breitner, S.; Cyrys, J.; Pitz, M.; Wolke, G.; Kreyling, W.; Heinrich, J.; Wichmann, H. E.; Peters, A. Daily mortality and particulate matter in different size classes in erfurt, germany. *Journal of Exposure Science and Environmental Epidemiology* **2007**, *17*, 458-467.

(6) Gilmour, P. S.; Ziesenis, A.; Morrison, E. R.; Vickers, M. A.; Drost, E. M.; Ford, I.; Karg, E.; Mossa, C.; Schroeppel, A.; Ferron, G. A.; Heyder, J.; Greaves, M.; MacNee, W.; Donaldson, K. Pulmonary and systemic effects of short-term inhalation exposure to ultrafine carbon black particles. *Toxicology and Applied Pharmacology* **2004**, *195*, 35-44.

(7) Hamoir, J.; Nemmar, A.; Halloy, D.; Wirth, D.; Vincke, G.; Vanderplasschen, A.; Nemery, B.; Gustin, P. Effect of polystyrene particles on lung microvascular permeability in isolated perfused rabbit lungs: Role of size and surface properties. *Toxicology and Applied Pharmacology* **2003**, *190*, 278-285.

(8) Kreyling, W. G.; Semmler, M.; Erbe, F.; Mayer, P.; Takenaka, S.; Schulz, H.; Oberdorster, G.; Ziesenis, A. Translocation of ultrafine insoluble iridium particles from lung epithelium to extrapulmonary organs is size dependent but very low. *Journal of Toxicology and Environmental Health-Part A* **2002**, *65*, 1513-1530.

(9) Nemmar, A.; Hoet, P. H. M.; Vanquickenborne, B.; Dinsdale, D.; Thomeer, M.; Hoylaerts, M. F.; Vanbilloen, H.; Mortelmans, L.; Nemery, B. Passage of inhaled particles into the blood circulation in humans. *Circulation* **2002**, *105*, 411-414.

(10) Nemmar, A.; Hoylaerts, M. F.; Hoet, P. H. M.; Nemery, B. Possible mechanisms of the cardiovascular effects of inhaled particles: Systemic translocation and prothrombotic

effects. *Toxicology Letters* **2004**, *149*, 243-253.

(11) Nemmar, A.; Vanbilloen, H.; Hoylaerts, M. F.; Hoet, P. H. M.; Verbruggen, A.; Nemery, B. Passage of intratracheally instilled ultrafine particles from the lung into the systemic circulation in hamster. *American Journal of Respiratory and Critical Care Medicine* **2001**, *164*, 1665-1668.

(12) Oberdorster, G. Pulmonary effects of inhaled ultrafine particles. *International Archives of Occupational and Environmental Health* **2001**, *74*, 1-8.

(13) Oberdorster, G.; Sharp, Z.; Atudorei, V.; Elder, A.; Gelein, R.; Kreyling, W.; Cox, C. Translocation of inhaled ultrafine particles to the brain. *Inhalation Toxicology* **2004**, *16*, 437-445.

(14) Li, N.; Sioutas, C.; Cho, A.; Schmitz, D.; Misra, C.; Sempf, J.; Wang, M. Y.; Oberley, T.; Froines, J.; Nel, A. Ultrafine particulate pollutants induce oxidative stress and mitochondrial damage. *Environmental Health Perspectives* **2003**, *111*, 455-460.

(15) Sioutas, C.; Delfino, R. J.; Singh, M. Exposure assessment for atmospheric ultrafine particles (ufps) and implications in epidemiologic research. *Environmental Health Perspectives* **2005**, *113*, 947-955.

(16) Elder, A.; Couderc, J.-P.; Gelein, R.; Eberly, S.; Cox, C.; Xia, X.; Zareba, W.; Hopke, P.; Watts, W.; Kittelson, D.; Frampton, M.; Utell, M.; Oberdorster, G. Effects of on-road highway aerosol exposures on autonomic responses in aged, spontaneously hypertensive rats. *Inhalation Toxicology* **2007**, *19*, 1-12.

(17) Shi, Z. B.; Shao, L. Y.; Jones, T. P.; Whittaker, A. G.; Lu, S. L.; Berube, K. A.; He, T.; Richards, R. J. Characterization of airborne individual particles collected in an urban area, a satellite city and a clean air area in beijing, 2001. *Atmospheric Environment* **2003**, *37*, 4097-4108.

(18) Morawska, L.; Ristovski, Z.; Jayaratne, E. R.; Keogh, D. U.; Ling, X. Ambient nano and ultrafine particles from motor vehicle emissions: Characteristics, ambient processing and implications on human exposure. *Atmospheric Environment* **2008**, *42*, 8113-8138.

(19) Westerdahl, D.; Fruin, S.; Sax, T.; Fine, P. M.; Sioutas, C. Mobile platform measurements of ultrafine particles and associated pollutant concentrations on freeways and residential streets in los angeles. *Atmospheric Environment* **2005**, *39*, 3597-3610.

(20) Zhu, Y. F.; Eiguren-Fernandez, A.; Hinds, W. C.; Miguel, A. H. In-cabin commuter exposure to ultrafine particles on los angeles freeways. *Environmental Science & Technology* **2007**, *41*, 2138-2145.

(21) Zhu, Y.; Fung, D. C.; Kennedy, N.; Hinds, W. C.; Eiguren-Fernandez, A. Measurements of ultrafine particles and other vehicular pollutants inside a mobile exposure system on los angeles freeways. *Journal of the Air & Waste Management Association* **2008**, *58*, 424-

434.

(22) Hitchins, J.; Morawska, L.; Wolff, R.; Gilbert, D. Concentrations of submicrometre particles from vehicle emissions near a major road. *Atmospheric Environment* **2000**, *34*, 51-59.

(23) Shi, J. P.; Khan, A. A.; Harrison, R. M. Measurements of ultrafine particle concentration and size distribution in the urban atmosphere. *Science of the Total Environment* **1999**, *235*, 51-64.

(24) Qi, C.; Stanley, N.; Pui, D. Y. H.; Kuehn, T. H. Laboratory and on-road evaluations of cabin air filters using number and surface area concentration monitors. *Environmental Science & Technology* **2008**, *42*, 4128-4132.

(25) Knibbs, L. D.; de Dear, R. J.; Morawska, L.; Mengersen, K. L. On-road ultrafine particle concentration in the m5 east road tunnel, sydney, australia. *Atmospheric Environment* **2009**, *43*, 3510-3519.

(26) Fruin, S.; Westerdahl, D.; Sax, T.; Sioutas, C.; Fine, P. M. Measurements and predictors of on-road ultrafine particle concentrations and associated pollutants in los angeles. *Atmospheric Environment* **2008**, *42*, 207-219.

(27) Knibbs, L. D.; de Dear, R. J.; Atkinson, S. E. Field study of air change and flow rate in six automobiles. *Indoor Air* **2009**, *19*, 303-313.

(28) Saber, E. M.; Bazargan, M. Dynamic behavior modeling of cigarette smoke particles inside the car cabin with different ventilation scenarios. *International Journal of Environmental Science and Technology* **2011**, *8*, 747-764.

(29) Chan, L. Y.; Lau, W. L.; Zou, S. C.; Cao, Z. X.; Lai, S. C. Exposure level of carbon monoxide and respirable suspended particulate in public transportation modes while commuting in urban, area of guangzhou, china. *Atmospheric Environment* **2002**, *36*, 5831-5840.

(30) Esber, L. A.; El-Fadel, M.; Nuwayhid, I.; Saliba, N. The effect of different ventilation modes on in-vehicle carbon monoxide exposure. *Atmospheric Environment* **2007**, *41*, 3644-3657.

(31) Xu, B.; Liu, S. S.; Liu, J. J.; Zhu, Y. F. Effects of vehicle cabin filter efficiency on ultrafine particle concentration ratios measured in-cabin and on-roadway. *Aerosol Science and Technology* **2011**, *45*, 234-243.

(32) Ott, W.; Klepeis, N.; Switzer, P. Air change rates of motor vehicles and in-vehicle pollutant concentrations from secondhand smoke. *Journal of Exposure Science and Environmental Epidemiology* **2008**, *18*, 312-325.

(33) Hudda, N.; Eckel, S. R.; Knibbs, L. D.; Sioutas, C.; Delfino, R. J.; Fruin, S. A. Linking in-vehicle ultrafine particle exposures to on-road concentrations. *Atmospheric*

Environment **2012**, *59*, 578-586.

(34) Fruin, S. A.; Hudda, N.; Sioutas, C.; Defino, R. J. Predictive model for vehicle air exchange rates based on a large, representative sample. *Environmental Science & Technology* **2011**, *45*, 3569-3575.

(35) Xu, B.; Liu, S.; Zhu, Y. Ultrafine particle penetration through idealized vehicle cracks. *Journal of Aerosol Science* **2010**, *41*, 859-868.

(36) Pui, D. Y. H.; Qi, C.; Stanley, N.; Oberdorster, G.; Maynard, A. Recirculating air filtration significantly reduces exposure to airborne nanoparticles. *Environmental Health Perspectives* **2008**, *116*, 863-866.

(37) Hudda, N.; Kostenidou, E.; Sioutas, C.; Delfino, R. J.; Fruin, S. A. Vehicle and driving characteristics that influence in-cabin particle number concentrations. *Environmental Science & Technology* **2011**, *45*, 8691-8697.

(38) Lee, E. S.; Stenstrom, M. K.; Zhu, Y. F. Ultrafine particle infiltration into passenger vehicles: Effects of driving speed and ventilation condition. *Environmental Science & Technology* **2013**, *xx*, xxx-xxx.

(39) Baker, P. H.; Sharples, S.; Ward, I. C. Air-flow through cracks. *Building and Environment* **1987**, *22*, 293-304.

(40) Xu, B.; Zhu, Y. Quantitative analysis of the parameters affecting in-cabin to on-roadway (i/o) ultrafine particle concentration ratios. *Aerosol Science and Technology* **2009**, *43*, 400-410.

2. IN-CABIN ULTRAFINE PARTICLE INFILTRATION

2.1. Abstract

Previous studies have reported ultrafine particle (UFP) infiltration to the in-cabin microenvironment; however, no systematic measurements have been conducted showing where and under what conditions the infiltration occurs. Guided by the principle of the leakage function from building environments, this study examined the leakage and UFP infiltration in 11 passenger vehicle models. We found the outdoor air (OA) mode air exchange rate (AER) is linearly proportional to the equivalent leakage area (ELA). UFP infiltration highly depends on the ventilation conditions and the aerodynamic differential pressure changes on a moving vehicle envelope. The leakage around the side doors usually has no UFP infiltration because of cabin pressurization under OA mode. Under RC mode, aerodynamic effects on the moving vehicle surface make the surface pressure on the side doors relatively lower than the cabin pressure. UFP infiltration mainly occurs through rear trunk gaps because moving vehicles create positive pressure on the surface of the rear trunk gaps while the in-cabin pressure is neutral. As driving speed increases, the pressure difference becomes highly negative (i.e., no infiltration) on the side doors but highly positive (i.e., more infiltration) on the rear trunk. These data provide the first

experimental evidence that UFP infiltration is a function of ventilation conditions and aerodynamic changes around the vehicle envelope.

2.2. Introduction

Ultrafine particle (UFP) concentration is usually an order of magnitude higher on the roadway than in the urban background.[1] The in-cabin UFP concentration substantially increases in a confined environment such as a tunnel.[2] Depending on the proximity to vehicle emissions on the roadway, passengers often experience high UFP concentrations in the automotive cabin because of high air exchange rates[3], the leakage of the vehicle envelope[4,5], and the low cabin air filter efficiency.[6] Studies have showed that the commuting exposure alone may account for up to 45 - 50 % of the total daily exposure to UFPs.[7,8]

Previous studies on automotive cabin air quality have focused on the air exchange rate (AER). Most of these studies adopted the tracer gas decay method and found that the in-cabin AER differs by vehicle models, ventilation modes (i.e., the outdoor air (OA) and recirculation (RC) modes), fan settings, and driving speeds.[9-11] The RC mode AER is also known as a function of the manufacturer origin, vehicle age, mileage, and driving speed.[12] Saber et al.[13] summarized the reported in-cabin AERs in previous studies.

Although AER is an important parameter that accounts for all routes of air exchange, AER by itself is not appropriate to explain the UFP infiltration to the passenger cabin. First, AER is not specific to leakage locations while the infiltration is. Considering the aerodynamic effects on a moving vehicle envelope and the associated changes in pressure fields, infiltration can highly depend on the leakage location and envelope surface pressure changes on the vehicle envelope. Second, AER from the tracer gas tests does not describe particle loss during infiltration processes. Although limited to lab-scale idealized automotive leakage, Xu et al.[14] found that the particle loss also changes with respect to the particle size, leakage geometry, and pressure difference.

This study adopted the principle of the leakage function from building environments to address UFP infiltration into the vehicle cabin. From the measurements of supplied air-flow rate (Q_{vent}) and the associated changes in differential pressure (dP), the leakage function (see Eq. (2.2)) describes the envelope leakage in a power-law correlation with two parameters: the flow coefficient (C_f) and the pressure exponent (n).[15,16] Leakage characterization using this method is also advantageous to determine an equivalent leakage area (ELA) for complex leakage openings (i.e., geometry). Automotive envelope leakage has also been explained with the same principle.[17]

When a vehicle has a high driving speed, the aerodynamic pressure field will change on the vehicle envelope, which further impacts the leakage on the vehicle envelope. For instance,

one common observation in automotive aerodynamic studies is that the driving-induced aerodynamic changes generate a low pressure field on the side surface but a high pressure field on the rear surface of the moving vehicle.[18] The magnitude of the surface pressure could also change drastically as the driving speed increases, and it is specific to the location on the automotive envelope. In addition, the leakage flow rate could also change substantially due to cabin pressurization under mechanical ventilation conditions (i.e., ventilation mode and fan setting). Therefore, it is important to take into account the ventilation modes, fan settings, driving speed, and vehicle shape when studying automotive envelope leakage to understand UFP infiltration to the passenger cabin.

In this study, 11 different vehicles were tested to investigate UFP infiltration in both stationary and mobile conditions. The variability of the blower fan and the level of cabin pressurization were first examined. In stationary mode, we determined the automotive leakage functions and compared OA-mode AERs to ELA. The aerodynamic differential pressure changes were then investigated at four representative leakage locations on moving vehicles. The dynamic behavior of UFP infiltration in terms of the ventilation modes, fan settings, driving speed, and vehicle types is also discussed.

2.3. Methods

2.3.1. Vehicle Selections and Quartile Fan Settings

The selected vehicles had age and mileage ranging from 1 to 12 years and 31,000 to 261,000 km, respectively. The test vehicle models include four passenger vehicle types, representing four different shapes: five sedans, two hatchbacks, two SUVs, and two minivans. The total cabin volume size of the test vehicles ranges from 2.77 to 7.03 m^3.[19] These vehicles have a wide variety of fan setting scales ranging from a minimum of 1 - 4 to a maximum of 1 - 12. To achieve comparable fan settings among tested vehicles, a quartile method was used. In both OA and RC modes, four evenly distributed fan settings (noted as Q1, Q2, Q3, and Q4) were used with Q1 and Q4 representing the minimum and the maximum, respectively. The test vehicle specifications are tabulated in Table 2.1. The specified numbers in Q4 is equal to the total number of fan settings found in the vehicle models. The numbers in parentheses indicate the ventilation air flow rates (m^3/hr) corresponding to each fan setting in OA mode. In addition, no mechanical ventilation condition (i.e. Qoff) was also tested.

Table 2.1 A summary of the test vehicle models and specifications

Manuf.	Model	Year	Mileage (km)	Vehicle Type	Cabin Volume[19] (m^3)			Quartile Fan Settings				Leakage Parameters	
					Total	Passenger	Cargo	Q1	Q2	Q3	Q4	Flow Coefficient (C_f)	Pressure Exponent (n)
Ford	Focus	2012	51,000	Sedan	2.94	2.57	0.37	1 (*110*)	3 (*160*)	5 (*288*)	7 (*335*)	18.78	0.82
Toyota	Corolla*	2005	184,000	Sedan	2.94	2.56	0.39	1 (*58*)	2 (*83*)	3 (*121*)	4 (*176*)	23.39	0.62
	Matrix*	2005	141,000	Hatchback	2.85	2.52	0.33	1 (*73*)	2 (*103*)	3 (*150*)	4 (*221*)	19.71	0.73
	Scion tC*	2008	67,000	Hatchback	2.77	2.40	0.37	1 (*84*)	3 (*138*)	5 (*221*)	7 (*298*)	28.70	0.65
	Sienna	2011	68,000	Minivan	5.76	4.66	1.11	1 (*112*)	3 (*229*)	5 (*341*)	6 (*463*)	72.12	0.53
Honda	Civic	2001	261,000	Sedan	2.86	2.49	0.37	1 (*83*)	4 (*157*)	7 (*278*)	9 (*367*)	21.21	0.76
	Accord*	2001	198,000	Sedan	3.28	2.72	0.45	1 (*125*)	5 (*280*)	9 (*452*)	12 (*509*)	23.38	0.85
	Odyssey*	2010	35,000	Minivan	7.03	5.94	1.09	1 (*130*)	3 (*278*)	5 (*440*)	7 (*596*)	31.40	0.75
Mercedes	GL450	2007	58,000	SUV	4.49	4.04	0.45	1 (*80*)	2 (*102*)	4 (*186*)	5 (*315*)	30.71	0.61
BMW	X3	2007	76,000	SUV	3.40	2.55	0.85	1 (*109*)	3 (*169*)	5 (*269*)	8 (*479*)	30.33	0.87
VW	Cc	2010	31,000	Sedan	3.10	2.73	0.37	1 (*133*)	2 (*202*)	3 (*300*)	4 (*522*)	6.63	1.00

* indicates the five vehicle models used in the mobile measurements

2.3.2. Instrumentation

The primary parameters affecting automotive envelope leakage include the ventilation air flow rate and the differential pressure. The ventilation air flow rate was measured with a ventilation meter (Q-trak model 7565-X with model 960, TSI Inc., St. Paul, MN) securely attached on the in-cabin air inlet diffuser. Two manometers (Model HD755, Extech Instruments Co., Nashua, NH) were used to measure the differential pressures between the cabin and the side door and between the cabin and the rear trunk gaps with an accuracy of ± 1 Pa. The

measurements were carried out concurrently at the pressure sampling locations: 2 and 4 as well as 1 and 3 as shown in Figure 2.1.

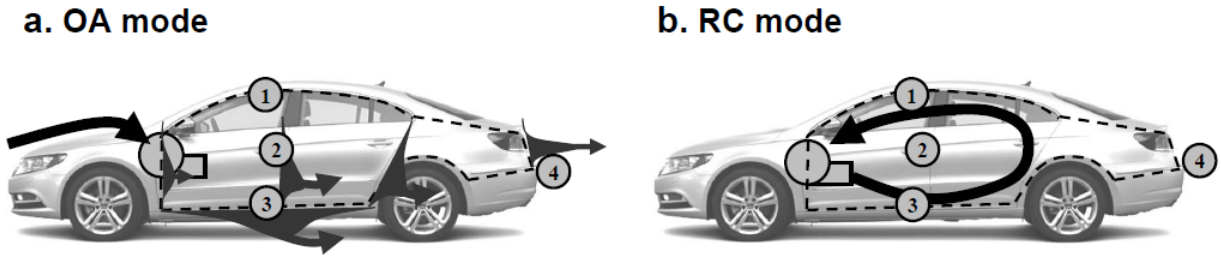


Figure 2.1 Graphical illustrations of the in-cabin air flow path
Ventilation air flow path (arrow) in the (a) outdoor air (OA) mode and (b) recirculation (RC) mode. OA mode ventilation is an open-loop system starting from the outdoor air intake and ending at the exhaust through the side-doors and rear-trunk leakage. RC mode is a close-loop system that utilizes the same cabin air. The total cabin volume is illustrated in dotted lines. The circled numbers symbolize the four manometer sensor locations. The differential pressure measurements were named after the number symbols as followed: dP_1, dP_2, dP_3, and dP_4.

Three sets of condensation particle counters (CPCs) measured UFP number concentrations concurrently at three locations: in the center of vehicle cabin ($C_{in\text{-}cabin}$), outside for ambient/on-roadway measurements ($C_{on\text{-}road}$), and inside near the rear trunk gap (C_{trunk}). A CPC (Model 3785, TSI Inc., St. Paul, MN) monitored $C_{in\text{-}cabin}$, while another CPC (Model 3786, TSI Inc., St. Paul, MN) monitoring $C_{on\text{-}road}$. The third CPC (Model 3007, TSI Inc., St. Paul, MN) detected the UFP infiltration through the rear trunk leakage (i.e., C_{trunk}). The CPC instruments

were collocated before and after field sampling for data quality assurance. Good correlations were observed among the three units. For the mobile experiments, the driving speed and the coordinates were logged by a GPS unit (Model BT-Q1000XT, QStarz Co. Ltd., Taiwan).

2.3.3. Stationary Measurements

The existing heating/air conditioning blower fan was utilized to pressurize the cabin as opposed to installing a blower-door on a window as used by Fletcher et al.[17]. The blower fan provided needed cabin pressurization under the OA mode. It is pertinent to note that this approach avoids considering the ventilation system as a potential leakage area. Although the penetration of air pollutants could occur through the ventilation systems, it is usually intended and controlled by choosing the ventilation settings. Thus, it is not considered as leakage or infiltration in this study; instead, it was regarded as passive ventilation.[9] In the pressurized cabin, the vehicle envelope leakage was identified at the gaps on the side doors and rear trunk using stannic chloride ($SnCl_4$) smoke tubes (model 9500, Nextteq LLC., Tampa, FL) in the pressurized cabin.

Under stationary condition, the mechanical ventilation flow was only allowed through a single open diffuser by closing and sealing the other inlet diffusers. In different fan settings, the

inlet air flow rates were estimated from the measurements of the diffuser area and air-flow velocity at the center of the diffuser. At the same time, the associated pressure differences between the in-cabin and the ambient were measured. The cabin pressure was uniform at various locations in the passenger cabin and the ambient pressure does not change considerably during the measurement period. The pressure differences across different vehicle models were due to different blower fan-capacity for individual vehicle. The measurements were repeated for all test vehicles under 10 possible combinations of the ventilation modes (i.e., OA and RC) and the quartile fan settings (i.e., Qoff, Q1, Q2, Q3, and Q4). All windows were closed during the measurements.

2.3.4. Mobile Measurements

To elucidate the aerodynamic effects, the ventilation air flow rates were monitored by the ventilation meter while the GPS tracking experimental conditions including the driving speed (e.g., driving speed, direction, coordinate, and elevation). The differential pressure measurements were conducted on both freeways and local roadways. The differential pressure changes on the vehicle envelope were monitored at four locations: three around the side door and one in the lateral center of the rear trunk gap (see Figure 2.1 for more detail). Each manometer measured the differential pressure (dP_i) in this study, as followed:

$$dP_i = P_{in-cabin} - P_i \tag{2.1}$$

where dP_i is the differential pressure between the in-cabin and the sampling location i (Pa), $P_{in-cabin}$ is the pressure at the center of the passenger cabin (Pa), P_i is the pressure at the sampling location i (Pa), and i is the pressure sampling location on potential leakage area (i.e., door / trunk gaps) as indicated in Figure 2.1 (i.e., i = 1, 2, 3, and 4). Prior to the measurements, the potential leakage area was identified at the gaps of side-doors and rear-trunk using stannic chloride ($SnCl_4$) smoke tubes (model 9500, Nextteq LLC., Tampa, FL).

A positive differential pressure ($dP_i > 0$) indicates cabin pressurization (i.e., $P_{in-cabin} > P_i$) thereby ex-filtration, whereas a negative value ($dP_i < 0$) represents infiltration due to $P_i > P_{in-cabin}$.

The dP_i was found near zero for any given i in the stationary RC condition (see Figure 2.2d for more detail). Thus, when a vehicle driven in RC mode, the positive dP_i stems from an aerodynamic effects making P_i smaller than $P_{in\text{-}cabin}$. Under the same condition, negative differential pressure ($dP_i < 0$) may oppositely result from $P_i > P_{in\text{-}cabin}$. Although the aerodynamic studies identified a negative pressure field behind a moving object or leeward of a building,[15] it is important to note that the pressure distributions on object surfaces whereby infiltration occurs can be different.[18]

The on-road experiments were conducted under four extreme ventilation settings: OA-Qoff, OA-Q4, RC-Qoff, and RC-Q4. The measurements were repeated three times on the same route for each vehicle type and ventilation settings. All measurement data were collected with a 1-second sampling interval for all instruments to capture rapidly changing of UFP concentrations in-cabin and on-road.

2.3.5. Analytical

The concept of a power-law leakage function[15,16] in building environment studies was adopted to investigate automotive envelope leakage in this study (Eq. (2.2)).

$$Q_{vent} = C_f \cdot dP^n \tag{2.2}$$

where Q_{vent} is the ventilation air flow rate (m^3/hr), C_f is the flow coefficient (m^3/s Pa^n), dP is the differential pressure (Pa), and n is the pressure exponent. The power-law correlation between air-flow rate and pressure difference has its fundamental basis in the Bernoulli's equation. In case of an orifice flow, n is equal to 0.5 and C_f becomes a function of fluid density (ρ) and cross-sectional area (A) of the flow (i.e., $C_f = A(2/\rho)^{0.5}$). However, when this concept is applied to building envelope leakage, the value of n can vary from 0.55 to 0.75 because of complexity of leakage geometry and the value of 0.65 is typically assumed for building cracks.[15] Based on the measurements of Q_{vent} and dP at a wide range of fan settings, two-parameter power-law regression analyses provided semi-empirical estimates of a flow coefficient (C_f) and a pressure exponent (n) for each vehicle model (discussed more detail in Figure 2.3).

Given the values of C_f and n, the equivalent leakage area (ELA)[15,20] was estimated at a dP_{ref} of either 20 or 50 Pa. The 20 Pa was used because it was achieved in all 11 vehicle models regardless of blower fan capacities (discussed later in Variability in the mechanical ventilation

system in stationary condition). The 50 Pa was also used for comparison since it is the commonly used reference pressure in building environment studies.[15] It is important to note that the ELA is not equal to the actual leakage area because it changes slightly as a function of the reference pressure. However, the use of ELA is advantageous because it allows a reasonable comparison of the envelope leakage area among different vehicle models at the same reference pressure. Equation 3 describes the ELA calculation:

$$ELA = 3.6 \times 10^{7} \cdot \frac{C_f}{C_d} \cdot \left(\frac{\rho_{air}}{2} \right)^{1/2} \cdot dP_{ref}{}^{n-1/2} \tag{2.3}$$

where ELA is the equivalent leakage area (ELA) at a reference pressure (cm^2), C_f is the flow coefficient ($m^3/s\ Pa^n$) same as shown in Eq. (2.2), C_d is the discharge coefficient (= 1.0 $kg^{1/2}/m^{1/2}$ hr Pa)[15,20], ρ_{air} is the density of air (kg/m^3), and dP_{ref} is the reference differential pressure (Pa).

2.4. Results and Discussion

2.4.1. Variability in the Mechanical Ventilation Systems

Figure 2.2 presents the mechanical ventilation flow rates and the associated differential pressures for the 11 test vehicle models in stationary OA and RC conditions. The maximum mechanical ventilation flow rates (i.e., Q4) ranged from 200 to 600 m^3/hr (Figures 2.2a and c), indicating that the blower fan capacities vary substantially across different vehicle models. The ventilation mode (i.e., OA or RC) created distinctive differences in both ventilation air flow rate and differential pressure. In general, the mechanical ventilation flow rates were 13% higher on average (± 13% depending on vehicle models) under the RC mode (Figure 2.2c) than under the OA mode (Figure 2.2a). This is likely because the RC mode air flow cycle does not experience the same pressure drop at the OA intake manifold.

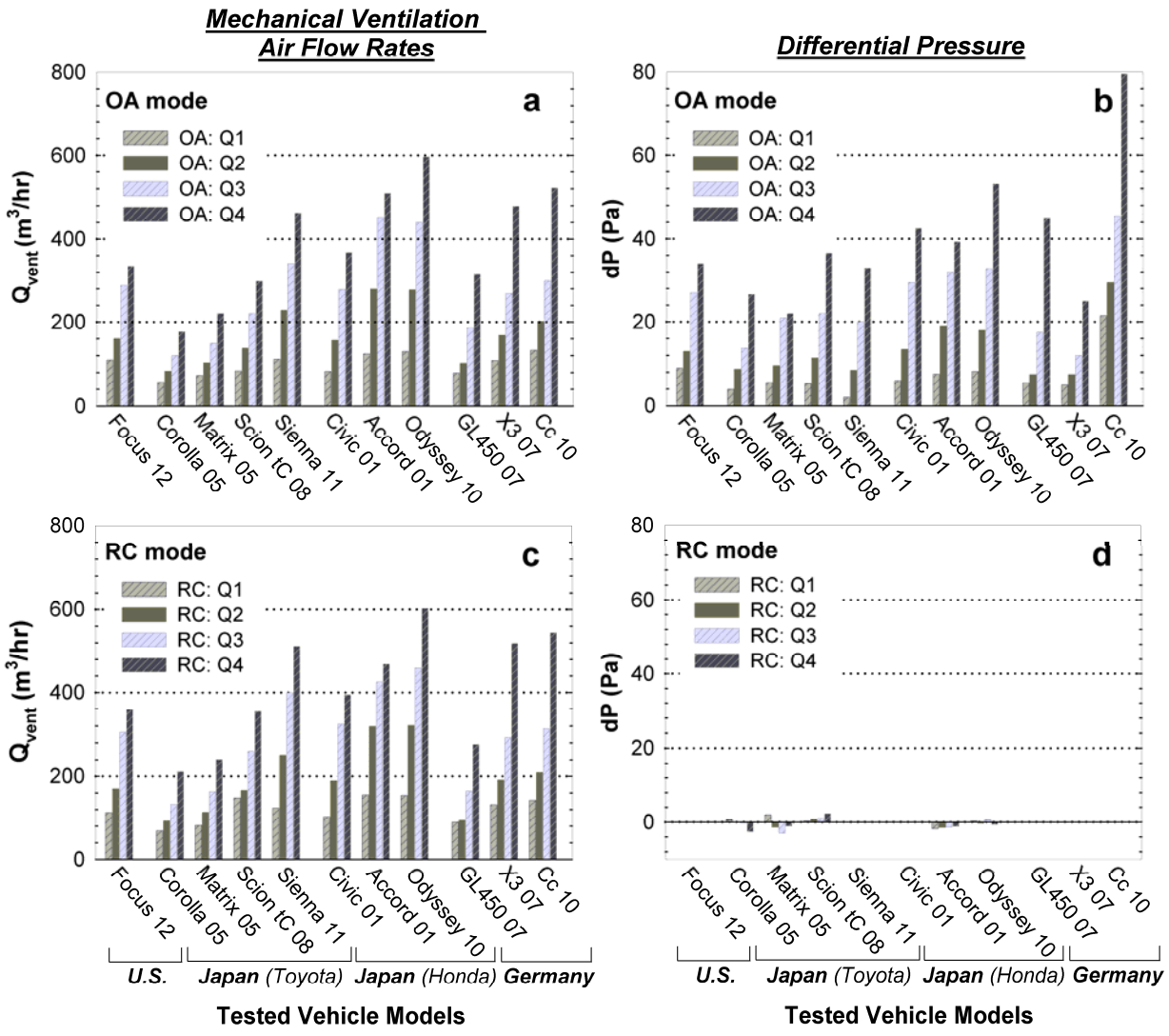


Figure 2.2 Variability of mechanical ventilation air-flow rates and the associated differential pressures across different vehicle models

Mechanical ventilation air-flow rates (Q_{vent}, panels a, c) and the associated differential pressures (dP, panels b, d) in the stationary condition are plotted for the OA (on the top) and RC (on the bottom) modes. The different shades indicate the different fan settings (i.e., Q1 through Q4). The x-axis shows the 11 test vehicle models ordered according to the manufacturers (i.e., Ford, Toyota, Honda, Mercedes-Benz, BMW, and Volkswagen) and the origin countries: U.S., Japan, and Germany.

Figure 2.2b shows the cabin pressurization under OA mode. The cabin pressurization reached up to 80 Pa during stationary mode measurements. Although it is clear that the differential pressure is a function of the ventilation inlet air flow rates, its variability across the different vehicle models was quite high under the same quartile fan settings. However, under the RC mode (i.e., closed air damper) of any fan setting, the differential pressure remained near zero (Figure 2.2d) within ± 3 Pa across the tested vehicle models. This indicates nearly 100% recirculation of the cabin air; otherwise, the RC mode would have resulted in a certain level of cabin pressurization despite the fan settings or the test vehicle models.

2.4.2. Leakage Function and Equivalent Leakage Area

Figure 2.3 presents the leakage functions characterized by the two parameters: the flow coefficient (C_f) and the pressure exponent (n). A regression of all 11 test vehicle models resulted C_f and n values of 38.14 and 0.62, respectively. Since the leakage geometry determines the leakage functions, different vehicle models presented a range of leakage function parameters from 6.63 to 72.12 for C_f and from 0.53 to 1.00 for n.

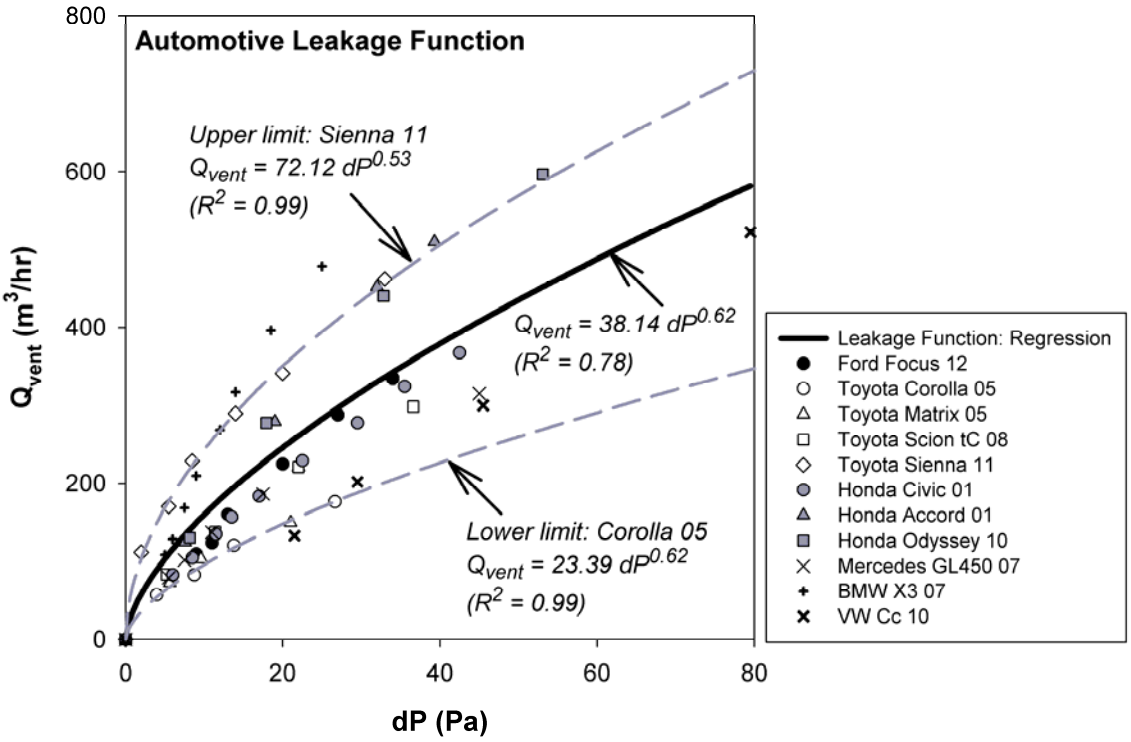


Figure 2.3 Automotive envelope leakage functions derived from the measurements of ventilation inlet air flow rate and corresponding differential pressure
The measurements of ventilation inlet air flow rate (Q_{vent}) and corresponding differential pressure (dP) are plotted. The different symbols represent the observations from the 11 test vehicle models, and the color schemes indicate the different origin countries and manufacturers: U.S. (black), Japan Toyota (white), and Japan Honda (gray). The German vehicle models are marked with line symbols (e.g., cross). Regression result of the measurements is given in solid line and the upper / lower limits are presented in dash lines.

From the power-law correlation, Equation 4 formulated the OA AER with differential pressure (dP) assuming well mixed in-cabin conditions under OA mode.[9,21] This is a reasonable assumption because of small cabin volume (V_{cabin}) size and high ventilation air flow rate (Q_{vent}). The OA AER calculation involves inlet air flow rate (i.e., Q_{vent} in Eq. (2.2)) which can be

estimated at any given dP with the vehicle-specific leakage function parameters (i.e., C_f and n). The OA AER can thus be calculated in the following form:

$$OA\,AER = \frac{Q_{vent}}{V_{cabin}} = \frac{C_f \cdot dP^n}{V_{cabin}} \tag{2.4}$$

where OA AER is the OA mode air exchange rate (hr^{-1}) and V_{cabin} is the cabin volume (m^3). It should be noted that the dP in Eq. (2.4) is the differential pressure caused by the mechanically supplied air flow rate (Q_{vent}); thus, it is independent from the reference pressure difference (dP_{ref}) in the Eq. (2.3).

With the OA AER, this study compared the increase of the OA AER with respect to the envelope leakage area (i.e., ELA) for different vehicle types (i.e., hatchback, sedan, SUV, and minivan) of various vehicle models from different manufacturers. The ELA was estimated at the reference pressure differences of 20 and 50 Pa using Eq. (2.3). Different cabin pressurization (20 Pa or 50 Pa) provided different Q_{vent} and demonstrated the changes in OA AER with respect to ELA (Figure 2.4). It shows that the OA AER linearly increases when leakage area (i.e., ELA) becomes large. It is important to note that higher inlet air flow rate (Q_{vent}) is required to achieve the same level of cabin pressurization for a leakier vehicle. However, higher cabin pressure in Figure 2.4 does not always mean proportionally higher OA AER and that was taken into account in Q_{vent} by applying vehicle-specific C_f and n in Eq. (2.4).

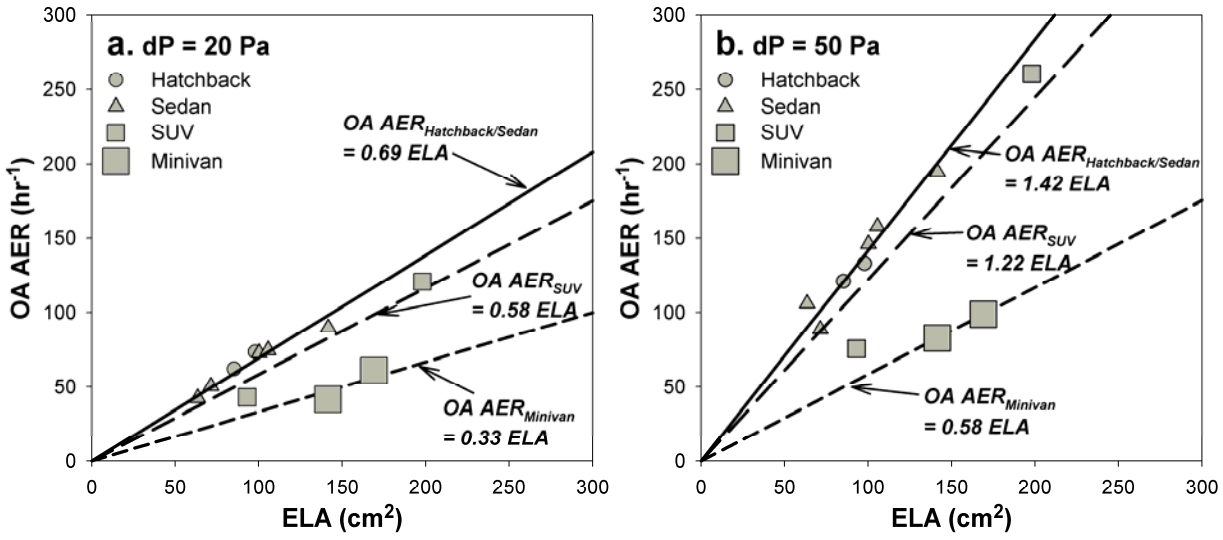


Figure 2.4 Linear correlations of outdoor air mode air exchange rates and equivalent leakage areas

For the different levels of cabin pressurization (dP) of (a) 20 Pa and (b) 50 Pa, the OA mode air exchange rates (OA AERs)are compared to the Equivalent Leakage Areas (ELAs) at 20 Pa. The linear relationship between the OA AER and the ELA is presented for hatchback/sedan (solid line), SUV (medium-dash line), and minivan (short-dash line).

Nonetheless, the rate of OA AER changes was specific to the vehicle type because SUV and minivan have V_{cabin} larger than hatchback and sedan. Assuming negligible temperature effects[17], the following relationship can be determined based on mass conservation (i.e., $Q_{in} = Q_{out}$):

$$OA\,AER = \frac{v_{leakage}}{V_{cabin}} \cdot ELA \tag{2.5}$$

where $v_{leakage}$ is the mean leakage air flow velocity (m/hr). Equation 5 quantitatively verifies the linear correlation observed in Figure 2.4. In Figure 2.4a, the slope of the linear regression (i.e., =

$v_{leakage}/V_{cabin}$) decreased from 0.69 to 0.33 because the V_{cabin} is larger for minivan than hatchback or sedan and the regression line for SUV lies in between the two ($v_{leakage}/V_{cabin}$ = 0.58). The increased cabin pressure in Figure 2.4b resulted higher $v_{leakage}/V_{cabin}$ for all vehicle types. A greater cabin pressurization, 50 Pa, for the same vehicle type consequently resulted in overall higher OA AER because of the increased $v_{leakage}$ while maintaining the same linear correlation as shown in Figure 2.4a. Therefore, the OA AER is linearly proportional to the ELA and is affected by vehicle types, more specifically V_{cabin}, rather than the manufacturers or vehicle models.

Recently, Hudda et al.[11] found a negatively proportional relationship between OA AER and cabin volume size (V_{cabin}); however, in this study we found the relationship was more complicated. As reported by Hudda et al.[11], over a wide range of observed OA AER values, its magnitude was generally lower for the large-cabin (V_{cabin} above 4 m^3) than the small-cabin (V_{cabin} below 4 m^3) vehicle models. This occurs primarily because the blower fan capacity is not high enough to supply a sufficient level of air exchange for relatively large vehicles. However, we observed a positively proportional increase of OA AER as a function of V_{cabin} when V_{cabin} is either greater or less than 4 m^3. Both small- and large-cabin vehicle models presented proportionally increasing OA AER as a function of cabin volume size. The OA AER increase was also positively greater at higher fan settings than at lower fan settings. Therefore, for either small or large vehicles, OA AER has a positive correlation with the size of V_{cabin}.

2.4.3. Aerodynamic Differential Pressure Changes on Moving Vehicles

The pressure field on the surface of the vehicle envelope (P_i) changes considerably because of the aerodynamic changes at different driving speeds and vehicle shapes. Accordingly, the differential pressure (dP_i) between the cabin and the leakage on the vehicle envelope vary not only by the leakage location but also by the driving speed and vehicle shape. Figure 2.5 presents differential pressure data collected under RC mode at four different leakage locations in two different vehicle types as a function of driving speed. The data were collected in five vehicle models and Figure 2.5 exhibits time-series measurements for a sedan (2008 Toyota Scion tC, Figure 2.5a) and a minivan (2010 Honda Odyssey, Figure 2.5b). The measurement data show distinguishable differences at different sampling locations, as illustrated in Figure 2.1. Under RC mode, air dampers are closed to prevent cabin pressure from increase. Therefore, the data in Figure 2.5 are not affected by the cabin pressure but only by the pressure field (i.e., P_i in Eq. (2.1)) changes on the vehicle envelope.

In terms of UFP infiltration, the leakage at the side doors is not of great concern, but the leakage at the rear trunk is important. When a vehicle is driven at a high speed, the vehicle creates relatively low pressure field (i.e., $P_{in\text{-}cabin} > P_i$) on the side door thereby creates positive differential pressures in the cabin (dP_1, dP_2, and dP_3 in Figure 2.5). Thus, the low surface pressure field at high speed prevents UFP infiltration through the leakage at the side doors

regardless of vehicle type. In contrast, the positive pressure field at the gap of the rear trunk creates a negative differential pressure shown as dP_4 (i.e., $dP_4 < 0$) in both vehicle types. It indicates that UFP infiltration occurs through the leakage route at rear trunk under the RC mode. The following section 2.4.4. *UFP Infiltration under the Mobile Condition* discusses more in detail with more experimental evidences of infiltrated UFPs.

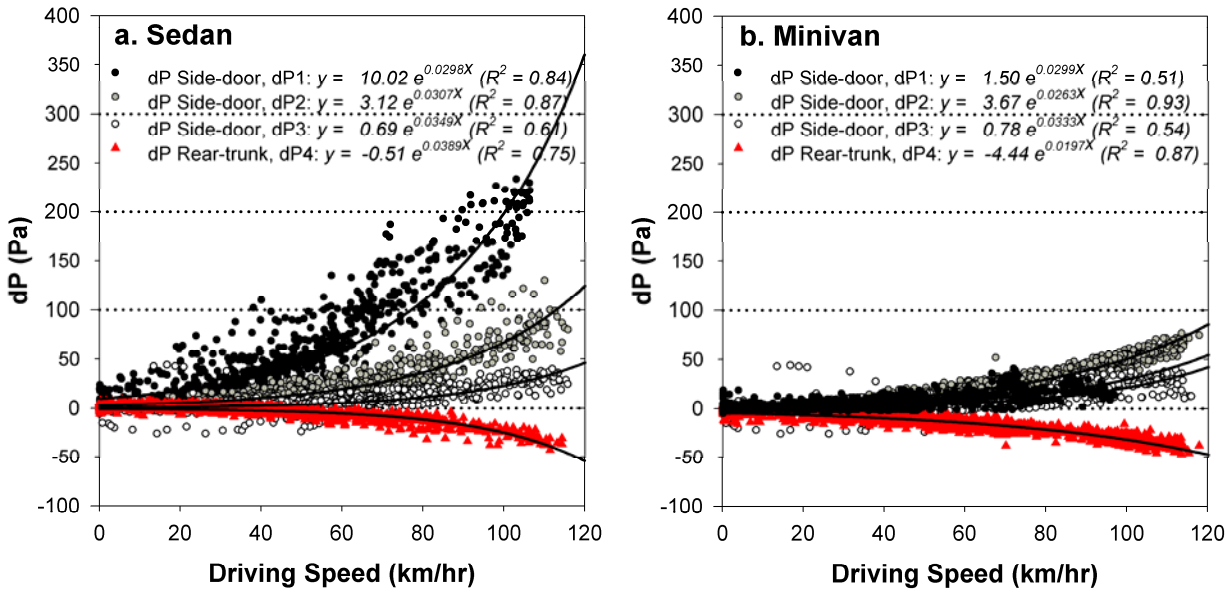


Figure 2.5 Aerodynamic differential pressure changes as a function of the driving speed
The differential pressure data at four different leakage locations (see Figure 2.1), three on the side door (i.e., dP_1, dP_2, and dP_3) and one on the rear trunk (i.e., dP_4), are plotted as a function of the driving speed. The data are presented with 1-second data for two distinctive vehicle types: (a) sedan (2008 Scion tC) and (b) minivan (2010 Honda Odyssey). The different schemes of symbols and colors indicate the differential pressure monitored at the four locations, and the regression data (lines) are also provided for each dataset.

Furthermore, the infiltration could be more significant when the driving speed increases

because of the exponential increase in the negative differential pressure (dP_4) regardless of vehicle shape. The two distinctive vehicle shapes (i.e., sedan and mini-van) had similar results in terms of the magnitude of increase in the differential pressure at the rear trunk (i.e., dP_4 approximately by 50 Pa) as a function of the driving speed. Therefore, when a vehicle is moving faster, the infiltration rate of UFPs through the leakage of the rear trunk is expected to increase as well, and consequently the passenger cabin environment becomes more vulnerable to on-road UFPs.

2.4.4. Ultrafine Particle Infiltration under the Mobile Condition

Figure 2.6 provides the RC mode test results under mobile condition for a sedan (Figures 2.6a, b, and c) and a mini-van (Figures 2.6d, e, and f). Figures 2.6a and 2.6d illustrate the driving speed in dark gray as a function of time during each test. The speed ranges from 0 to 120 km/hr. The three highest peaks of the driving speed refer to the maximum driving speed achieved on the freeway during the three repeated trips in a ventilation mode / fan setting combination (i.e., either RC-Qoff or RC-Q4). The remaining peaks with a lower magnitude represent the driving speed on local streets. While maintaining the RC mode during the testing, the fan was set to either Qoff or Q4 to simulate two extremely fan conditions.

Figure 2.6b (sedan) and Figure 2.6e (mini-van) illustrate the differential pressure changes at the side door (solid red line, dP_2) and at the rear trunk (dotted red line, dP_4) and the ventilation flow rates (blue, Q_{vent}) under the two ventilation mode / fan settings. The ventilation flow rates remained relatively constant at a certain flow rate depending on the fan settings because the RC mode (i.e., closed air damper) prevents passive ventilation through the ventilation systems. As mentioned in Figure 2.5, the differential pressures on the side door and rear trunk was affected by the driving speed and the changes of the negative differential pressure at the rear trunk leakage (dP_4) also track the changes of driving speed.

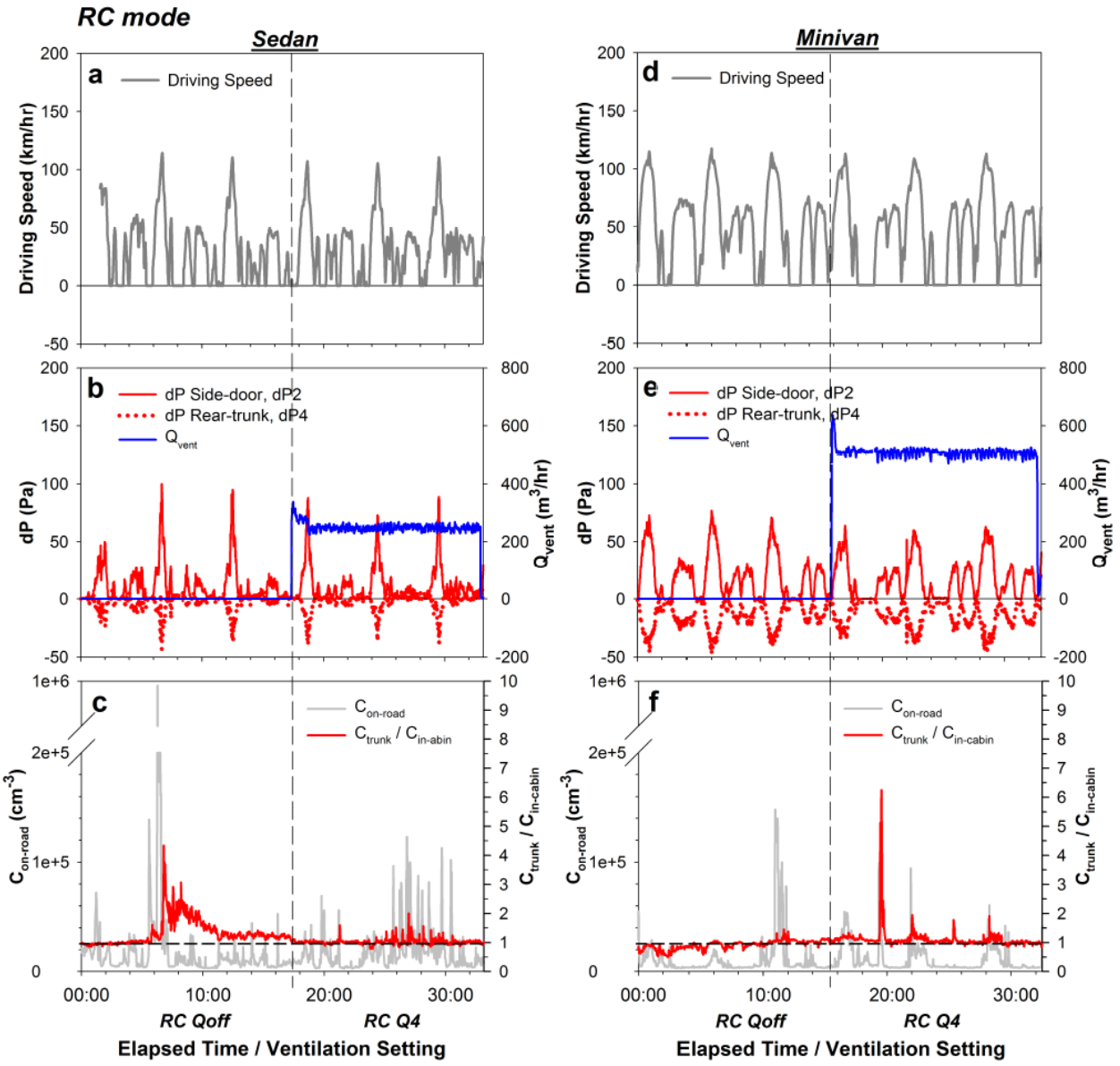


Figure 2.6 Observation of ultrafine particle infiltration in recirculation mode

In the RC mode, the driving speed (panels a, d) and the differential pressure and ventilation air flow rates (panels b, e) are plotted in time and compared between a sedan (2008 Toyota Scion tC on the left) and a minivan (2010 Honda Odyssey on the right). The bottom two panels (panels c, f) provide the corresponding particle number concentrations: on-road particle number concentration ($C_{on\text{-}road}$) measurements (gray) and the ratio of measured concentrations at trunk and at the center of cabin (C_{trunk} / $C_{in\text{-}cabin}$, red). All parameters are presented with 1-second data.

Figure 2.6c (sedan) and Figure 2.6f (mini-van) present the ratio of concentrations measured at the trunk gap and in-cabin (red, C_{trunk} / $C_{in\text{-}cabin}$) in a time series in comparison with the concurrent measurements of the on-road ambient UFP concentrations (gray, $C_{on\text{-}road}$). During the test, C_{trunk} was highly fluctuating above $C_{in\text{-}cabin}$ independent from the overall decay of $C_{in\text{-}cabin}$ under RC mode. The oscillation of the C_{trunk} / $C_{in\text{-}cabin}$ ratio was induced by the C_{trunk}. Since there was no emission source in the passenger cabin, the UFP infiltration through the rear trunk gap likely cause significant fluctuations of C_{trunk} and C_{trunk} / $C_{in\text{-}cabin}$ ratio. When the C_{trunk} / $C_{in\text{-}cabin}$ ratio is greater than 1.0, it serves as an indicator of UFP infiltration

The data collected under the RC-Qoff mode of the sedan (Figure 2.6c) and the RC-Q4 mode of the mini-van (Figure 2.6f) provide experimental evidence of UFP infiltration. The peaks of the C_{trunk} / $C_{in\text{-}cabin}$ ratio in the RC-Qoff mode of the sedan (Figure 2.6c) and the RC-Q4 mode of the mini-van (Figure 2.6f) clearly demonstrated that the C_{trunk} are 4- and 6-folds higher than $C_{in\text{-}cabin}$. The spikes in the C_{trunk} / $C_{in\text{-}cabin}$ ratio were typically observed when the following two criteria were met: (1) the differential pressure at the rear trunk (dP_4) was highly negative and (2) the $C_{on\text{-}road}$ was significantly higher than $C_{in\text{-}cabin}$. For instance, in the case of RC-Q4 of the sedan and RC-Qoff of the minivan (Figures 2.6c and f), the magnitude of the C_{trunk} / $C_{in\text{-}cabin}$ ratio was not as high as the previous two cases (i.e., the RC-Qoff mode of the sedan and RC-Q4 of the minivan in Figures 2.6c and f) for two reasons. For RC-Q4 of the sedan (Figure 2.6c), the small

cabin volume resulted in a high in-cabin air turn-over leading to more filtration under the RC mode; therefore, the C_{trunk} / $C_{in\text{-}cabin}$ ratio remained low in magnitude for the RC-Q4 mode of the sedan. However, in the case of RC-Qoff mode of the mini-van (Figure 2.6f), the C_{trunk} / $C_{in\text{-}cabin}$ ratio remained low in magnitude simply because the $C_{on\text{-}road}$ was much lower than the $C_{in\text{-}cabin}$ for most of the testing period. It is worth noting that under RC-Qoff, the $C_{in\text{-}cabin}$ decreases mostly by air exchange via infiltration, which is much smaller than the air exchange using mechanical ventilation. For that reason, the $C_{in\text{-}cabin}$ remained higher than the $C_{on\text{-}road}$.

Under OA mode, cabin pressurization can prevent UFP infiltration. In comparison to the RC mode, the OA mode data were also collected in a similar manner and presented in Figure 2.7. Under the OA mode, the C_{trunk} / $C_{in\text{-}cabin}$ ratio remained near 1.0 with minimal standard deviation (± 0.12) despite of aerodynamic differential pressure changes on the vehicle envelope. The only exception was the OA-Qoff of minivan in which the passive ventilation air flow rate could not achieve enough in-cabin pressure to compensate the surface pressure at the rear trunk (dP_4). In result, the C_{trunk} / $C_{in\text{-}cabin}$ ratio reached up to 9.

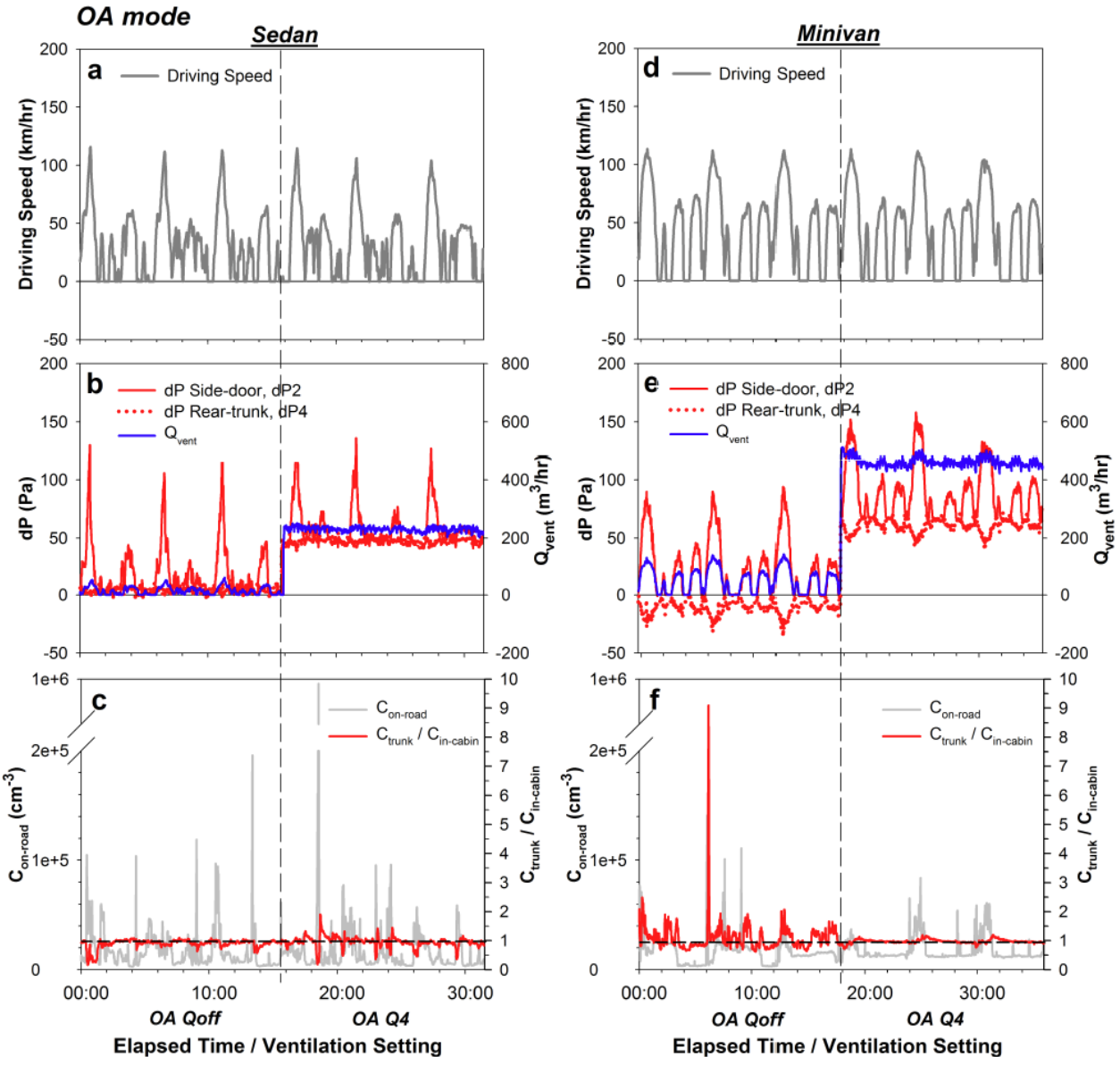


Figure 2.7 Observation of ultrafine particle infiltration in outdoor air mode

In the OA mode, the driving speed (panels a, d) and the differential pressure and ventilation air flow rates (panels b, e) are plotted in time and compared between a sedan (2008 Toyota Scion tC on the left) and a minivan (2010 Honda Odyssey on the right). The bottom two panels (panels c, f) provide the corresponding particle number concentrations: on-road particle number concentration ($C_{on\text{-}road}$) measurements (gray) and the ratio of measured concentrations at trunk and at the center of cabin (C_{trunk} / $C_{in\text{-}cabin}$, red). All parameters are presented with 1-second data.

In summary, the infiltration flow through the rear trunk leakage physically occurs when the negative differential pressure at the rear trunk (dP_4) becomes large in magnitude. It also depends on the $C_{on\text{-}road}$; that is, the $C_{in\text{-}cabin}$ is significantly influenced when the $C_{on\text{-}road}$ is much higher than the $C_{in\text{-}cabin}$. Even with the high blower fan setting used in the RC-Q4 mode (i.e., highly repeated filtration) for the small-cabin volume sedan, the infiltrated UFPs were observed at the rear trunk leakage but at a reduced magnitude. From these observations, UFP infiltration is a dynamic process which depends on the surface pressure at the rear trunk leakage, in-cabin pressure, and the ambient concentration on the roadway. Properly maintained cabin pressurization can prevent the UFP infiltration into the passenger cabin.

References

(1) Morawska, L.; Ristovski, Z.; Jayaratne, E. R.; Keogh, D. U.; Ling, X. Ambient nano and ultrafine particles from motor vehicle emissions: Characteristics, ambient processing and implications on human exposure. *Atmospheric Environment* **2008**, *42*, 8113-8138.

(2) Knibbs, L. D.; de Dear, R. J.; Morawska, L.; Mengersen, K. L. On-road ultrafine particle concentration in the m5 east road tunnel, sydney, australia. *Atmospheric Environment* **2009**, *43*, 3510-3519.

(3) Park, J. H.; Spengler, J. D.; Yoon, D. W.; Dumyahn, T.; Lee, K.; Ozkaynak, H. Measurement of air exchange rate of stationary vehicles and estimation of in-vehicle exposure. *Journal of Exposure Analysis and Environmental Epidemiology* **1998**, *8*, 65-78.

(4) Chan, L. Y.; Lau, W. L.; Zou, S. C.; Cao, Z. X.; Lai, S. C. Exposure level of carbon monoxide and respirable suspended particulate in public transportation modes while commuting in urban, area of guangzhou, china. *Atmospheric Environment* **2002**, *36*, 5831-5840.

(5) Esber, L. A.; El-Fadel, M.; Nuwayhid, I.; Saliba, N. The effect of different ventilation modes on in-vehicle carbon monoxide exposure. *Atmospheric Environment* **2007**, *41*, 3644-3657.

(6) Xu, B.; Liu, S. S.; Liu, J. J.; Zhu, Y. F. Effects of vehicle cabin filter efficiency on ultrafine particle concentration ratios measured in-cabin and on-roadway. *Aerosol Science and Technology* **2011**, *45*, 234-243.

(7) Zhu, Y. F.; Eiguren-Fernandez, A.; Hinds, W. C.; Miguel, A. H. In-cabin commuter exposure to ultrafine particles on los angeles freeways. *Environmental Science & Technology* **2007**, *41*, 2138-2145.

(8) Fruin, S.; Westerdahl, D.; Sax, T.; Sioutas, C.; Fine, P. M. Measurements and predictors of on-road ultrafine particle concentrations and associated pollutants in los angeles. *Atmospheric Environment* **2008**, *42*, 207-219.

(9) Ott, W.; Klepeis, N.; Switzer, P. Air change rates of motor vehicles and in-vehicle pollutant concentrations from secondhand smoke. *Journal of Exposure Science and Environmental Epidemiology* **2008**, *18*, 312-325.

(10) Knibbs, L. D.; de Dear, R. J.; Atkinson, S. E. Field study of air change and flow rate in six automobiles. *Indoor Air* **2009**, *19*, 303-313.

(11) Hudda, N.; Eckel, S. R.; Knibbs, L. D.; Sioutas, C.; Delfino, R. J.; Fruin, S. A. Linking in-vehicle ultrafine particle exposures to on-road concentrations. *Atmospheric Environment* **2012**, *59*, 578-586.

(12) Fruin, S. A.; Hudda, N.; Sioutas, C.; Defino, R. J. Predictive model for vehicle air exchange rates based on a large, representative sample. *Environmental Science & Technology* **2011**, *45*, 3569-3575.

(13) Saber, E. M.; Bazargan, M. Dynamic behavior modeling of cigarette smoke particles inside the car cabin with different ventilation scenarios. *International Journal of Environmental Science and Technology* **2011**, *8*, 747-764.

(14) Xu, B.; Liu, S.; Zhu, Y. Ultrafine particle penetration through idealized vehicle cracks. *Journal of Aerosol Science* **2010**, *41*, 859-868.

(15) ASHRAE *Ashrae handbook: 2005 fundamentals*; American Society of Heating, Refrigerating, and Air-Conditioning Engineers: Atlanta, GA, 2005.

(16) ASTM, *E779-10 standard test method for determining air leakage rate by fan pressurization*; ASTM International: West Conshohocken, PA, 2010.

(17) Fletcher, B.; Saunders, C. J. Air change rates in stationary and moving motor-vehicles. *Journal of Hazardous Materials* **1994**, *38*, 243-256.

(18) Song, K. S.; Kang, S. O.; Jun, S. O.; Park, H. I.; Kee, J. D.; Kim, K. H.; Lee, D. H. Aerodynamic design optimization of rear body shapes of a sedan for drag reduction. *International Journal of Automotive Technology* **2012**, *13*, 905-914.

(19) U.S. EPA Fuel economy database, 2012. http://www.fueleconomy.gov/feg/download.shtml (accessed Sep 7, 2012).

(20) ASTM, *E1827-11 standard test methods for determining airtightness of buildings using an orifice blower door*; ASTM International: West Conshohocken, PA, 2011.

(21) Joodatnia, P.; Kumar, P.; Robins, A. Fast response sequential measurements and modelling of nanoparticles inside and outside a car cabin. *Atmospheric Environment* **2013**, *71*, 364-375.

3. IN-CABIN ULTRAFINE PARTICLE TRANSPORT

3.1. Abstract

Existing in-cabin ultrafine particle (UFP) dynamic models do not account for passive ventilation and infiltration through the vehicle envelope. This study developed passive ventilation and infiltration models and coupled them to a dimensionless pseudo-steady-state model. The model predictions were validated with literature data and with field measurements from 10 vehicle models. The proposed model can simulate in-cabin air quality over time under a wide range of driving speed and ventilation condition. It shows infiltration would only occur above a certain driving speed depending on in-cabin pressure and vehicle type. The model predicts that UFP in-cabin/on-road concentrations ratio (I/O) would increase substantially with respect to driving speed due to infiltration and passive ventilation. Application of higher fan settings in outdoor air (OA) mode (i.e., higher cabin pressurization) minimizes the effects of infiltration and passive ventilation. However, active OA (mechanical) ventilation leads to a higher air exchange which usually results in a higher I/O ratio. A parametric analysis found the fractional impacts of different UFP gain/loss mechanisms on I/O ratios changed dynamically as a function of driving speed.

3.2. Introduction

Ultrafine particles (UFPs, diameter < 100 nm) constitute a significant health concern due to their adverse health effects. Elevated ambient UFP concentrations have been associated with pulmonary[1-3] and cardiovascular diseases.[4,5] Because UFPs originate primarily from traffic emissions in urban environments,[6] high UFP concentrations have been frequently observed on the roadway. In outdoor air (OA) mode, the UFP concentration is usually an order of magnitude higher in the passenger cabin even with a cabin air filter, than in the urban background.[7] High levels of passenger exposure occur because of high air exchange rates (AERs),[8,9] low filter efficiency,[10,11] and vehicle envelope leakage.[12,13] Despite a short commuting time of 1.3 h/day on average[14], commuting exposure alone may contribute up to 45-50% of the total UFP daily exposure.[15,16]

In order to quantify UFP transport in passenger cabins, previous modeling studies have proposed a dimensionless in-cabin UFP model. However, the previous models often neglected infiltration terms[17] or required difficult measurements for the infiltration air-flow rate.[18] Because infiltration typically occurs through unknowingly distributed leakage on the vehicle envelope, direct instrumental measurements are not experimentally feasible for the infiltration air-flow rates. The aerodynamic surface pressure on the moving vehicle substantially increases with driving speed[19] and, as anticipated, changes the infiltration air-flow rate. To incorporate

infiltration as a function of driving speed, an idealized leakage model[20] has been utilized.[21,22] However, application of this model is also limited because the required model inputs include difficult measurements of leakage geometry dimensions and infiltration air-flow rates as a function of driving speed.

In addition, previous studies reported a linear increase in ventilation air-flow and/or air exchange with increasing speed due to passive ventilation;[23-25] however, the passive ventilation has not been incorporated in the previous modeling approaches. Up to date, there is no in-cabin UFP model allowing for quantitative analysis including the effects of infiltration and passive ventilation.

This study formulated semi-empirical models for infiltration and passive ventilation and incorporated them in a dimensionless pseudo-steady-state in-cabin UFP model. The proposed model allows for the dynamic simulation of in-cabin UFPs as a function of driving speed under any ventilation condition in time. Using the proposed model, this study elucidated the effects of infiltration and passive ventilation as a function of driving speed and discussed their overall impacts on the in-cabin air quality. This study further evaluated the parametric significance of different particle gain/loss mechanisms, including active and passive OA ventilation, recirculation (RC) filtration, infiltration, and surface deposition.

3.3. Methods

3.3.1. In-cabin Ultrafine Particle Gain / Loss Mechanisms

In-cabin UFP transport is governed largely by the following five mechanisms: (1) active OA ventilation, (2) passive OA ventilation, (3) RC filtration, (4) infiltration, and (5) surface deposition. Depending on ventilation conditions (i.e., the selection of OA/RC modes and fan settings), different mechanisms control in-cabin air quality. For example, under the stationary OA mode, in-cabin concentrations are determined by active OA ventilation, infiltration, and surface deposition. When the vehicle is moving under OA mode (i.e., mobile OA mode), passive OA ventilation in addition to active OA ventilation also increases the amount of air supply through the ventilation system while infiltration and surface deposition still occur. However, under RC mode, there is little passive ventilation if the mechanical air damper is closed and the same cabin air repeatedly circulates in the cabin. In this case, RC filtration consequently reduces the in-cabin UFP concentration while infiltration and surface deposition still exist. UFP uptake by passenger inhalation is negligible because the breathing rate is much smaller than the airflow rate of the vehicle.[22]

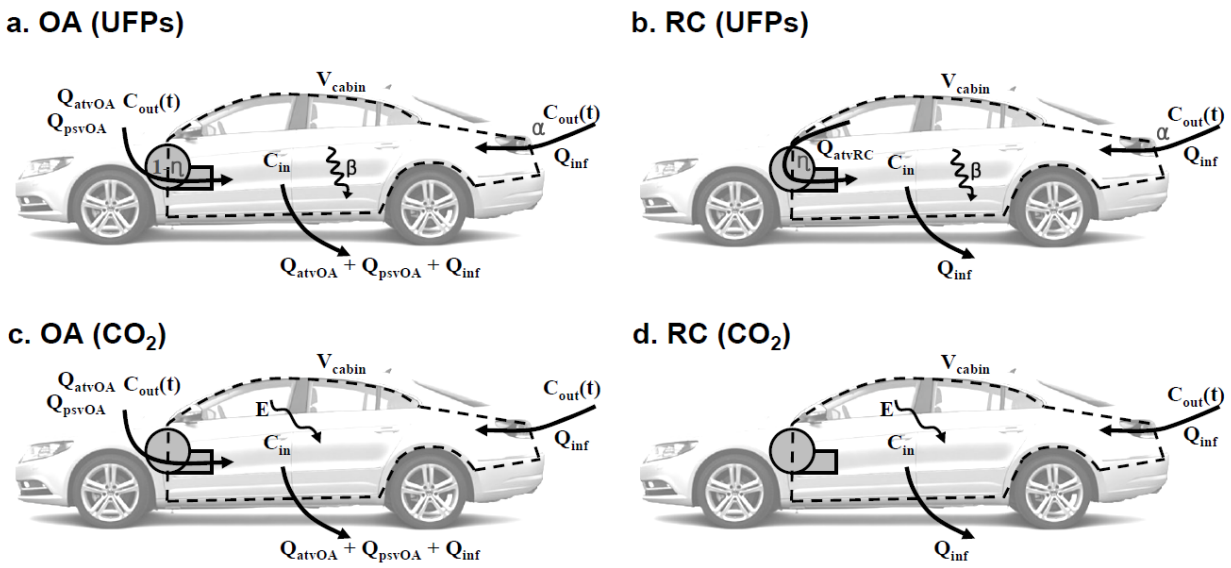


Figure 3.1 Graphical illustrations of the modeling domain and modeling parameters
Graphical illustrations indicate the modeling parameters for UFPs and CO_2 in the same modeling domain (V_{cabin}, dash-line) in the outdoor air (OA) mode (a, c) and the recirculation (RC) mode (b, d). The arrows indicate air flow paths.

3.3.2. Model Development

Figure 3.1 illustrates the modeling parameters for particles and gas (i.e., UFPs and CO_2) under different ventilation conditions. Upon the selection of UFPs/CO_2 and OA/RC for the model, the model considers different modeling parameters affecting the in-cabin concentration (C) inside the passenger cabin volume (V_{cabin}). The active ventilation air-flow rate (Q_{atvOA}) is determined by fan settings for UFPs in OA mode under stationary conditions (see Figure 3.1a), and the passive ventilation air-flow rate (Q_{psvOA}) is a linear function of driving speed ($v_{driving}$).[23-25] The sum of the two air-flow rates (i.e., $Q_{atvOA} + Q_{psvOA}$) supplies OA to the manufacture installed

cabin air filter whose efficiency (η = 40% in this study) ranges from 20 to 80%. [11,17] In the passenger cabin, particle loss occurs via a surface deposition mechanism described by the deposition rate (β = 8 h^{-1})[26] until the cabin air is exhausted through the leakage around the vehicle envelope.

Infiltration is modeled with the infiltration air-flow rate (Q_{inf}). Infiltration is independent of the selection of OA/RC mode but is dependent on two competing pressures: cabin pressure and aerodynamic pressure changes on the vehicle surface (discussed in more detail below). For UFPs in RC mode, the RC-mode ventilation air-flow rate (Q_{atvRC}) replaces both Q_{atvOA} and Q_{psvOA}. RC-mode ventilation only works as the UFP sink due to repeated filtration. The only UFP penetration route in this scenario is infiltration. The particle penetration loss partitioning coefficient (α = 0.6)[21] is also applied to Q_{inf} for UFP infiltration.

Similar to the UFP model (Figure 3.1a and b), the CO_2 model incorporates the same air-flow rates (Q_{atvOA} and Q_{psvOA}) in OA mode (Figure 3.1c) and Q_{inf} in RC mode (Figure 3.1d). The parameter η disappears because the automotive filtration system does not allow for gas removal. Instead, the CO_2 emission rate (E) from passenger exhalation is considered.

Table 3.1 A summary of the modeling equations for particle and gas under different ventilation modes

$\frac{dC_{in}}{dt} = S - L \cdot C_{in}$		**Source Term (*S*)**	**Loss Term (*L*)**
UFPs	OA	$C_{out}(t) \cdot \left\{ (1-\eta) \cdot \left(\frac{Q_{atvOA} + Q_{psvOA}}{V_{cabin}} \right) + \alpha \cdot \frac{Q_{\inf}}{V_{cabin}} \right\}$	$\frac{Q_{atvOA} + Q_{psvOA} + Q_{\inf}}{V_{cabin}} + \beta$
	RC	$C_{out}(t) \cdot \alpha \cdot \frac{Q_{\inf}}{V_{cabin}}$	$\eta \cdot \frac{Q_{atvRC}}{V_{cabin}} + \frac{Q_{\inf}}{V_{cabin}} + \beta$
CO_2	OA	$C_{out}(t) \cdot \left(\frac{Q_{atvOA} + Q_{psvOA} + Q_{\inf}}{V_{cabin}} \right) + \frac{E}{V_{cabin}}$	$\frac{Q_{atvOA} + Q_{psvOA} + Q_{\inf}}{V_{cabin}}$
	RC	$C_{out}(t) \cdot \frac{Q_{\inf}}{V_{cabin}} + \frac{E}{V_{cabin}}$	$\frac{Q_{\inf}}{V_{cabin}}$

3.3.3. Modeling Assumptions

The dimensionless pseudo-steady-state modeling approach includes three assumptions: well-mixed conditions, no temperature effect, and no UFP phase change by coagulation, condensation, and evaporation. The well-mixed condition is valid in consideration of high ventilation air-flow rates (i.e., up to 600 m^3/h) in a small cabin volume (approximately 3 m^3 for a sedan and 7 m^3 for a minivan). Experimental studies also support the well-mixed in-cabin condition from in-cabin UFP concentration measurements at widely distributed sampling

locations in the passenger cabin.[25,27] The assumption of no temperature effect has also been demonstrated previously.[23] For simplicity, no phase change is assumed for the UFPs, making the material balance applicable to the UFP number concentration. Air exchange rate is approximately 12 and 13 orders of magnitude higher than thermal coagulation rate of typical in-cabin particles in RC and OA modes, respectively. However, the particle phase change can also occur by kinematic coagulation, condensation, and evaporation. This study evaluated the no phase change assumption later. Corresponding to the modeling schematics in Figure 3.1, Table 3.1 summarizes the modeling equations developed for this study and provides different equations for the OA/RC scenario with UFPs and CO_2.

3.3.4. Driving-speed-dependent Sub-models

Two input parameters that change dynamically with respect to driving speed are infiltration air-flow rate (Q_{inf}) and passive ventilation air-flow rate (Q_{psvOA}). Because infiltration occurs when the cabin pressure (dP_{mech}) is lower than the aerodynamic pressure (dP_{aero}) on the moving vehicle surface, the differential pressure affecting infiltration (dP_{inf}) is determined by the difference between the two competing pressures, dP_{mech} and dP_{aero}.

As demonstrated in cabin pressurization tests of a previous study,[19] ventilation air-flow

rate (Q_{vent}) in OA mode becomes a power-law function with respect to differential pressure (dP_{mech}) and it is given as followed:

$$Q_{vent} = C_f \cdot dP_{mech}{}^{n} \tag{3.1}$$

where C_f is the leakage flow coefficient, n is the pressure exponent. C_f and n are vehicle model-specific properties describing envelope leakage characteristics. The values can be obtained from the power-law regression with the measurements of Q_{vent} and dP_{mech} in stationary condition (i.e., cabin pressurization test).[19,23] Table 3.2 summarized C_f and n.

When a vehicle is moving, dP_{mech} increases because of OA ventilation air-flow rate (Q_{atvOA}) and passive ventilation air-flow rate (Q_{psvOA}). Thus, the following equation describes the level of cabin pressurization (i.e., dP_{mech}) in driving conditions.

$$dP_{mech} = e^{\frac{1}{n}\ln\left(\frac{Q_{atvOA}+Q_{psvOA}}{C_f}\right)} \tag{3.2}$$

Independent from dP_{mech}, the aerodynamic pressure (dP_{aero}) on the vehicle surface can also take place during driving. The dP_{aero} were previously derived from the regression of the differential pressure measurements.[19] The aerodynamic differential pressure (dP_{aero}) is given as a function of driving speed ($v_{driving}$) as followed:

$$dP_{aero} = C_p \cdot a \cdot e^{b \cdot v_{driving}} \tag{3.3}$$

where C_p is the infiltration pressure distribution coefficient. The magnitude of the exponential increase in dP_{aero} is slightly different depending on the aerodynamic design or shape of the

vehicle. The two coefficients (i.e., a and b) in the dP_{aero} term of Eq. (3.3) accordingly become 0.51 and 0.04 for a sedan and 4.44 and 0.02 for a minivan.[19]

Infiltration occurs when dP_{aero} is greater than dP_{mech}. Therefore, dP_{inf} can take the following form:

$$dP_{\text{inf}} = \underbrace{C_p \cdot a \cdot e^{b \cdot v_{driving}}}_{dP_{aero}} - \underbrace{e^{\frac{1}{n}\ln\left(\frac{Q_{atvOA}+Q_{psvOA}}{C_f}\right)}}_{dP_{mech}} \tag{3.4}$$

Previous studies have found that AER due to passive ventilation (AER_{psvOA}) is a linear function of $v_{driving}$ given as followed:[23,25]

$$AER_{psvOA} = C_{psv} \cdot v_{driving} \tag{3.5}$$

where C_{psv} is the passive ventilation coefficient. C_{psv} was found to be 0.21 from the measurements on five vehicle models, which were different from the 10 vehicle models used for model validation. This coefficient is in good agreement with previous studies (see Figure 3.2). Whereas dP_{aero} is always present under driving conditions, the OA-mode dP_{mech} remains positive due to cabin pressurization by Q_{atvOA} and Q_{psvOA}. Thus, in OA mode, the two competing pressures (i.e., dP_{aero} and dP_{mech}) depend on changes in the driving speed of a moving vehicle. In RC mode, dP_{mech} is equal to zero regardless of $v_{driving}$ because RC mode ventilation does not pressurize the passenger cabin.[19] Thus, only dP_{aero} determines the differential pressure affecting infiltration (dP_{inf}) in RC mode.

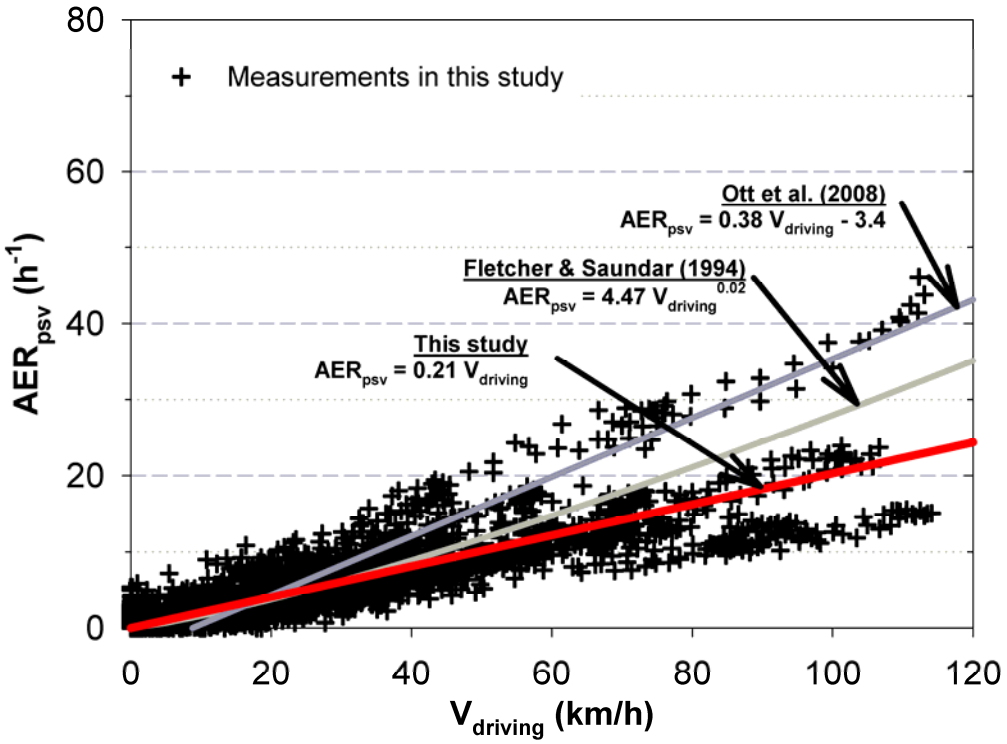


Figure 3.2 Linear function of passive ventilation air exchange rates with respect to driving speed The passive ventilation air exchange rates (AER_{psv}) at a wide range of driving speed ($V_{driving}$) are plotted for this study and compared to the previous findings in Fletcher and Saundar (1994) and Ott et al. (2008). In comparison to the previous studies, the AER_{psv} in this study excluded the effects of infiltration so the AER is slightly lower in magnitude.

With the use of dP_{inf}, Q_{inf} is expressed as follows:

$$Q_{\text{inf}} = C_{rev} \cdot C_f \cdot dP_{\text{inf}}{}^{n} \tag{3.6}$$

where C_{rev} is the reverse leakage flow correction factor (C_{rev} = 0.65) adopted from a previous study.[23] The C_{rev} accounts for the differences between infiltration and exfiltration. The C_f and n are the parameters resulting from cabin pressurization consequently leading to exfiltration. Infiltration flow occurs in the reverse direction and experiences higher magnitude of resistance

thereby allowing approximately 65% of exfiltration flow rate.[23] Accordingly, the relationship must be corrected with C_{rev} because the infiltration flow occurs in the reverse direction.

3.3.5. Model Calibration

The proposed model was calibrated via C_p of Eq. (3.3) from the CO_2 measurements in RC mode. Since C_p determines infiltration air-flow rate, it is desirable to calibrate the model with C_p in RC mode when air exchange only occurs by infiltration air-flow. Under mobile RC conditions, infiltration occurs only due to the changes in dP_{aero} because there is no cabin pressurization by dP_{mech}. Instead of using UFPs for calibration, the use of CO_2 minimizes the uncertainty that might arise from the assumption of no phase change for UFPs.

The Eq. (3.3) was derived from the continuous measurement of dP_{aero} changes on the lateral-center of the rear trunk gap,[19] where infiltration is most significant.[28] Accordingly, the overall aerodynamic pressure affecting dP_{inf} is lower than the measurements but the measurements of aerodynamic pressures are not feasible across the widely spread rear-trunk leakage. Thus, C_p is not a measureable parameter. After comparing the simulation results with the CO_2 measurement data in RC mode, the optimal C_p was determined to be 0.33 and 0.23 for a sedan and a minivan, respectively. Finally, the calibrated model with the optimal C_p was validated with *in situ* measurement data collected in 10 different vehicle models.

Table 3.2 A summary of the test vehicle models and specifications

Category	ID	Model	Year	Mileage (km)	Cabin Volume (m^3)	Flow Coefficient (C_f)	Pressure Exponent (n)
Hatchback	1	Toyota Prius	2012	9102	3.88	46.83	0.81
Sedan	2	Ford Focus	2012	51347	2.94	18.78	0.82
	3	Honda Accord	2011	51194	3.83	69.39	0.49
	4	Hyundai Sonata	2013	21712	3.41	40.58	0.69
	5	Nissan Sentra	2012	30398	3.50	6.73	0.82
	6	Toyota Camry	2012	1931	3.78	61.49	0.48
	7	VW Jetta	2012	14917	3.55	29.77	0.75
SUV	8	Ford Explorer	2013	16510	4.89	17.66	0.89
	9	Toyota Highlander	2012	10611	4.43	60.09	0.56
Minivan	10	Toyota Sienna	2011	74174	5.76	72.12	0.53

3.3.6. Validation Data Collection

The proposed model was validated with the experimental measurement data acquired from testing 10 different vehicle models (see Table 3.2). Under stationary conditions, a cabin pressurization test was conducted to estimate the vehicle leakage properties (C_f and n) from the measurements of mechanical ventilation inlet air-flow rates in OA mode (i.e., Q_{atvOA}) with a ventilation meter (Q-Trak model 7565-X with model 960, TSI, Inc., St. Paul, MN). The associated differential pressure was measured with a manometer (Model HD755, Extech Instruments Co., Nashua, NH). The cabin pressurization test is described in more detail elsewhere.[29-31] Two condensation particle counters (CPCs) measured UFP number concentrations concurrently at two locations: in the center of the vehicle cabin (C_{in}) and outside for ambient/on-

road measurements (C_{out}). One of the CPCs (Model 3785, TSI, Inc., St. Paul, MN) monitored C_{in} while the other (Model 3786, TSI Inc., St. Paul, MN) monitored C_{out}. The CPC instruments were collocated before and after field sampling for data quality assurance. The driving speed and coordinates were logged by a GPS unit (Model BT-Q1000XT, QStarz, Co. Ltd., Taiwan). Throughout the measurements and across vehicle models, the fan was set to the medium fan settings at which the numeric air-flow rate was measured for the model input.

Consequently, the proposed model takes the following input parameters: $\nu_{driving}$, C_{out} as a function of time (t), and the initial C_{in} at t = 0. With vehicle model-specific leakage parameter data C_f and n from a cabin pressurization test, the model outputs C_{in} predictions with respect to both time and driving speed for any vehicle model at any ventilation condition.

3.4. Results and Discussion

3.4.1. Model Validation

Figure 3.3 illustrates the comparisons between the model predictions and experimental measurement data from the 10 vehicle models representing a wide range of vehicle variations (i.e., model, age, type, and manufacturer). Model validation was also conducted at driving speeds ranging from 0 to 130 km/h. As shown in Figure 2a, the predicted in-cabin UFP model matches the experimental data well. The R^2 of 0.78 (for UFPs) and 0.83 (for CO_2) suggests high reliability for the model predictions of in-cabin concentrations.

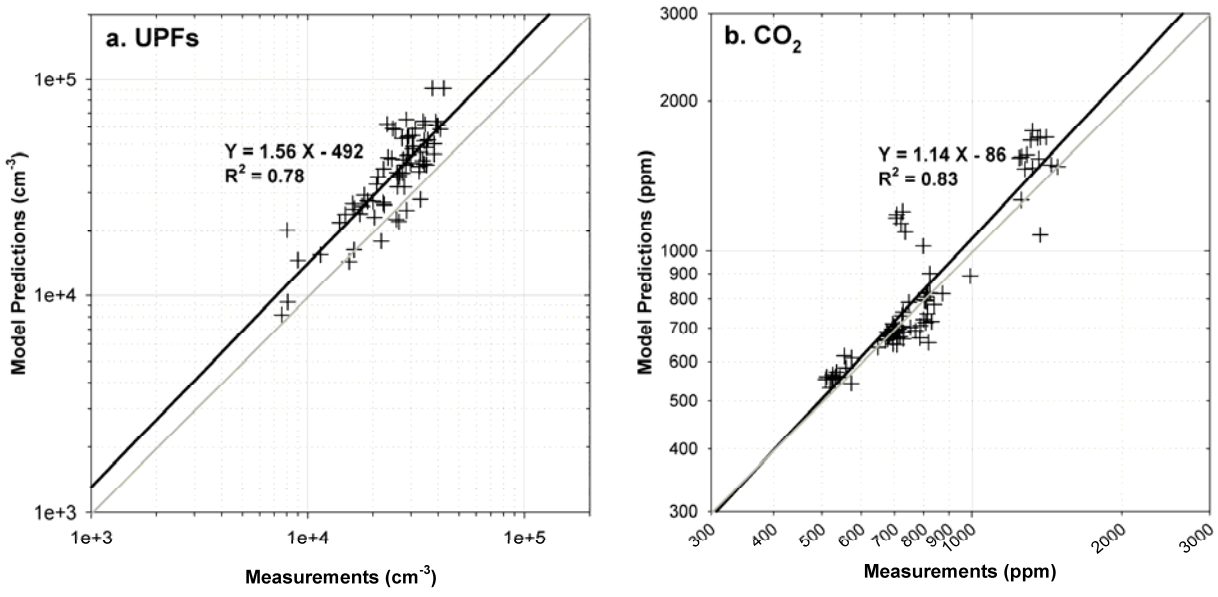


Figure 3.3 Empirical validation results of the proposed model for UFPs and CO_2

Figure 3.4 presents a sensitivity analysis for both UFPs and CO_2 at different concentrations. The model bias remains near zero for CO_2 at a wide range of concentrations in Figure 3b, suggesting the model is well calibrated for CO_2 and provides accurate air exchange estimates for the passenger cabin. However, the UFP model bias increases as particle number concentration increases in Figure 3.4a. This is presumably due to particle phase change mechanisms other than thermal coagulation such as kinematic coagulation, condensation and evaporation. Note that a high particle number concentration often constitutes a large fraction of nucleation mode particles subjected to a significant level of phase change. In addition, the UFP model bias can also increase at higher concentration because the surface deposition rate (β) is constant (i.e., 8 hr^{-1}) in this study. Although the median value of surface deposition rate was taken from Gong et al.[26], in-cabin UFP surface deposition can take place at different rate as a function of particle size, in-cabin surface area and material.

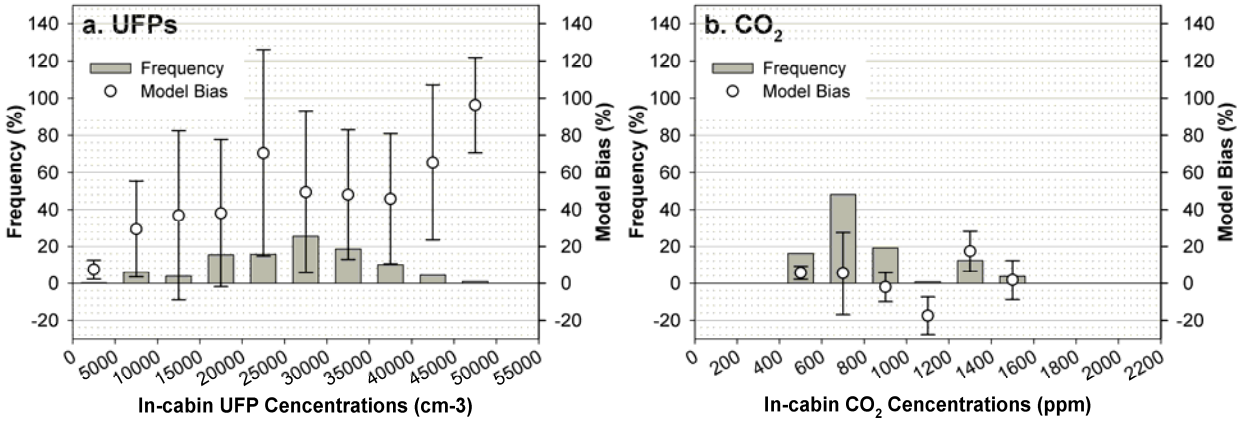


Figure 3.4 Concentration sensitivity of the proposed model for UFPs and CO_2

Histogram shows the frequency distributions of the in-cabin concentration observations. The proposed model bias (dot with error bars) are provided across the observed range of in-cabin concentrations for (a) UFPs and (b) CO_2.

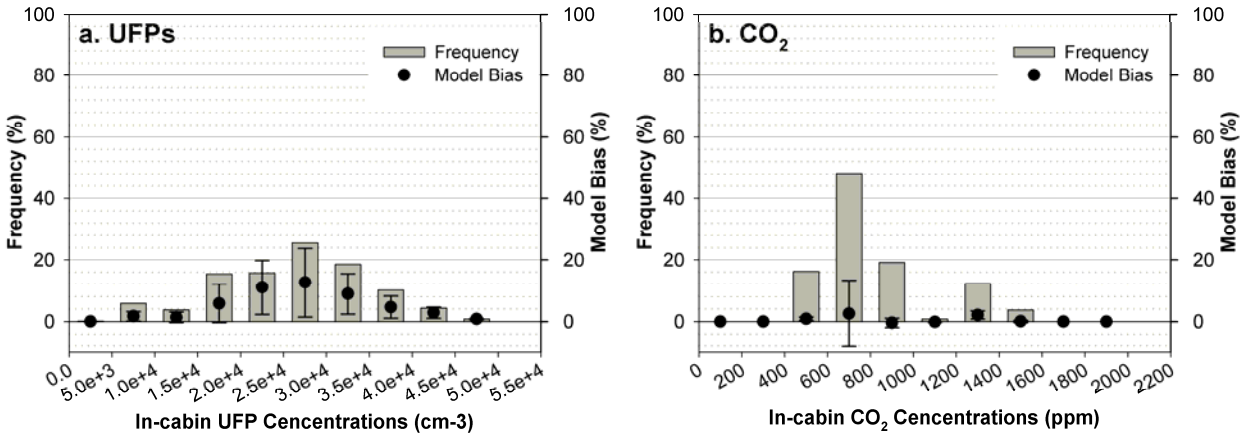


Figure 3.5 Model bias weighted by frequency distributions of the in-cabin measurements

Frequency distributions of the in-cabin measurements (histogram) and frequency-weighted model bias (dot with error bars) are provided across the observed range of in-cabin concentrations for (a) UFPs and (b) CO_2.

However, the in-cabin UFP concentration ranged widely from 7 x 10^3 to 5 x 10^4 cm^{-3} and high UFP number concentration is rarely observed. Taking into account the observed frequency distributions of in-cabin UFP concentrations, the overall model bias is below 16% throughout the concentration ranges as seen in Figure 3.4a. As of CO_2 in Figure 3.4b, the model bias is near zero. Therefore, the model provides reasonably good predictions with the maximum model bias of 16% for the in-cabin UFPs in a typical in-cabin environment. It offers even more accurate estimates for in-cabin CO_2 concentrations.

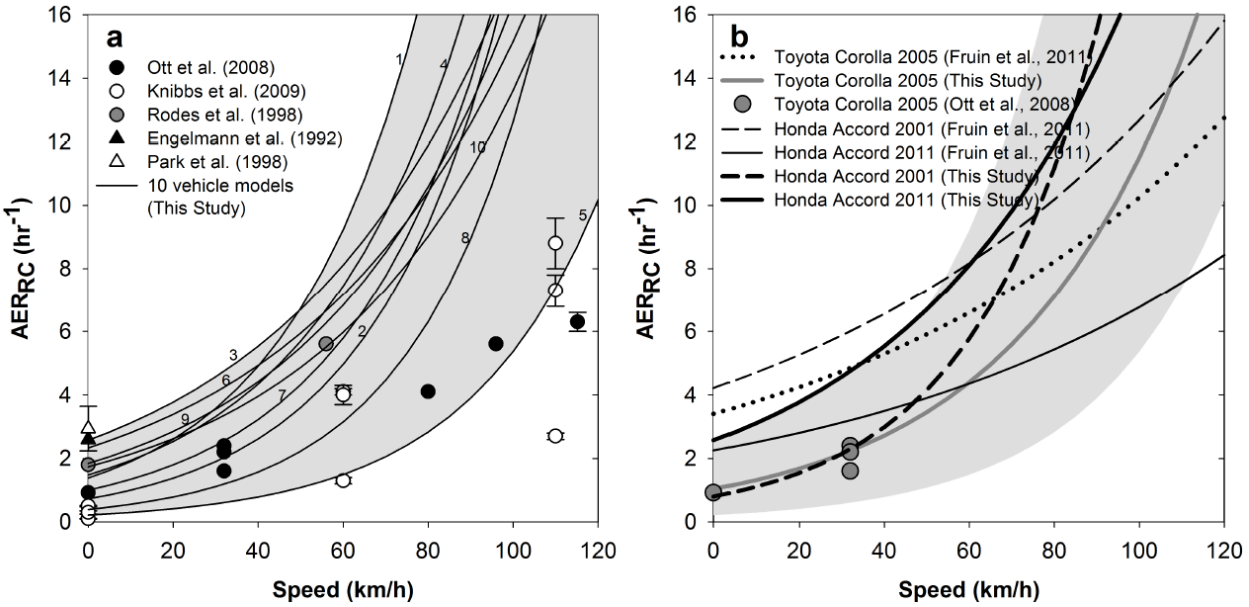


Figure 3.6 Recirculation mode air exchange rates as a function of driving speed
The model estimated RC-mode air exchange rates (AER_{RC}) (solid lines in panel a) are plotted as a function of driving speed and compared to the measurement data from previous studies. The numbers next to the solid lines refer to vehicle IDs listed in Table 3.2. AER_{RC} of specific vehicle model/year in this study are also compared to the measurement data from Ott et al. (2008) and model predictions from Fruin et al. (2011) in panel b.

3.4.2. Recirculation Mode Air Exchange Rates

The proposed model is developed primarily to predict in-cabin UFP concentrations (i.e., C_{in}); but it can also estimate RC-mode AERs (AER_{RC}) with respect to driving speed. RC mode air exchange occurs only by infiltration therefore AER_{RC} is equal to Q_{inf}/V_{cabin} under well-mixed conditions. Figure 3.6 shows the model predictions of AER_{RC} as a function of driving speed and compares with literature data. Figure 3.6a compared the model predictions in this study with experimental measurements in the literature.[8,25,32-34] As illustrated in Figure 3.6a, the modeling results for AER_{RC} are in reasonable agreement with experimental data in the literature. One should interpret this plot carefully because the test vehicles in the literature are different from the test vehicles in this study except for the 2005 Toyota Corolla.[25]

Specific to the 2005 Toyota Corolla, Figure 3.6b shows that the model predictions correspond well with the experimental observations from Ott et al.[25] for the same vehicle model at the same driving speed in spite of the vehicle age differences at the time of measurement in this study and Ott et al.[25]. Previously, Fruin et al.[35] statistically derived an AER_{RC} model which takes input parameters such as vehicle age and manufacturer. Both Fruin's and currently developed models predict that AER_{RC} increases exponentially at increasing driving speeds and agreed well with each other in an acceptable range. However, this study observed that the predicted AER_{RC} for individual vehicles could be different, possibly because automotive

envelope leakage is more specific to manufacturer's design changes in vehicle model than the actual vehicle age. For instance, at 60 km/h, the AER_{RC} in this study estimated 5.8 and 8.1 h^{-1} for the 2001 and 2011 models of the Honda Accord, respectively (Figure 3.6b). However, at the same driving speed, the Fruin's AER_{RC} model provided corresponding values of 8.2 and 4.4 h^{-1}, respectively. The plots in Figure 3.6b provide AER_{RC} across a wide range of driving speed in detail.

Potential causes of these differences may be due to the nature of the different approaches. The previous AER_{RC} model was derived from statistical regressions assuming that the vehicle age has significant effects on AER_{RC}. Whereas, the AER_{RC} estimated in this study depends on the physical properties of envelope leakage, such as the infiltration flow coefficient (C_f) and the pressure exponent (n) because AER_{RC} is driven by infiltration through the leakage. When considering manufacturers' design changes, the two leakage properties could also change AER_{RC} substantially and would become more specific to the vehicle model rather than vehicle age. Although vehicle aging can result in additional leakage, it is also important to consider the design changes in the vehicle models.

3.4.3. Infiltration with Different Fan Setting and Driving Speed

As driving speed increases, the pressure field changes not only in the passenger cabin but also on the surface of the vehicle envelope. While an active OA ventilation system pressurizes the passenger cabin at dP_{mech}, a moving vehicle also experiences aerodynamic pressure changes on the vehicle surface (i.e., dP_{aero}). Under stationary conditions ($\nu_{driving} = 0$), dP_{mech} maintains the positive pressure of the passenger cabin. Under mobile conditions ($\nu_{driving} > 0$), dP_{mech} increases because passive ventilation allows an additional volume of air (i.e., Q_{psvOA} in Figure 3.1) into the passenger cabin as a linear function of driving speed (see Eq. (3.2) and (3.5)). Similarly, dP_{aero} increases exponentially with respect to driving speed, specific to the aerodynamic envelope design (e.g., vehicle type). While a vehicle is moving, dP_{mech} is often compensated by dP_{aero}, thereby allowing infiltration air-flow (i.e., Q_{inf}) into the passenger cabin. Because dP_{mech} and dP_{aero} occur independently, the pressure affecting infiltration (dP_{inf}) can be determined by subtracting dP_{aero} from dP_{mech} in Eq. (3.4).

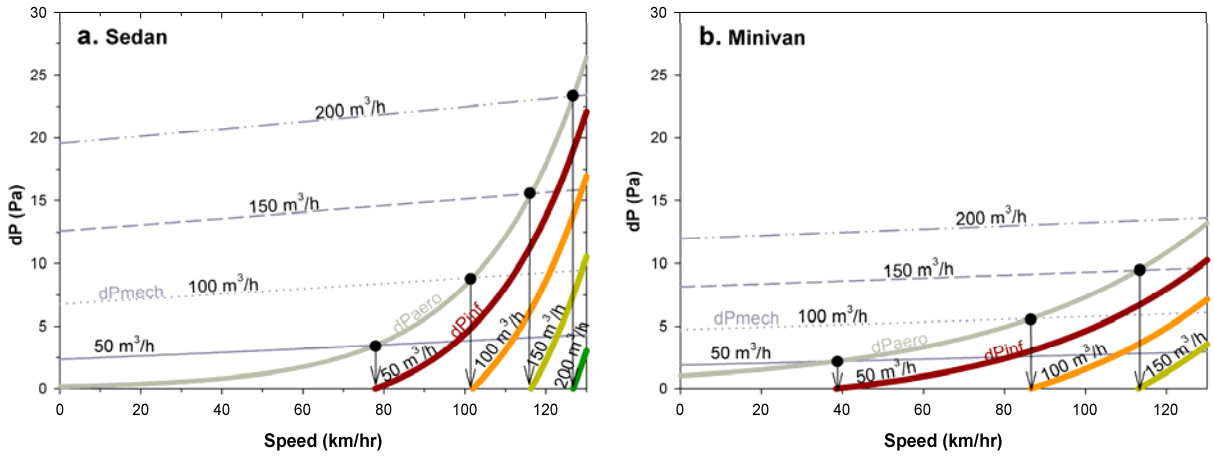


Figure 3.7 Differential pressure changes as a function of speed at given ventilation air-flow rates The differential pressure changes are simulated for (a) sedan and (b) minivan as a function of driving speed at a wide range of ventilation air flow rates: 50, 100, 150, and 200 m^3/h. The infiltration pressure differences (dP_{inf}, colored solid-lines) are determined by subtracting in-cabin pressures (dP_{cabin}), schemed gray lines) from the rear-trunk cabin pressure (dP_{rear}, gray solid-line). The black dots represent the critical speed at which infiltration starts occurring.

Figures 3.7a and 3.7b present the OA-mode simulation results of dP_{inf} for a sedan and a minivan, respectively. The dP_{mech} maintains positive cabin pressure and prevents infiltration up to a certain driving speed, above which dP_{aero} overcomes dP_{mech}, resulting in infiltration (i.e., $dP_{inf} > 0$). In Figure 3.7a, when Q_{atvOA} = 50 m^3/h under stationary conditions, dP_{mech} is only at 2.5 Pa but increases to 6 Pa at 130 km/hr for the same Q_{atvOA}. In this case, the dP_{inf} started increasing from 78 km/h and exhibited a further increase up to 22 Pa at 130 km/h. Conversely, the higher ventilation air-flow rate of 200 m^3/h effectively prevents infiltration up to 126 km/h, suggesting that proper maintenance of cabin pressure can prevent the infiltration of on-road pollutants.

Similar to the sedan, Figure 3.7b provides the simulation results for the minivan but at a different magnitude. For the same Q_{atvOA}, dP_{mech} is much lower in the minivan than in the sedan because the minivan often has a larger leakage area than the sedan. Accordingly, the same Q_{atvOA} could not raise dP_{mech} sufficiently high to compensate for dP_{aero}. For example, at 50 m^3/h, the dP_{inf} begins to increase above the critical driving speed of 38 km/h, which is much lower than the 78 km/h found in the sedan. However, with the same air-flow rate of 200 m^3/h, the dP_{inf} does not become positive while the driving speed is less than 130 km/h because of the different aerodynamic characteristics (i.e., shapes) of the two vehicle types.

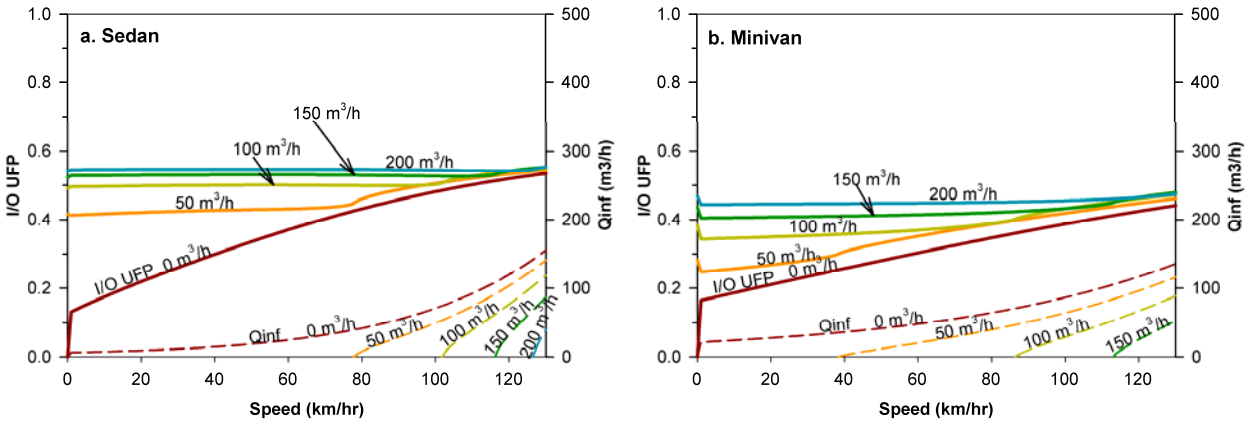


Figure 3.8 Ultrafine particle I/O ratio as a function of driving speed.
The changes in UFP I/O ratio (solid-lines) are compared to the infiltration air flow rates (Q_{inf}, dash-lines) with respect to the driving speed. The results are given for (a) a sedan and (b) a minivan at a typical range of ventilation air flow rates: 0, 50, 100, 150, and 200 m^3/h.

Further analysis examined the effects of the infiltration air-flow rate (Q_{inf}) on the I/O

ratio of UFPs (UFP I/O). Figure 3.8 provides UFP I/O and Q_{inf} as a function of driving speed in the sedan (Figure 3.8a) and minivan (Figure 3.8b). Overall, Q_{inf} increases at increasing driving speeds, but the critical driving speeds for infiltration and the magnitude of Q_{inf} are different for the sedan and minivan. The critical driving speed is lower in the minivan than the sedan, but more infiltration (i.e., greater Q_{inf}) occurs at the lower driving speed range in the minivan than in the sedan. However, at higher driving speeds, Q_{inf} is generally higher for the sedan than for the minivan.

The infiltrated particles also substantially increased the UFP I/O above a critical driving speed. In Figure 3.8a, at an air flow rate of 50 m^3/h, UFP I/O begins to increase from 0.41 to 0.45 due to active OA ventilation (Q_{atvOA}) and passive OA ventilation (Q_{psvOA}) when driving speed increased from 0 to 78 km/h. Above the critical driving speed of 78 km/h, infiltration (Q_{inf}) begins to increase UFP I/O further up to 0.55 at 130 m^3/h. UFP I/O simulation at Q_{atvOA} = 0 m^3/h exhibits the most significant I/O changes only by the effects of passive OA ventilation and infiltration. The use of higher fan settings minimizes the change in UFP I/O, suggesting that high in-cabin pressurization can reduce the UFP I/O fluctuation that arises from passive ventilation and infiltration. However, the increase in a supplied mechanical air-flow rate (i.e., Q_{atvOA}) stabilizes the UFP I/O at higher magnitude overall.

In summary, infiltration and passive ventilation substantially changes UFP I/O ratios.

The UFP I/O increases most significantly when $Q_{atvOA} = 0$ due to passive ventilation and more importantly infiltration. Although UFP I/O generally increases as a function of driving speed but its changes in magnitude is a complex function of Q_{atvOA}, Q_{psvOA}, and Q_{inf}. In addition, Q_{inf} occurs when dP_{mech} is less than dP_{aero}. Therefore, infiltration starts occurring above a certain critical driving speed, which can be determined by the two competing pressures discussed previously (see Eq (4) and Figure 3.8). A high fan setting reduced the fluctuation in UFP I/O but increased the overall I/O ratio. To investigate individual UFP gain/loss mechanisms, the following parametric sensitivity analysis further evaluated the proportional effects of (1) active OA ventilation, (2) passive OA ventilation, (3) RC filtration, (4) infiltration, and (5) surface deposition.

3.4.4. Fractional Impact by Different Mechanisms

Depending on the ventilation conditions (i.e., OA/RC mode and fan setting), the relative importance of each mechanism can change as speed increases. To elucidate the effects of each of the five mechanisms, this study conducted parametric evaluations on the five mechanisms using the concept of fractional impact (FI) in the following equations:

$$I_{total} = \underbrace{(1-\eta)\cdot\frac{Q_{atvOA}}{V_{cabin}}}_{Active\,OA\,Ventilation} + \underbrace{(1-\eta)\cdot\frac{Q_{psvOA}}{V_{cabin}}}_{Passive\,OA\,Ventilation} + \underbrace{\eta\cdot\frac{Q_{atvRC}}{V_{cabin}}}_{RC\,Filtration} + \underbrace{\alpha\cdot\frac{Q_{\inf}}{V_{cabin}}}_{Infiltration} + \underbrace{\beta}_{Deposition} \tag{3.7}$$

$$FI_i = \frac{I_i}{I_{total}} \tag{3.8}$$

where I_{total} is the sum of all five UFP gain/loss rates, I_i is a specific UFP gain/loss rate by mechanism i, and i can be (1) active OA ventilation, (2) passive OA ventilation, (3) RC filtration, (4) infiltration, or (5) surface deposition. FI_i is the fractional impact of a specific mechanism, i. Note that (3) and (5) are in-cabin UFP removal mechanisms, whereas (1), (2), and (4) are in-cabin UFP gain mechanisms.

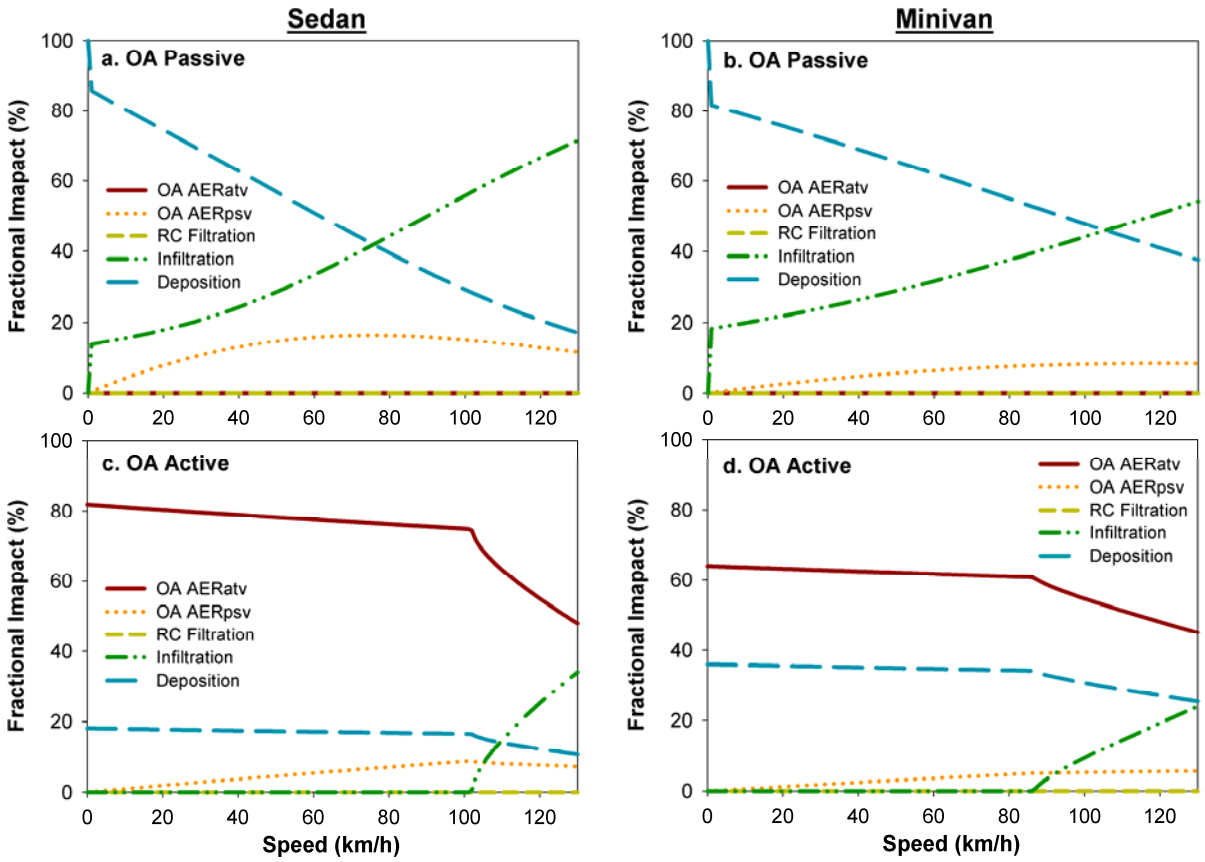


Figure 3.9 Changes of fractional impacts of in-cabin particle gain/loss mechanisms in outdoor air mode as a function of driving speed.

Under OA mode, the fractional impacts of different in-cabin particle gain/loss terms (OA AER_{atv}, OA AER_{psv}, RC Filtration, Infiltration, and Deposition) are compared for (a, c) a sedan and (b, d) a minivan as a function of driving speed. The top two panels (a, b) illustrate the results of OA passive ventilation (i.e., with no fan operation/open damper), and the bottom two panels (c, d) illustrate the OA active ventilation (i.e., with fan operation/open damper) simulation results using the same ventilation air-flow (100 m^3/h) for the sedan and minivan, respectively.

Figure 3.9 presents the fractional impact simulation results in OA mode for the sedan and minivan. Under passive ventilation, the surface deposition is the most significant factor when the vehicle is in stationary mode, but its fractional impact is reduced from 87% to 20% for

the sedan in Figure 3.9a. The infiltration process becomes more important as driving speed increases. At 80 km/h, the fractional impact of infiltration becomes greater than the fractional impact of surface deposition. The fractional impact of passive ventilation remained less than 20% across the typical driving speed less than 130 km/h. Figure 3.9b shows a similar pattern observed in the minivan under the same ventilation conditions. However, the infiltration becomes more important than deposition as more substantial infiltration occurs at a higher driving speed of approximately 100 km/h. The fractional impact by passive ventilation also remained under 10%, suggesting that UFP I/O can be lower at low driving speeds because surface deposition loss is dominant under those circumstances. However, UFP I/O can be higher at high driving speeds and is significantly affected by infiltration and passive ventilation.

Under active ventilation in Figures 3.9c and d, active OA ventilation governs the particle gain/loss mechanism (FI > 50%) throughout the studied driving speed range. With a minimal fractional impact by passive ventilation (FI < 10%), the fractional impact of infiltration begins to increase above the critical driving speed, which is 100 km/h for the sedan and 85 km/h for the minivan. The fractional impact of surface deposition is not as high as observed in OA passive scenarios in Figures 3.9a and b; however, surface deposition still represents 20% and 35% of the total UFP gain/loss rate for the sedan and minivan, respectively. The proportion of surface deposition is considered relatively high in comparison with active OA ventilation and the others,

so the particle loss by surface deposition could be significant. Particle loss through surface deposition could be more important under RC mode, which only allows for air exchange via infiltration.

Figure 3.10 provides the fractional impact modeling results for RC mode. Because under the RC mode, air exchange only occurs by infiltration, the RC-Q_{off} conditions in Figures 3.10a and b are dominantly driven by infiltration processes. Without the effects of passive ventilation, the fractional impact of deposition is slightly higher than the fractional impact of deposition observed in OA mode (see Figures 3.9a, b), which is the reason why infiltration was more easily observed at high driving speeds under RC-Q_{off} mode.

When the fan is operating under RC mode (i.e., RC active in Figures 10c and d), filtration is a continuous particle removal mechanism, which dominantly controls the in-cabin UFPs. RC filtration was more prevalent in the sedan than in the minivan under the same mechanical ventilation air-flow rate of 100 m^3/h because the cabin volume (V_{cabin}) is smaller for the sedan than for the minivan. More importantly, the fractional impact by deposition remains higher than RC filtration in the minivan, whereas the infiltration process remains comparable for both vehicle types. Therefore, the effects of the five different particle gain/loss mechanisms can be dynamically different as a function of driving speed. Different ventilation modes (OA/RC mode) provide completely different profiles of relative importance for each mechanism.

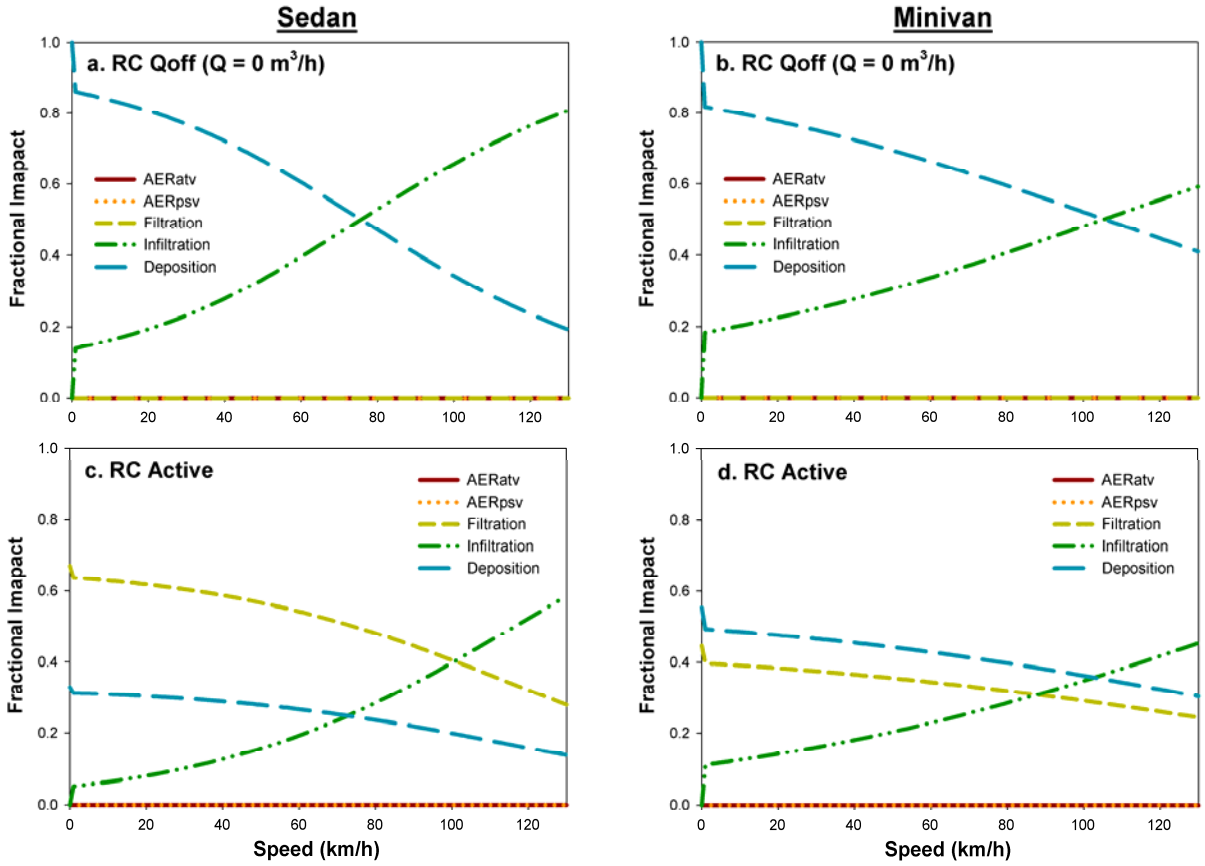


Figure 3.10 Changes of fractional impacts of in-cabin particle gain/loss mechanisms in recirculation mode as a function of driving speed

Under RC mode, the fractional impacts of different in-cabin particle gain/loss terms (OA AER_{atv}, OA AER_{psv}, RC Filtration, Infiltration, and Deposition) are compared for (a, c) a sedan and (b, d) a minivan as a function of driving speed. The top two panels (a, b) illustrate the results of RC ventilation with no fan operation/close damper, and the bottom two panels (c, d) illustrate the RC active ventilation (i.e., with fan operation/close damper) simulation results using the same ventilation air-flow (100 m^3/h) for the sedan and minivan, respectively.

Consequently, the work in this chapter evaluated the effects of infiltration and passive ventilation on in-cabin UFP dynamics. The proposed model simulates in-cabin UFP concentrations at different driving speeds and ventilation conditions (i.e., selection of OA/RC mode and blower fan setting) in time. The model was validated with the literature data and experimental measurements from 10 vehicle models. Although the assumption of no particle phase change tends to increase model bias at high in-cabin UFP concentrations, the model bias remained less than 16% for UFPs and near zero for CO_2 for a typical range of in-cabin concentrations.

This chapter discussed five in-cabin UFP gain/loss mechanisms: active OA ventilation, passive OA ventilation, RC filtration, infiltration, and surface deposition. Aerodynamic pressure changes on a moving vehicle surface substantially affected infiltration and passive OA ventilation. Similar to previous findings, a linear function was observed between air exchange rate due to passive ventilation and driving speed. Infiltration increases exponentially and results from the competition between the in-cabin pressurization by mechanical ventilation and the aerodynamic pressure changes on vehicle surface. Therefore, infiltration becomes more important at higher driving speed and only occurs above a certain driving speed, which depends on the aerodynamic design of the vehicle and the fan setting.

The fractional impact of the five in-cabin UFP gain/loss mechanisms also changes

dynamically as a function of driving speed. This study observed intriguingly high fractional impact by surface deposition overall. However, the fractional impact of surface deposition decreased at increasing driving speed, which substantiated other mechanisms such as infiltration and passive ventilation. The fractional impact of passive ventilation is generally less than 20% under OA mode and does not occur under RC mode. Although infiltration can occur under any circumstances, the effects of infiltration on UFP I/O can be reduced by cabin pressurization using active mechanical ventilation in OA mode. Even with a high fractional impact of surface deposition, the infiltration process often becomes greater relative to the driving speed, thereby leading to a net positive gain of in-cabin UFPs at high driving speeds.

References

(1) Penttinen, P.; Timonen, K. L.; Tiittanen, P.; Mirme, A.; Ruuskanen, J.; Pekkanen, J. Ultrafine particles in urban air and respiratory health among adult asthmatics. *European Respiratory Journal* **2001**, *17*, 428-435.

(2) Peters, A.; Wichmann, H. E.; Tuch, T.; Heinrich, J.; Heyder, J. Respiratory effects are associated with the number of ultrafine particles. *American Journal of Respiratory and Critical Care Medicine* **1997**, *155*, 1376-1383.

(3) von Klot, S.; Wolke, G.; Tuch, T.; Heinrich, J.; Dockery, D. W.; Schwartz, J.; Kreyling, W. G.; Wichmann, H. E.; Peters, A. Increased asthma medication use in association with ambient fine and ultrafine particles. *European Respiratory Journal* **2002**, *20*, 691-702.

(4) Andersen, Z. J.; Olsen, T. S.; Andersen, K. K.; Loft, S.; Ketzel, M.; Raaschou-Nielsen, O. Association between short-term exposure to ultrafine particles and hospital admissions for stroke in copenhagen, denmark. *European Heart Journal* **2010**, *31*, 2034-2040.

(5) Stolzel, M.; Breitner, S.; Cyrys, J.; Pitz, M.; Wolke, G.; Kreyling, W.; Heinrich, J.; Wichmann, H. E.; Peters, A. Daily mortality and particulate matter in different size classes in erfurt, germany. *Journal of Exposure Science and Environmental Epidemiology* **2007**, *17*, 458-467.

(6) Shi, Z. B.; Shao, L. Y.; Jones, T. P.; Whittaker, A. G.; Lu, S. L.; Berube, K. A.; He, T.; Richards, R. J. Characterization of airborne individual particles collected in an urban area, a satellite city and a clean air area in beijing, 2001. *Atmospheric Environment* **2003**, *37*, 4097-4108.

(7) Morawska, L.; Ristovski, Z.; Jayaratne, E. R.; Keogh, D. U.; Ling, X. Ambient nano and ultrafine particles from motor vehicle emissions: Characteristics, ambient processing and implications on human exposure. *Atmospheric Environment* **2008**, *42*, 8113-8138.

(8) Knibbs, L. D.; de Dear, R. J.; Atkinson, S. E. Field study of air change and flow rate in six automobiles. *Indoor Air* **2009**, *19*, 303-313.

(9) Saber, E. M.; Bazargan, M. Dynamic behavior modeling of cigarette smoke particles inside the car cabin with different ventilation scenarios. *International Journal of Environmental Science and Technology* **2011**, *8*, 747-764.

(10) Xu, B.; Liu, S. S.; Liu, J. J.; Zhu, Y. F. Effects of vehicle cabin filter efficiency on ultrafine particle concentration ratios measured in-cabin and on-roadway. *Aerosol Science and Technology* **2011**, *45*, 234-243.

(11) Qi, C.; Stanley, N.; Pui, D. Y. H.; Kuehn, T. H. Laboratory and on-road evaluations of cabin air filters using number and surface area concentration monitors. *Environmental*

Science & Technology **2008**, *42*, 4128-4132.

(12) Chan, L. Y.; Lau, W. L.; Zou, S. C.; Cao, Z. X.; Lai, S. C. Exposure level of carbon monoxide and respirable suspended particulate in public transportation modes while commuting in urban, area of guangzhou, china. *Atmospheric Environment* **2002**, *36*, 5831-5840.

(13) Esber, L. A.; El-Fadel, M.; Nuwayhid, I.; Saliba, N. The effect of different ventilation modes on in-vehicle carbon monoxide exposure. *Atmospheric Environment* **2007**, *41*, 3644-3657.

(14) Klepeis, N. E.; Nelson, W. C.; Ott, W. R.; Robinson, J. P.; Tsang, A. M.; Switzer, P.; Behar, J. V.; Hern, S. C.; Engelmann, W. H. The national human activity pattern survey (nhaps): A resource for assessing exposure to environmental pollutants. *Journal of Exposure Analysis and Environmental Epidemiology* **2001**, *11*, 231-252.

(15) Fruin, S.; Westerdahl, D.; Sax, T.; Sioutas, C.; Fine, P. M. Measurements and predictors of on-road ultrafine particle concentrations and associated pollutants in los angeles. *Atmospheric Environment* **2008**, *42*, 207-219.

(16) Zhu, Y. F.; Eiguren-Fernandez, A.; Hinds, W. C.; Miguel, A. H. In-cabin commuter exposure to ultrafine particles on los angeles freeways. *Environmental Science & Technology* **2007**, *41*, 2138-2145.

(17) Pui, D. Y. H.; Qi, C.; Stanley, N.; Oberdorster, G.; Maynard, A. Recirculating air filtration significantly reduces exposure to airborne nanoparticles. *Environmental Health Perspectives* **2008**, *116*, 863-866.

(18) Hudda, N.; Kostenidou, E.; Sioutas, C.; Delfino, R. J.; Fruin, S. A. Vehicle and driving characteristics that influence in-cabin particle number concentrations. *Environmental Science & Technology* **2011**, *45*, 8691-8697.

(19) Lee, E. S.; Stenstrom, M. K.; Zhu, Y. F. Ultrafine particle infiltration into passenger vehicles: Effects of driving speed and ventilation condition. *Environmental Science & Technology* (in review)

(20) Baker, P. H.; Sharples, S.; Ward, I. C. Air-flow through cracks. *Building and Environment* **1987**, *22*, 293-304.

(21) Xu, B.; Liu, S.; Zhu, Y. Ultrafine particle penetration through idealized vehicle cracks. *Journal of Aerosol Science* **2010**, *41*, 859-868.

(22) Xu, B.; Zhu, Y. Quantitative analysis of the parameters affecting in-cabin to on-roadway (i/o) ultrafine particle concentration ratios. *Aerosol Science and Technology* **2009**, *43*, 400-410.

(23) Fletcher, B.; Saunders, C. J. Air change rates in stationary and moving motor-vehicles. *Journal of Hazardous Materials* **1994**, *38*, 243-256.

(24) Knibbs, L. D.; de Dear, R. J.; Morawska, L. Effect of cabin ventilation rate on ultrafine particle exposure inside automobiles. *Environmental Science & Technology* **2010**, *44*, 3546-3551.

(25) Ott, W.; Klepeis, N.; Switzer, P. Air change rates of motor vehicles and in-vehicle pollutant concentrations from secondhand smoke. *Journal of Exposure Science and Environmental Epidemiology* **2008**, *18*, 312-325.

(26) Gong, L.; Xu, B.; Zhu, Y. Ultrafine particles deposition inside passenger vehicles. *Aerosol Science and Technology* **2009**, *43*, 544-553.

(27) Joodatnia, P.; Kumar, P.; Robins, A. Fast response sequential measurements and modelling of nanoparticles inside and outside a car cabin. *Atmospheric Environment* **2013**, *71*, 364-375.

(28) Song, K. S.; Kang, S. O.; Jun, S. O.; Park, H. I.; Kee, J. D.; Kim, K. H.; Lee, D. H. Aerodynamic design optimization of rear body shapes of a sedan for drag reduction. *International Journal of Automotive Technology* **2012**, *13*, 905-914.

(29) ASHRAE *Ashrae handbook: 2005 fundamentals*; American Society of Heating, Refrigerating, and Air-Conditioning Engineers: Atlanta, GA, 2005.

(30) ASTM, *E779-10 standard test method for determining air leakage rate by fan pressurization*; ASTM International: West Conshohocken, PA, 2010.

(31) ASTM, *E1827-11 standard test methods for determining airtightness of buildings using an orifice blower door*; ASTM International: West Conshohocken, PA, 2011.

(32) Engelmann, R. J.; Pendergrass, W. R.; White, J. R.; Hall, M. E. The effectiveness of stationary automobiles as shelters in accidental releases of toxic materials. *Atmospheric Environment Part a-General Topics* **1992**, *26*, 3119-3125.

(33) Park, J. H.; Spengler, J. D.; Yoon, D. W.; Dumyahn, T.; Lee, K.; Ozkaynak, H. Measurement of air exchange rate of stationary vehicles and estimation of in-vehicle exposure. *Journal of Exposure Analysis and Environmental Epidemiology* **1998**, *8*, 65-78.

(34) Rodes, C.; Sheldon, L.; Whitaker, D.; Clayton, A.; Fitzgerald, K.; Flanagan, J.; DiGenova, F.; Hering, S.; Frazier, C. "Measuring concentrations of selected air pollutants inside california vehicles, report prepared for california epa," California Air Resources Board, 1998.

(35) Fruin, S. A.; Hudda, N.; Sioutas, C.; Defino, R. J. Predictive model for vehicle air exchange rates based on a large, representative sample. *Environmental Science & Technology* **2011**, *45*, 3569-3575.

4. APPLICATION OF HIGH EFFICIENCY AIR FILTER

4.1. Abstract

Modern passenger vehicles are commonly equipped with cabin air filters, but the filtration efficiency is only 40-60% for ultrafine particles (UFPs). Although setting the vehicle ventilation system to recirculation (RC) mode can reduce in-cabin UFPs by 80-95%, carbon dioxide (CO_2) from the exhaled breath of passengers can quickly accumulate inside the cabin. To prevent CO_2 accumulation, the vehicle must be operated under outdoor air (OA) mode to allow for sufficient air exchange. To overcome this dilemma, this study investigated in-cabin UFP removal under OA mode using high-efficiency particulate air (HEPA) filters. Concentrations of UFP and other air pollutants were simultaneously monitored inside and outside of 12 different vehicles under three different driving conditions: stationary, local roadway, and freeway. Under each of the experimental conditions, data were collected with no filter, in-use original equipment manufacturer (OEM) filter, and two types of HEPA filters. The HEPA filters were found to reduce the in-cabin UFP concentration by 93% on average under OA-mode field conditions, representing a much higher efficiency than the OEM filters used currently (41-65% on average). The application of a HEPA filter in OA mode also enabled the in-cabin environment to be more independent of the changes in the driving speed and the fluctuations in the UFP concentrations on different roadways. Throughout the measurements, the in-cabin CO_2 concentration remained in the range of 635-924 ppm, representing a significant reduction from the typical in-cabin CO_2 concentration range of 2,500-4,000 ppm in RC mode.

4.2. Introduction

Several epidemiological and toxicological studies have demonstrated that the adverse health effects of ultrafine particles (UFPs, diameter ≤ 100 nm) are not limited to pulmonary diseases, as UFPs could also damage other organs through inter-organ translocation.[1-8] The cardiovascular system is considered a target to which UFPs can translocate from the lungs, as demonstrated in animal models[1-3,6,7] and human subjects.[4,5] Once inhaled, UFPs can also penetrate the epithelium, enter the circulatory system, and be deposited into other organs, including the brain.[8] The small size and large surface area of UFPs also allow them to penetrate cell walls and localize in mitochondria.[9] Due to the numerous redox-active chemicals present in motor-vehicle-emitted UFPs, systemic inflammation can also occur.[10,11]

In an urban environment, vehicle emissions usually constitute the most significant source of primary UFPs.[12,13] The on-road UFP concentration typically ranges from 100,000 to 500,000 particles/cm^3,[14-16] which is an order of magnitude higher than the ambient background typically on the order of 5,000-50,000 particles/cm^3. Accordingly, despite the short average commuting time (1.3 h/day),[17] in-cabin exposure alone accounts for up to 45-50% of the total daily exposure to UFPs.[15,18]

Modern vehicles are commonly equipped with cabin air filters;[19] however, the overall passenger protection against UFPs is limited to 40-60%.[20] The level of protection also varies with respect to the vehicle type and age in addition to the ventilation settings.[15] Although operating the automotive ventilation system under recirculation (RC) on mode can achieve a protection of ~85% using the manufacturer-installed cabin air filters,[15,21] this setting also causes passenger-exhaled CO_2 to accumulate rapidly in the vehicle cabin. Therefore, the current automotive ventilation systems and cabin air filters cannot control both UFPs and CO_2

simultaneously.

This study aimed to achieve a simultaneous control of both UFPs and CO_2 by applying high-efficiency particulate air (HEPA) filtration in outdoor air (OA) mode. Field measurements were conducted in 12 different vehicles of different types from several automobile manufacturers. In-cabin UFP exposure reductions were compared under three driving conditions (i.e., stationary, local roadway, and freeway) with four different filter types: no filter, in-use original equipment manufacturer (OEM), and two types of HEPA filters.

4.3. Methods

4.3.1. Automotive Cabin HEPA Filters

Two types of automotive-cabin HEPA filters (noted here as HEPA A and HEPA B) were developed in collaboration with an industrial partner. The two HEPA filters were similar to OEM cabin air filters in terms of their structure, i.e., the pleated panel type, but differed in the filtration media used. Whereas OEM filters are typically composed of a single layer of glass fibers, the developed HEPA filters were manufactured with a double layer, with synthetic fibers on the upstream side and glass fibers on the downstream side. The application of synthetic fibers with different physicochemical properties (e.g., diameter, material, and density) on the upstream layer allows the HEPA filters to achieve significantly higher filtration efficiency than OEM filters. Considering the additional pressure drop upon retrofitting with HEPA filters, the HEPA A filters were designed to maintain a pressure drop equivalent to the OEM filters by increasing the intrinsic surface area with 1-3 μm fibers. Unlike the HEPA A filters, the HEPA B filters were designed to maximize the filtration efficiency using 400-800 nm fibers. Figure 4.1 and 4.2 show

the scanning electron microscope images of HEPA A and B filters, respectively. Because there is no filtration efficiency rating standard currently available for automotive cabin filters, the HEPA filters were graded using the minimum efficiency reporting value (MERV) standard developed by the American Society of Heating, Refrigerating and Air-Conditioning Engineers (ASHRAE) for building heating, ventilating, and air-conditioning (HVAC) systems. A MERV rating of 15 and 16 was achieved for the HEPA A and B filters, as shown in Figures 4.3 and 4.4, respectively.



Figure 4.1 Scanning electron microscope (SEM) image of HEPA A filter
Diesel soot particles are attached on the synthetic fiber (diameter 1-3 μm) of HEPA A filter media.

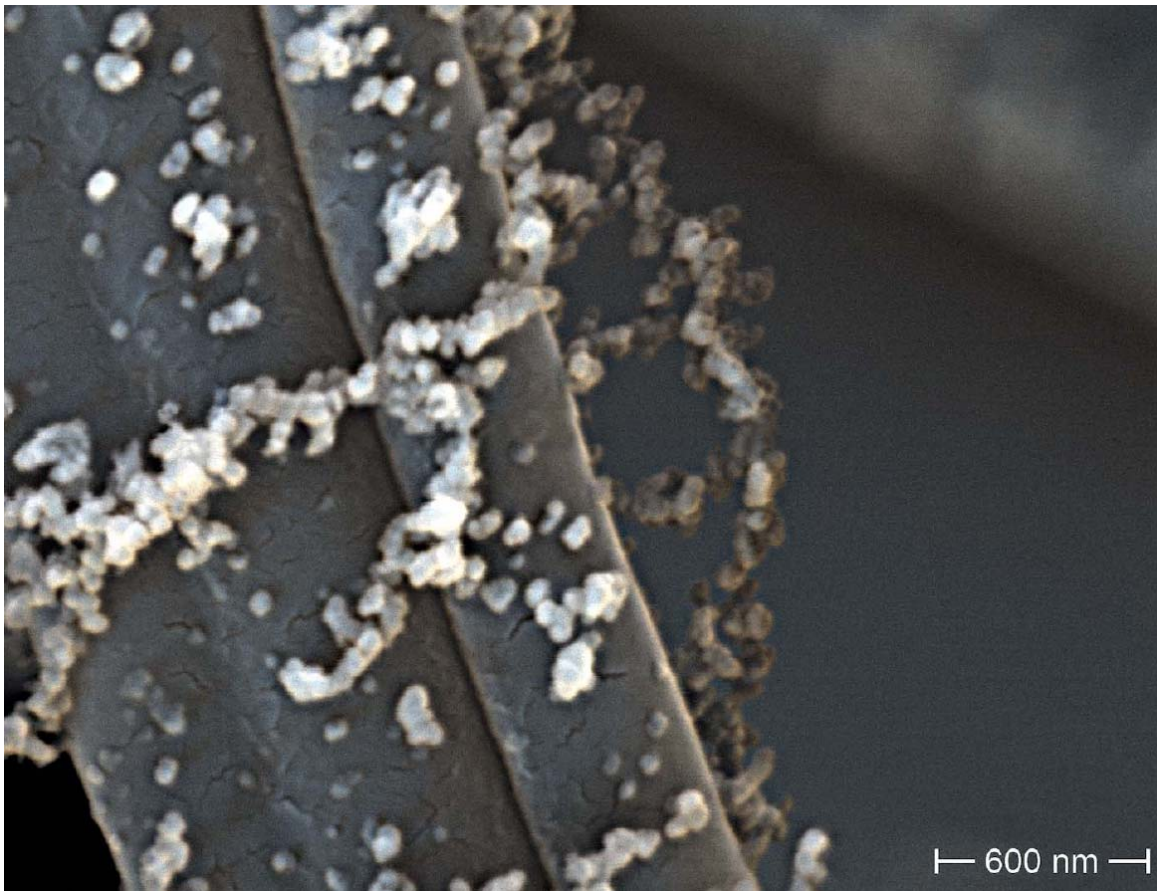


Figure 4.2 Scanning electron microscope (SEM) image of HEPA B filter
Diesel soot particles are attached on the synthetic fiber (diameter 400-800 nm) of HEPA B filter media.

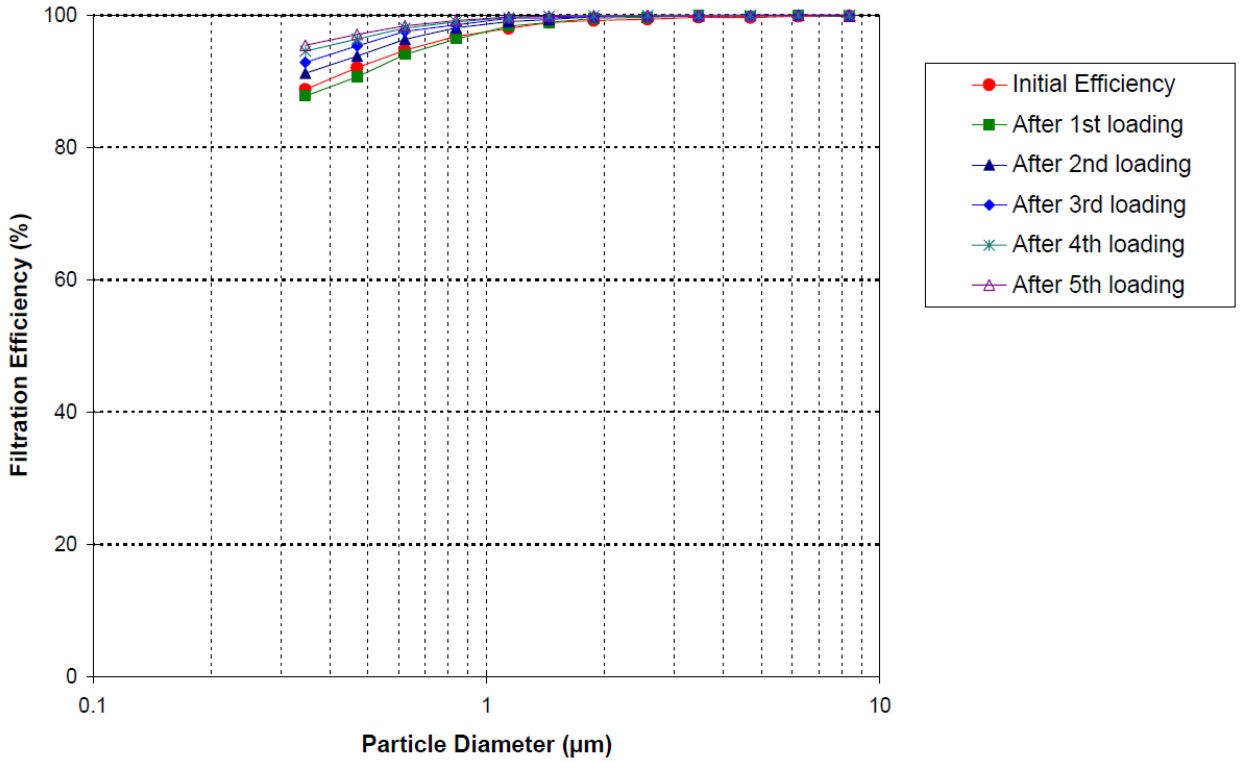


Figure 4.3 Lab testing results of the particle size-specific filtration efficiency of HEPA A filter The filtration efficiency is shown with respect to particle diameter. The tests were conducted with dust particles at constant air flow rate and face velocity of 3344 m3/h and 2.5 m/s, respectively.

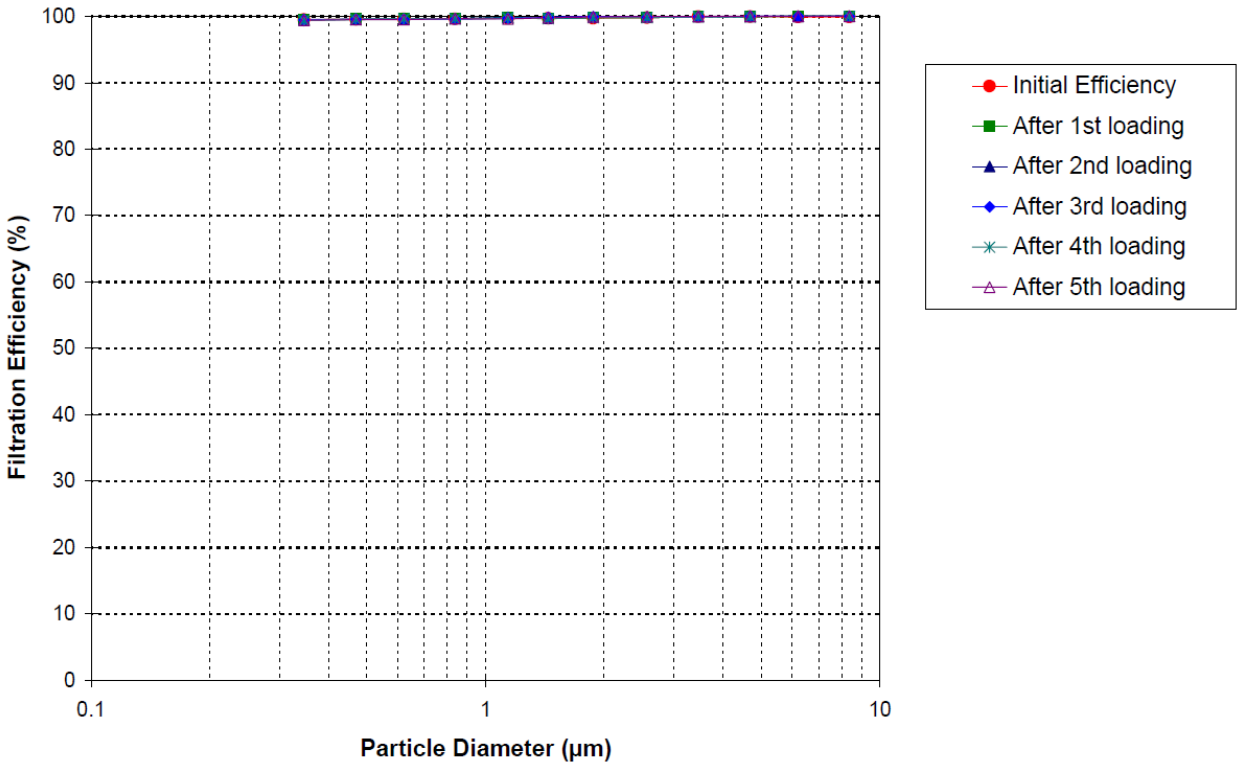


Figure 4.4 Lab testing results of the particle size-specific filtration efficiency of HEPA B filter The filtration efficiency is shown with respect to particle diameter. The tests were conducted with dust particles at constant air flow rate and face velocity of 3344 m^3/h and 2.5 m/s, respectively.

4.3.2. Test Vehicle Selections

Twelve passenger vehicles of different models and types and from different manufacturers and countries of origin were selected to investigate the in-cabin exposure reductions resulting from the application of the HEPA filters. As listed in Table 4.1, the vehicle selection included eight small-cabin vehicle models (i.e., six sedans and two hatchbacks) and four large-cabin vehicles (i.e., two SUVs and two minivans) that are among popular vehicle models. The cabin volume size ranged from 2.94 to 7.03 m^3.[22] To minimize the potential variability that can result from vehicle aging, the test vehicles chosen were not older than three years. The accumulated mileage of the vehicles ranged from 1,339 to 74,174 km. The cabin air filter housing was most commonly found behind the glove box, but a few vehicle models also had cabin air filters under the dashboard or hood, as noted in Table 4.1. Except for the 2012 Chevrolet Impala, all test models were equipped with an in-use OEM filter.

Table 4.1 A summary of the test vehicle models and specifications

Vehicle Type	Maker	Model	Year	Mileage (km)	Cabin Filter Locations	Cabin Volume (m^3)
Hatchback	Ford	Focus	2012	51,347	Glove Box	2.94
	Toyota	Prius	2012	9,102	Glove Box	3.88
Sedan	Chevrolet	Impala	2012	1,339	Glove Box	4.01
	Honda	Accord	2011	51,194	Glove Box	3.83
	Hyundai	Sonata	2013	21,712	Glove Box	3.41
	Nissan	Sentra	2012	30,398	Under Dash	3.50
	Toyota	Camry	2012	1,931	Glove Box	3.78
	Volkswagen	Jetta	2012	14,917	Under Hood	3.55
SUV	Ford	Explorer	2013	16,510	Glove Box	4.89
	Toyota	Highlander	2012	10,611	Glove Box	4.43
Minivan	Honda	Odyssey	2010	38,622	Glove Box	7.03
	Toyota	Sienna	2011	74,174	Glove Box	5.76

4.3.3. Field Measurements

During the field measurements, the in-cabin and on-road concentrations were concurrently monitored for UFPs, $PM_{2.5}$, black carbon (BC), and CO_2 to assess the in-cabin passenger exposure reductions. Two sets of instruments were deployed for the concurrent measurements of the in-cabin and on-road air: one set monitored at the center of the passenger cabin and the other outside. Two condensation particle counters (CPCs) were deployed to measure the UFP concentrations for the in-cabin (Model 3785, TSI Inc., St. Paul, MN) and on-road (Model 3786, TSI Inc., St. Paul, MN) conditions. Similarly, two Dusttraks (Model 8520, TSI Inc., St. Paul, MN) and two Qtraks (Model 8554, TSI Inc., St. Paul, MN) simultaneously logged changes in the in-cabin and on-road concentrations of $PM_{2.5}$ and CO_2. The BC concentrations inside and outside of the cabin were also recorded with two aethalometers (Models AE-22 and AE-42, Magee Scientific Co., Berkeley, CA). All of the instruments were calibrated prior to their deployment for field sampling and set to a logging interval of 1 s, except for the aethalometers, which were set to their minimum logging interval of 1 min. In addition, the particle size distribution data were collected using two sets of scanning mobility particle sizers (SMPSs, Model 3080 with Model 3085, TSI Inc., St. Paul, MN). The two sets of SMPSs were configured to sample the in-cabin and on-road ambient atmospheres in conjunction with the TSI 3785 and TSI 3786 CPCs used for sampling the in-cabin and on-road UFP conditions, respectively. The in-cabin and on-road particle size distribution in the size range of 7.37-289 nm were concurrently collected. The applied scanning and retrace times were 100 and 20 s, respectively.

Under the medium fan setting in OA mode, data were collected for each of the vehicle under three different driving conditions: stationary, local roadway, and freeway conditions. Stationary sampling was conducted in an underground parking lot. Local-roadway sampling was repeatedly conducted on the 2.4-mile sector of Westwood Blvd between Wilshire Blvd and National Blvd in Los Angeles, CA. The freeway testing route included a 22-mile segment of I-405 between the I-10 and I-710 freeways. Four different types of filters (i.e., no filter, in-use OEM, HEPA A, and HEPA B) were tested under each of the three different driving conditions for at least 15 min during each filter/driving condition combination. The collected data included 144 different experimental conditions and provided more than 130,000 pairs of one-second data concurrently acquired for both the in-cabin and on-road concentrations to assess the in-cabin passenger exposure reductions.

4.4. Results and Discussion

4.4.1. Particle Size Distributions under Different Conditions

Figure 4.5 shows an overview of the in-cabin and on-road ambient particle size distributions averaged across each sampling period using the same filter and plotted for the different driving conditions, namely, (a) stationary, (b) local, and (c) freeway. The solid lines represent the particle size distribution data collected for the on-road air, whereas the dot-and-dash lines represent the in-cabin particle size distributions with no filter, an in-use OEM filter, and HEPA B filters.

The three driving conditions were distinctively different in their on-road particle size distributions. For the stationary conditions, the ambient data exhibited size distributions with a

mode diameter of ~80 nm, which is significantly larger than the ~30 nm observed for the freeway conditions. Due to the abundant presence of nucleation mode particles, the freeway conditions exhibited a typical bi-modal size distribution (Figure 4.5c). In comparison, the data collected for the local roadway conditions exhibited a mixture of the stationary and freeway particle size distributions. The particle size distribution data demonstrated distinctive triple modes for the local roadway conditions (Figure 4.5b). Throughout the local roadway sampling, each measured particle size distribution exhibited dynamic changes in the mode diameter and accordingly resulted in the presence of multiple mode diameters in the average particle size distribution plotted in Figure 4.5b. The multiple modes for the local roadway conditions reflect the complexity of the traffic conditions, which are considerably affected by local factors, including vehicle emissions and traffic density near the test vehicle at the time.

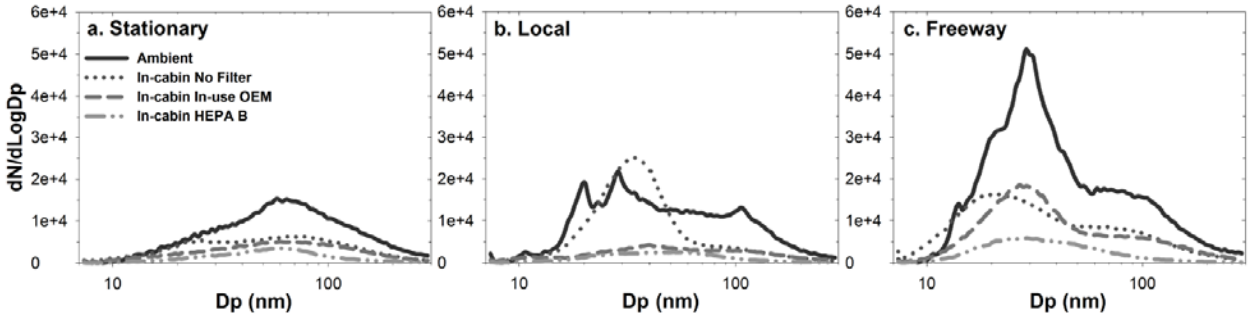


Figure 4.5 Particle size distributions for the on-road and in-cabin environments with different filter types
Averaged particle size distribution data are presented for the on-road (ambient) and in-cabin with different filters (i.e., no filter, in-use OEM, and HEPA B) in (a) stationary, (b) local roadway, and (c) freeway conditions. The size distribution data for HEPA A was not included for clarity.

The in-cabin reductions were commonly found across a wide range of particle sizes for all driving conditions. In comparison with the ambient concentrations for the three driving conditions, the plotted data in Figure 4.5 also demonstrate the significant reductions in the in-

cabin particle concentrations across the measured particle size range. Even with no filters, the reduction was significant due to particle diffusion loss to the ventilation systems. Installation of in-use OEM filters offered additional particle removal for all conditions, but the reduction remained small in magnitude (Figures 4.5). Upon retrofitting with HEPA B filters, the in-cabin particle concentration was further decreased especially for particles in the nucleation mode as in the case of the freeway driving shown in Figure 4.5c.

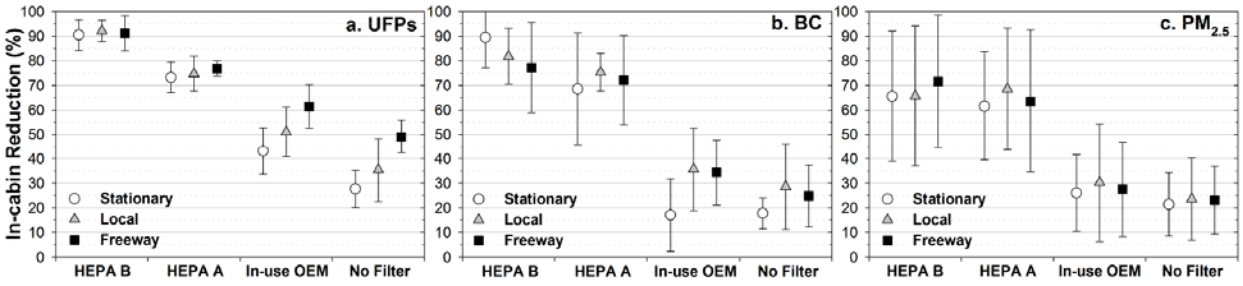


Figure 4.6 In-cabin particle concentration reductions with different filters and driving conditions In-cabin reduction of (a) UFPs, (b) BC, and (c) $PM_{2.5}$ in application of different filters and driving conditions: stationary (white), local roadway (gray), and freeway (black). The symbols and error bars present the means and standard deviations of the 1-minute average data from all 12 test vehicle models.

4.4.2. In-cabin Reduction for UFPs, Black Carbon, and $PM_{2.5}$

Based on the field measurement data, Figure 4.6 provides the in-cabin particle concentration reductions relative to the on-road ambient concentration. Under the scope of this study, the in-cabin pollutant reduction was estimated from the in-cabin/on-road (I/O) concentration ratio (i.e., in-cabin reduction = 1 - I/O). The plotted data points are the means of the 1 min averaged data in each of the 12 test vehicle models for (a) UFPs, (b) BC, and (c) $PM_{2.5,}$ which were measured under the different driving conditions and using the different filter types. The total number of observations for each plotted data point (i.e., one-minute mean) and each

error bar (i.e., standard deviation) was greater than 150 which were averaged from 9,000 one-second raw measurement data points.

As shown in Figure 4.6a, under stationary and realistic driving conditions, the use of the HEPA B filter achieved an average reduction of 93% for UFPs with minimal variability that originates from the characteristics of various vehicle models. In comparison, the no-filter scenario exhibited an average reduction of 20-55% and the in-use OEM filter had an average reduction to 35-70%. The application of the HEPA A and B filters enabled further reductions of 68-82% and 85-99%, respectively. In addition to the great in-cabin UFP reduction, the application of the HEPA filters also minimized the variability (i.e., error bars) in UFP concentration for the different vehicle models.

Figure 4.6 also illustrates the in-cabin UFP reductions achieved under each of the different driving conditions (i.e., stationary, local, and freeway). As shown in Figure 4.6a, the maximum UFP reduction occurred under the freeway driving conditions because particle diffusion loss is more effective for the nucleation mode particles abundantly present in the freeway environment. As discussed in Figure 4.5, the particle size distributions under the freeway conditions included a large portion of nucleation mode particles with a mode diameter near 30 nm. Because the freeway particle size distribution is skewed toward small diameters, the largest in-cabin UFP reduction resulted from the diffusion loss of the large population of small particles.

In contrast, because of the large number of larger particles (mode diameter = 80 nm) under the stationary driving conditions, the in-cabin reduction was smaller under the stationary conditions than under the local or freeway condition. Note that the field observations indicated that the overall in-cabin concentrations were greatest under the freeway conditions, followed by

the local and then the stationary conditions. Thus, the greater reduction observed in the freeway environment should not be misinterpreted as the in-cabin UFP concentration being lower for the freeway driving conditions compared to those for the local or stationary conditions. The size-specific in-cabin concentration reduction is discussed in more detail in Figure 4.8.

The in-cabin reductions were lower for BC and $PM_{2.5}$ than UFPs, and lower on freeway than on local roadway, as shown in Figures 4.6b and 4.6c. This is likely due to three important factors. First, BC and $PM_{2.5}$ were measured for their mass concentrations and the effects of diffusion loss on smaller particles have little impacts on the mass concentration reductions in BC and $PM_{2.5}$. Second, the mass concentrations of BC and $PM_{2.5}$ represent a wider range of particles with diameters up to 1 μm and 2.5 μm, respectively. Because the particle size that gives the minimum filtration efficiency usually occurs around 0.1-0.3 μm,[23] the filtration efficiency could be substantially lower for a significant mass fraction of BC and $PM_{2.5}$ which leads to a decrease of total in-cabin reduction. Finally, the smaller in-cabin reduction under the freeway conditions is in part because of the increase in the infiltrated portion of the on-road pollutants, which often occurs at higher driving speeds on freeways.[24] The infiltration effects were not noticeable for UFPs (in Figure 4.6a) because the diffusion loss during the infiltration process was also significant for the nucleation mode UFPs on the freeways. However, the infiltrated on-road BC and $PM_{2.5}$ can lead to a substantial decrease in the overall in-cabin mass concentration reduction in the freeway environment. Due to these three factors, the in-cabin reductions in BC and $PM_{2.5}$ were smaller than UFPs and smaller under the freeway driving conditions than under the local driving conditions.

In summary, the HEPA filters successfully reduced all three pollutants under the field conditions. The HEPA B filter reduced the in-cabin concentrations of UFPs, BC, and $PM_{2.5}$ by 93,

80, and 70%, respectively, compared to the on-road concentrations. The use of the HEPA B filter also greatly reduced the variability in the data from the different vehicle models and under the different driving conditions. Compared to the in-use OEM filters, the HEPA filters increased the removal of the three pollutants by a factor of two to three. Table 4.2 summarizes the measured UFPs, BC, and $PM_{2.5}$ concentrations in more detail.

Table 4.2 A summary of the in-cabin concentration reductions for UFP, BC, and $PM_{2.5}$

The in-cabin concentration reductions for UFP, BC, and $PM_{2.5}$ are summarized under different driving conditions (i.e., stationary, local, and freeway) with the four different filter types (i.e., no filter, in-use OEM, HEPA A, and HEPA B). The data are the average of the field observations and the standard deviation is given in parenthesis.

Pollutants		Filter Types	Stationary		Local		Freeway	
			In-cabin	Ambient	In-cabin	On-road	In-cabin	On-road
Particle	UFP (#/cm^3)	No filter	15006 *(6125)*	22418 *(12832)*	15368 *(5034)*	27446 *(9849)*	28826 *(10076)*	66292 *(26770)*
		In-use OEM	12373 *(5672)*	23292 *(12309)*	11302 *(3933)*	26026 *(7473)*	25916 *(11914)*	81282 *(44536)*
		HEPA A	6048 *(2904)*	23715 *(13464)*	6418 *(3039)*	27321 *(8323)*	15558 *(5421)*	72765 *(23677)*
		HEPA B	2264 *(2029)*	21508 *(9785)*	2455 *(1792)*	30075 *(11685)*	5726 *(2914)*	76549 *(39837)*
	BC (ng/cm^3)	No filter	2899 *(2169)*	2282 *(1462)*	2473 *(2869)*	2032 *(1181)*	4636 *(2610)*	3589 *(1708)*
		In-use OEM	2577 *(2121)*	2102 *(1407)*	2559 *(2819)*	2136 *(1384)*	4275 *(2250)*	4407 *(1795)*
		HEPA A	1061 *(2073)*	2192 *(1342)*	1399 *(2725)*	2182 *(1227)*	1433 *(2133)*	5175 *(2055)*
		HEPA B	1089 *(2632)*	2724 *(1245)*	915 *(2067)*	2412 *(1230)*	1343 *(2809)*	3036 *(1606)*
	$PM_{2.5}$ (μg/cm^3)	No filter	38 *(24)*	46 *(26)*	32 *(21)*	36 *(26)*	37 *(21)*	41 *(28)*
		In-use OEM	28 *(25)*	47 *(24)*	33 *(25)*	40 *(34)*	33 *(19)*	44 *(29)*
		HEPA A	15 *(15)*	34 *(25)*	10 *(5)*	38 *(33)*	11 *(7)*	40 *(28)*
		HEPA B	12 *(13)*	28 *(17)*	10 *(7)*	38 *(31)*	9 *(6)*	37 *(26)*
Gas	CO_2 (ppm)	No filter	1082 *(581)*	944 *(528)*	705 *(91)*	477 *(49)*	729 *(132)*	540 *(206)*
		In-use OEM	1067 *(625)*	957 *(653)*	711 *(98)*	481 *(54)*	729 *(146)*	526 *(160)*
		HEPA A	1268 *(663)*	1040 *(633)*	752 *(148)*	469 *(55)*	716 *(94)*	473 *(45)*
		HEPA B	1170 *(561)*	1022 *(577)*	792 *(132)*	470 *(54)*	746 *(111)*	472 *(48)*

4.4.3. Ventilation Air-flow Rate Reduction

The installation of HEPA filters may result in a large pressure drop that reduces the ventilation air-flow rate into the passenger cabin. Because the automotive ventilation systems primarily serve to offer thermal comfort to passengers, the reduction in the air-flow rate could become a critical limitation for in-cabin HEPA filter applications.

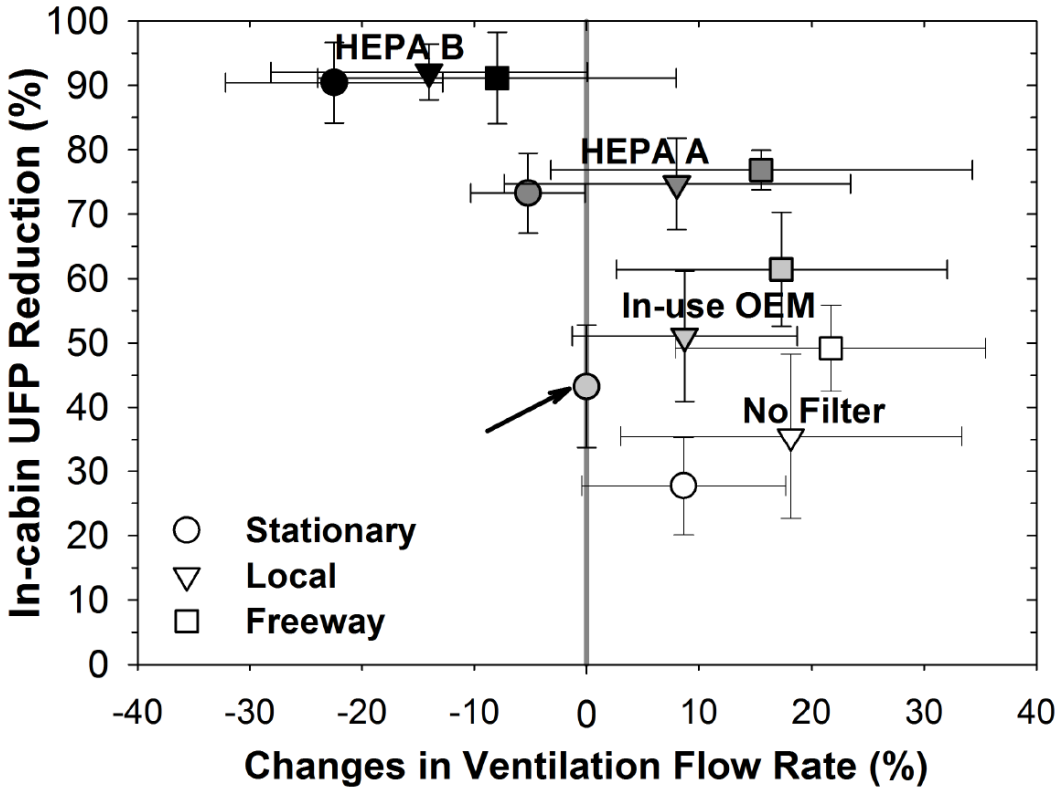


Figure 4.7 In-cabin ultrafine particle reductions and the changes in ventilation air-flow rates
Changes in ventilation flow rates by increasing in-cabin UFP reduction with use of different filters: HEPA B, HEPA A, in-use OEM, and no filter in different driving conditions. The changes were estimated relative to the ventilation flow rate measurements with in-use OEM filters in stationary condition for each vehicle (arrow, 306 m^3/h on average with ±101 m^3/h). The symbols and error bars are averages and standard deviations of the relative changes, respectively.

Figure 4.7 summarizes the ventilation air-flow rate changes and the in-cabin UFP reductions upon retrofitting with the in-cabin HEPA filters. The changes in the ventilation air-flow rates were estimated with respect to the air-flow rates measured with the in-use OEM filters for each of the individual test vehicles. With the in-use OEM filters, the air-flow rate was 306 m^3/h on average (± 101 m^3/h) across the test vehicle models under stationary conditions. The presented data are the means and standard deviations of all tested vehicle models under the different field conditions.

For all three driving conditions, the application of the HEPA B filters provided the most effective removal of the in-cabin UFPs with acceptable pressure drop. In comparison to the in-cabin UFP reduction demonstrated with the HEPA B filters, the in-cabin UFP reduction was lower in the case of the HEPA A filter and lower still for the in-use OEM filter and the no-filter cases. As expected, the changes in the air-flow rate exhibit an inverse relationship with the UFP reduction. A high in-cabin UFP reduction was observed using the HEPA B filters, and the associated ventilation air-flow rate was reduced by only 22, 12, and 7% under the stationary, local, and freeway conditions, respectively. Note that the ventilation air-flow rate increases due to the passive ventilation at increasing speed. Regardless of the filter types, the air-flow rate becomes higher on the freeway than on local roadways. Considering the advantageous in-cabin UFP reductions of 93% on average, this air-flow rate changes by additional pressure drop is acceptable. Installing cabin HEPA filters may also have other potential impacts (e.g., on fuel economy) which is beyond the scope of this work.

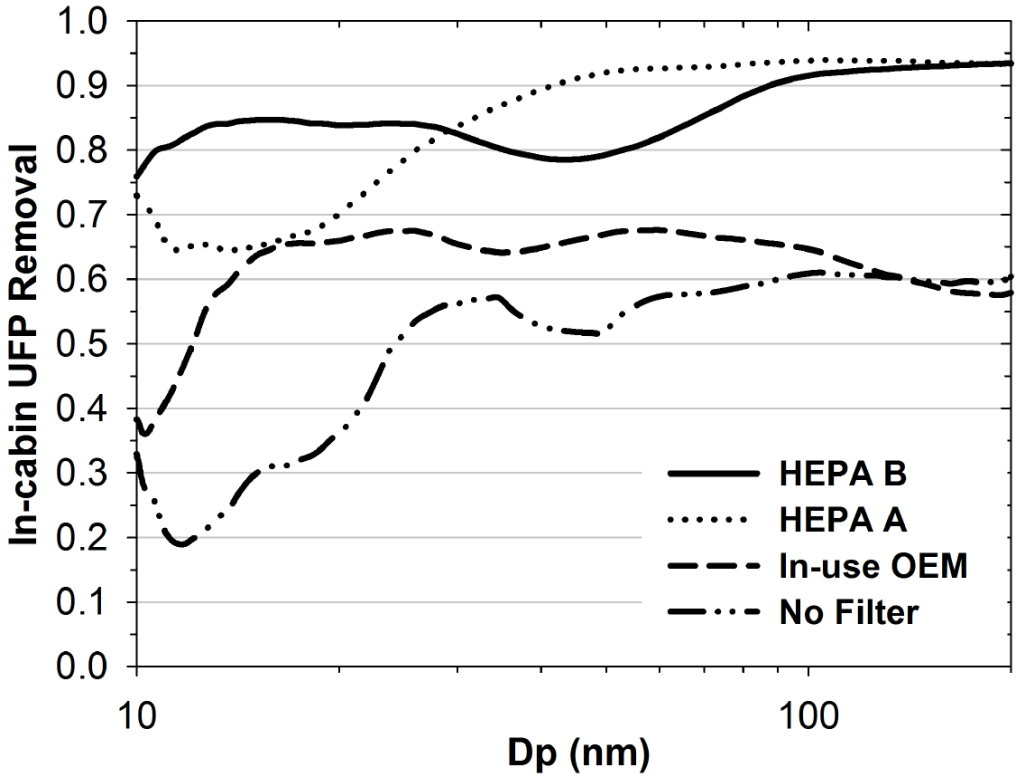


Figure 4.8 Size-specific particle removal efficiency of the four different filter types
Size-specific particle removal efficiencies are provided for HEPA B, HEPA A, in-use OEM, and no filter in field conditions. The plotted data are given with averages of all field conditions (i.e., stationary, local roadway, and freeway) with the specified filter types.

4.4.4. Size-resolved In-cabin UFP Reduction

Figure 4.8 shows the intrinsic UFP removal efficiency as a function of particle size. The in-cabin UFP removal for each filter type is the average of the field measurements under all three driving conditions. Unlike laboratory testing of filtration efficiency (see Figure 4.3 and 4.4), field measurement across different driving conditions advantageously considers realistic source particles from the different roadway scenarios as well as the effects of passive ventilation. Thus, the data presented in Figure 4.8 should be differentiated from the standardized laboratory testing that uses laboratory-generated particles under the same flow rate.

Across the particle size range from 10 to 200 nm, retrofitting with HEPA filters achieved much higher in-cabin UFP removal efficiencies than those obtained under the in-use OEM filter and no-filter scenarios. The results are similar to those previously discussed in relation to the reduction of particle concentrations. The in-cabin UFP removal across the different size ranges was most effective when using the HEPA B filter, followed by the HEPA A filter, the in-use OEM filter, and no filter. The removal efficiency of the no-filter case exhibited a significant decrease from 0.6 to 0.2 as the particle size decreased from 100 to 10 nm. Although the removal efficiency using the in-use OEM filter was relatively consistent at a level of 0.60-0.65 across the measured size range, it decreased considerably to 0.35 for particle sizes below 15 nm. In comparison, the removal efficiency of the HEPA A filter was consistently very high at approximately 93% for particle sizes down to 50 nm, with a decrease down to 0.65 for particle sizes below 50 nm. However, the application of the HEPA B filter enabled a high UFP removal ranging from 0.75 to 0.93 and consequently offered a more consistent performance with less variability across the measured size range than any of the other test filters.

The substantial differences in the size-specific particle removal of the four filter types indicate that the source particle size and associated size-specific removal efficiency of the cabin air filters are very important in reducing the in-cabin passenger exposures to UFPs. These findings demonstrate that a significantly large portion of the measured in-cabin UFPs include the particles with their size highly skewed toward the smaller size range, even after the filtration process with the HEPA A or the in-use OEM filters. As previously discussed, the deleterious health effects of UFPs are highly associated with the particle size. Therefore, a consistent particle removal across a wide range of particle sizes is important and is readily achievable via in-cabin HEPA B filters as demonstrated in Figure 4.8.

4.4.5. In-cabin Reduction of Nucleation Mode Particles

The application of a HEPA B filter successfully reduced in-cabin UFPs across a wide range of particle size. Figure 4.9 illustrates this reduction in comparison with the ambient conditions in the stationary (Figures 4.9a and b) and freeway (Figures 4.9c and d) conditions. Under the stationary conditions, use of the HEPA B filter resulted in a strong in-cabin concentration decay over time, and the changes in the size distribution were also independent of the particle size, resulting in consistent removal efficiency across a wide size range of particles, as shown in Figure 4.8. While maintaining consistent ambient particle size distributions in Figure 4.9a, the in-cabin UFP concentration decayed from 5,500 to 1,200 particles/cm^3. During this effective filtration process in stationary conditions, the mode diameter measured was approximately 70 nm and 60 nm in the ambient air and in-cabin, respectively.

Under freeway conditions, this study also observed a strong reduction in the in-cabin UFP concentrations of the freeway ambient particles in the nucleation mode at approximately 30 nm. Figure 4.9c presents the particle size distribution changes over a time series for the freeway ambient particles, and Figure 4.9d presents the in-cabin particle size distribution changes measured concurrently. Although the dynamic changes in the freeway UFPs did not mirror the decrease in the in-cabin UFP concentration and particle size that was observed in the stationary environment, the comparison of the freeway ambient and in-cabin environments still exhibited a strong mitigation of the UFPs in terms of their concentration and particle size. With HEPA B filter installation, the particle size-specific reduction improved by approximately one order of magnitude. This reduction is similar to the 93% reduction of in-cabin UFP number concentrations (previously discussed and shown in Figure 4.6) and occurred for all driving environments.

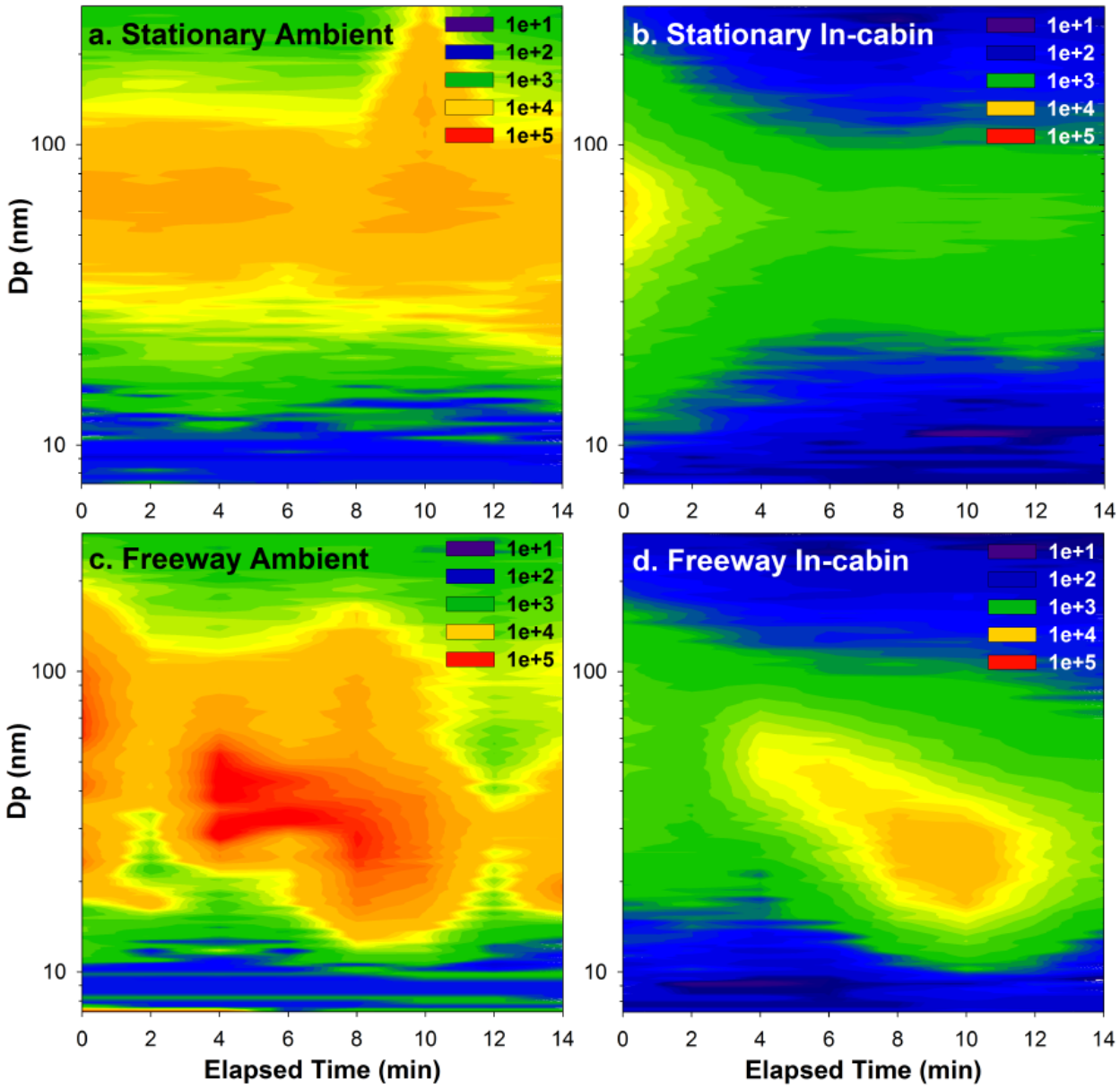


Figure 4.9 Size-resolved ultrafine particle number concentration changes in time series contour Size-resolved ultrafine particle number concentration contour plots in (a, b) stationary and (c, d) freeway conditions for (a, c) ambient and (b, d) in-cabin environments with HEPA B filter time series. Color intensity is the normalized particle concentration (dN/dLogDp) in log-scale with unit of particle/cm^3.

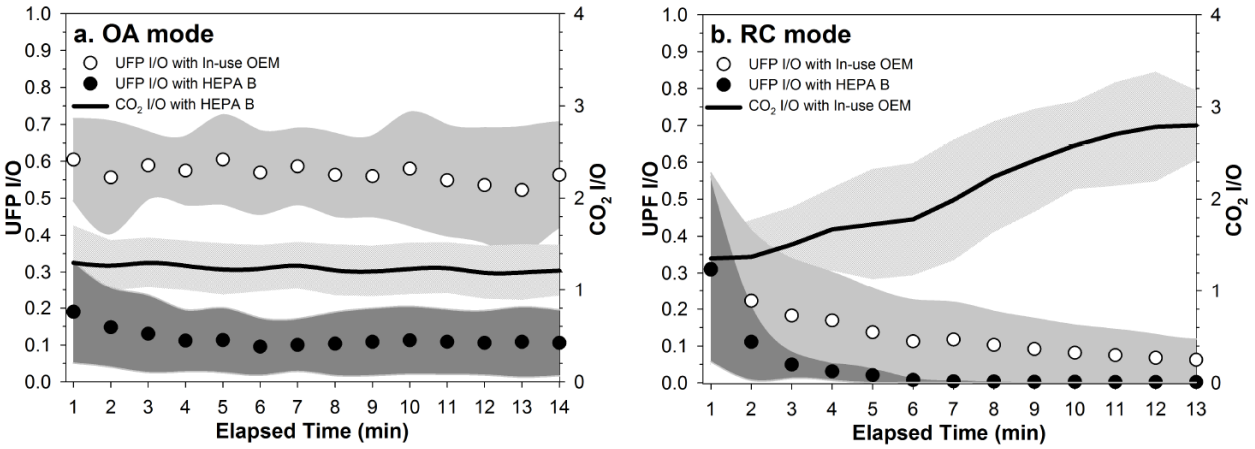


Figure 4.10 Simultaneous reduction of the in-cabin ultrafine particles and carbon dioxide
Simultaneous control of UFPs and CO_2 in (a) OA and (b) RC mode I/O, the changes of the UFPs (dots) and CO_2 (line) I/O ratios in comparison with HEPA B and in-use OEM filters. The symbols present the averages of the 1-minute average data from the test vehicle models in stationary condition. The shade shows the standard deviations.

4.4.6. Simultaneous Control of In-cabin UFPs and CO_2

Installing the HEPA B filters also allows for the simultaneous control of the UFP and CO_2 concentrations in passenger cabins. Figure 4.10 shows the I/O estimates under the stationary conditions in this study. Figure 4.10a presents the OA mode results, and Figure 4.10b compares the RC mode results for the in-use OEM and HEPA B filters. The plotted data are means, and the shades are the standard deviations of all test vehicles in time series.

As shown in Figure 4.10b, the RC mode is an effective in-cabin UFP control strategy, reducing the UFP I/O down to 0.07. However, this approach also imposes the unwanted problem of passenger-exhaled CO_2 accumulation, as shown in Figure 4.10b. During the same time period of RC filtration, the CO_2 I/O tripled with 1-2 passengers inside the vehicle cabin. The tripled CO_2 I/O is equivalent to a concentration from 2,500 to 4,000 ppm on average. Although the application of a HEPA filter in RC mode further reduced the in-cabin UFPs more rapidly than the

in-use OEM filters, the problem of CO_2 accumulation still remained at a similar magnitude (data not provided for clarity). Therefore, the current automotive ventilation system with the low filtration efficiency of the OEM filters is limited in its ability to control the UFP and CO_2 concentrations simultaneously.

To solve this problem, this study proactively utilized the OA-mode ventilation system to supply OA into the passenger cabin at the same medium fan setting while testing different filters. By retrofitting the existing automotive ventilation systems with the HEPA filters, this study reports a successful simultaneous control of both the UFP and CO_2 concentrations to reduce the in-cabin passenger exposures.

Figure 4.10a presents the time-series of the UFP I/O and CO_2 I/O in stationary condition with the application of a HEPA B filter in comparison with the application of the in-use OEM filter. In OA mode, supplying ambient air maintained the in-cabin CO_2 concentration at a low level that was slightly higher than the ambient level. Despite the variability of the different vehicle models, the proactive use of OA mode led the in-cabin CO_2 concentration to stabilize at 22% (in stationary vehicles with 1-2 passengers) on average higher than the ambient concentration. With 2 passengers in local and freeway conditions, the average in-cabin CO_2 concentrations were 69% (i.e., 792 ppm) and 58% (i.e., 746 ppm) higher than the ambient concentration (i.e., 470–472 ppm). Table 4.2 provides the concentration data in more detail.

Simultaneously, the in-cabin UFP concentrations also decreased and I/O stabilized at 0.07 in the OA mode with HEPA B filter. In comparison to the in-use OEM filter, which recorded a UFP I/O of 0.60, the application of the HEPA B filter achieved a substantially lower in-cabin UFP I/O. Regardless of the ambient concentration fluctuations in local and freeway conditions, the in-cabin UFP concentration exhibited at an order of magnitude lower than the ambient level

with HEPA B filter. As shown in Figure 4.10b, for RC mode, the effectiveness of the HEPA B filter is also greater than that of the in-use OEM filter.

Consequently, application of the in-cabin HEPA filters achieved an average UFP reduction of 93% under the field conditions while maintaining a CO_2 concentration that was only at 635-924 ppm with 2 passengers in local and freeway driving conditions than the ambient concentration. This concentration is much less than the CO_2 concentration in the RC mode, which reached 2,500-4,000 ppm over the same time period. In conclusion, the proactive use of the OA mode with an automotive cabin HEPA filtration is a highly desirable control method for the simultaneous reduction of in-cabin exposures to UFPs and CO_2.

References

(1) Gilmour, P. S.; Ziesenis, A.; Morrison, E. R.; Vickers, M. A.; Drost, E. M.; Ford, I.; Karg, E.; Mossa, C.; Schroeppel, A.; Ferron, G. A.; Heyder, J.; Greaves, M.; MacNee, W.; Donaldson, K. Pulmonary and systemic effects of short-term inhalation exposure to ultrafine carbon black particles. *Toxicology and Applied Pharmacology* **2004**, *195*, 35-44.

(2) Hamoir, J.; Nemmar, A.; Halloy, D.; Wirth, D.; Vincke, G.; Vanderplasschen, A.; Nemery, B.; Gustin, P. Effect of polystyrene particles on lung microvascular permeability in isolated perfused rabbit lungs: Role of size and surface properties. *Toxicology and Applied Pharmacology* **2003**, *190*, 278-285.

(3) Kreyling, W. G.; Semmler, M.; Erbe, F.; Mayer, P.; Takenaka, S.; Schulz, H.; Oberdorster, G.; Ziesenis, A. Translocation of ultrafine insoluble iridium particles from lung epithelium to extrapulmonary organs is size dependent but very low. *Journal of Toxicology and Environmental Health-Part A* **2002**, *65*, 1513-1530.

(4) Nemmar, A.; Hoet, P. H. M.; Vanquickenborne, B.; Dinsdale, D.; Thomeer, M.; Hoylaerts, M. F.; Vanbilloen, H.; Mortelmans, L.; Nemery, B. Passage of inhaled particles into the blood circulation in humans. *Circulation* **2002**, *105*, 411-414.

(5) Nemmar, A.; Hoylaerts, M. F.; Hoet, P. H. M.; Nemery, B. Possible mechanisms of the cardiovascular effects of inhaled particles: Systemic translocation and prothrombotic effects. *Toxicology Letters* **2004**, *149*, 243-253.

(6) Nemmar, A.; Vanbilloen, H.; Hoylaerts, M. F.; Hoet, P. H. M.; Verbruggen, A.; Nemery, B. Passage of intratracheally instilled ultrafine particles from the lung into the systemic circulation in hamster. *American Journal of Respiratory and Critical Care Medicine* **2001**, *164*, 1665-1668.

(7) Oberdorster, G. Pulmonary effects of inhaled ultrafine particles. *International Archives of Occupational and Environmental Health* **2001**, *74*, 1-8.

(8) Oberdorster, G.; Sharp, Z.; Atudorei, V.; Elder, A.; Gelein, R.; Kreyling, W.; Cox, C. Translocation of inhaled ultrafine particles to the brain. *Inhalation Toxicology* **2004**, *16*, 437-445.

(9) Li, N.; Sioutas, C.; Cho, A.; Schmitz, D.; Misra, C.; Sempf, J.; Wang, M. Y.; Oberley, T.; Froines, J.; Nel, A. Ultrafine particulate pollutants induce oxidative stress and mitochondrial damage. *Environmental Health Perspectives* **2003**, *111*, 455-460.

(10) Sioutas, C.; Delfino, R. J.; Singh, M. Exposure assessment for atmospheric ultrafine particles (ufps) and implications in epidemiologic research. *Environmental Health Perspectives* **2005**, *113*, 947-955.

(11) Elder, A.; Couderc, J.-P.; Gelein, R.; Eberly, S.; Cox, C.; Xia, X.; Zareba, W.; Hopke, P.; Watts, W.; Kittelson, D.; Frampton, M.; Utell, M.; Oberdorster, G. Effects of on-road highway aerosol exposures on autonomic responses in aged, spontaneously hypertensive rats. *Inhalation Toxicology* **2007**, *19*, 1-12.

(12) Hitchins, J.; Morawska, L.; Wolff, R.; Gilbert, D. Concentrations of submicrometre particles from vehicle emissions near a major road. *Atmospheric Environment* **2000**, *34*, 51-59.

(13) Shi, J. P.; Khan, A. A.; Harrison, R. M. Measurements of ultrafine particle concentration and size distribution in the urban atmosphere. *Science of the Total Environment* **1999**, *235*, 51-64.

(14) Westerdahl, D.; Fruin, S.; Sax, T.; Fine, P. M.; Sioutas, C. Mobile platform measurements of ultrafine particles and associated pollutant concentrations on freeways and residential streets in los angeles. *Atmospheric Environment* **2005**, *39*, 3597-3610.
(15) Zhu, Y. F.; Eiguren-Fernandez, A.; Hinds, W. C.; Miguel, A. H. In-cabin commuter exposure to ultrafine particles on los angeles freeways. *Environmental Science & Technology* **2007**, *41*, 2138-2145.
(16) Zhu, Y.; Fung, D. C.; Kennedy, N.; Hinds, W. C.; Eiguren-Fernandez, A. Measurements of ultrafine particles and other vehicular pollutants inside a mobile exposure system on los angeles freeways. *Journal of the Air & Waste Management Association* **2008**, *58*, 424-434.
(17) Klepeis, N. E.; Nelson, W. C.; Ott, W. R.; Robinson, J. P.; Tsang, A. M.; Switzer, P.; Behar, J. V.; Hern, S. C.; Engelmann, W. H. The national human activity pattern survey (nhaps): A resource for assessing exposure to environmental pollutants. *Journal of Exposure Analysis and Environmental Epidemiology* **2001**, *11*, 231-252.
(18) Fruin, S.; Westerdahl, D.; Sax, T.; Sioutas, C.; Fine, P. M. Measurements and predictors of on-road ultrafine particle concentrations and associated pollutants in los angeles. *Atmospheric Environment* **2008**, *42*, 207-219.
(19) Qi, C.; Stanley, N.; Pui, D. Y. H.; Kuehn, T. H. Laboratory and on-road evaluations of cabin air filters using number and surface area concentration monitors. *Environmental Science & Technology* **2008**, *42*, 4128-4132.
(20) Xu, B.; Liu, S. S.; Liu, J. J.; Zhu, Y. F. Effects of vehicle cabin filter efficiency on ultrafine particle concentration ratios measured in-cabin and on-roadway. *Aerosol Science and Technology* **2011**, *45*, 234-243.
(21) Pui, D. Y. H.; Qi, C.; Stanley, N.; Oberdorster, G.; Maynard, A. Recirculating air filtration significantly reduces exposure to airborne nanoparticles. *Environmental Health Perspectives* **2008**, *116*, 863-866.
(22) U.S. EPA Fuel economy database, 2012. http://www.fueleconomy.gov/feg/download.shtml (accessed Sep 7, 2012).
(23) Hinds, W. C. *Aerosol technology: Properties, behavior, and measurement of airborne particles*; 2nd, ed.; Wiley: New York, 1999.
(24) Lee, E. S.; Stenstrom, M. K.; Zhu, Y. F. Ultrafine particle infiltration into passenger vehicles: Effects of driving speed and ventilation condition. *Environmental Science & Technology* (in review)

5. CONCLUSIONS

Previous epidemiological and toxicological studies have presented strong evidences supporting deleterious health effects of UFPs. Despite abundant presence of UFPs in roadway environments and less-controlled UFP penetrations to the passenger vehicle cabins, the in-cabin micro-environment has been largely overlooked while previous research efforts have primarily dedicated to near-freeway, on-roadway, and building indoor environments for the past two decades.

Automotive cabin is a unique micro-environment which requires different approaches from the previous building indoor environment studies because of strong aerodynamic effects and different mechanical ventilation system in addition to the complexity of on-road UFP dynamics. Thereby, the limited empirical or quantitative understating of in-cabin air quality restricted to develop effective control of in-cabin air quality to better protect passenger exposures.

To develop effective in-cabin air quality control strategy, this dissertation aimed to identify the infiltration problem and to improve quantitative understanding of in-cabin UFP dynamics. Subsequently, this dissertation work proposes the simultaneous control method for in-cabin UFPs and CO_2 with application of an automotive cabin HEPA filter.

Investigation of automotive envelope leakage and infiltration found that the aerodynamic pressure changes on a moving vehicle envelope enable UFP infiltration. However, the occurrence of UFP infiltration resulted dominantly from the leakage at rear trunk rather than the side doors regardless of ventilation settings, driving speed, and even vehicle types; whereas, the magnitude of the infiltrated portion of UFPs was still dependant upon those three parameters.

From quantification of the infiltration, this study proposed in-cabin UFP dynamics

model to enable time-series simulation of in-cabin UFP dynamic behavior at any given time, driving speed, and ventilation settings. As taking into account two dynamic sub-functions of infiltration and passive ventilation with respect to driving speed, this semi-empirical modeling study demonstrated the competition of two pressures (i.e., aerodynamic pressure and in-cabin pressure driven by mechanical ventilation) to determine the presence of UFP infiltration over a wide range of driving speeds. The work also demonstrated dynamic changes of in-cabin UFPs due to dynamic contributions of each of the five UFP gain / loss mechanisms: (1) active OA ventilation, (2) passive OA ventilation, (3) RC filtration, (4) infiltration, and (5) surface deposition. Accordingly, the dynamic changes of in-cabin UFPs were observed primarily because of changes in driving speed.

In order to control in-cabin UFPs and CO_2 accumulation, this study proposed the proactive use of OA mode ventilation with an automotive cabin HEPA filter. While maintaining low pressure drop of the filter, this method achieved to reduce the in-cabin UFP concentration by 93% on average under field conditions. In comparison to 41-65% UFP removal by the in-use OEM filters, the use of this approach is promising and validated across 12 different vehicle models representing diverse vehicle models and types. More importantly, throughout the measurements, the in-cabin CO_2 concentration remained in the rage of 635-924 ppm, which proves a significant reduction from the typical CO_2 concentration range of 2500-4000 ppm in RC mode for the same period time. This approach also enabled the in-cabin micro environment to be more independent of the changes in the driving speed and the fluctuations in the UFP concentrations on different roadways.

APPENDICES

Contents lists available at SciVerse ScienceDirect

Atmospheric Environment

journal homepage: www.elsevier.com/locate/atmosenv

Measurements of ultrafine particles carrying different number of charges in on- and near-freeway environments

Eon S. Lee [a], Bin Xu [b], Yifang Zhu [c,*]

[a] Department of Civil and Environmental Engineering, Henry Samueli School of Engineering and Applied Science, University of California Los Angeles, Los Angeles, CA 90095-1593, USA
[b] State Key Laboratory of Pollution Control and Resource Reuse, Tongji University, Shanghai 200092, China
[c] Department of Environmental Health Sciences, Jonathan and Karin Fielding School of Public Health, University of California Los Angeles, Los Angeles, CA 90095-1772, USA

HIGHLIGHTS

- Electrical charges on ultrafine particles (UFPs) were measured on- and near-freeways.
- The fractions of charged UFPs were significantly higher on the freeways than in the background.
- Charged particles decayed faster than total particles but slower than ion downwind from the freeway.
- Strong net positive charges were found on nucleation mode particles near freeways.

ARTICLE INFO

Article history:
Received 8 April 2012
Received in revised form
24 June 2012
Accepted 28 June 2012

Keywords:
Ultrafine particle
Freeway
Charge

ABSTRACT

This paper presents measurements of electrical charges on ultrafine particles (UFPs) of different electrical mobility diameters (30, 50, 80, and 100 nm) in on- and near-freeway environments. Using a tandem Differential Mobility Analyzer (DMA) system, we first examined the fraction of UFPs carrying different number of charges on two distinctive freeways: a gasoline-vehicle dominated freeway (I-405) and a heavy-duty diesel truck dominated freeway (I-710). The fractions of UFPs of a given size carrying one or more charges were significantly higher on the freeways than in the background. The background UFPs only carried up to two charges but freeway UFPs could have up to three charges. The total fraction of charged particles was higher on the I-710 than I-405 across the studied electrical mobility diameters. Near the I-405 freeway, we observed a strong decay of charged particles on the downwind side of the freeway. We also found fractional decay of the charged particles was faster than total particle number concentrations, but slower than total ion concentrations downwind from the freeway I-405. Among charged particles, the highest decay rate was observed for particles carrying three charges. Near the I-710 freeway, we found strong net positive charges on nucleation mode particles, suggesting that UFPs were not at steady-state charge equilibrium near freeways.

© 2012 Elsevier Ltd. All rights reserved.

1. Introduction

Traffic emissions usually constitute the largest source of ultrafine particles (UFPs, $D_P < 100$ nm) in an urban environment (Shi et al., 2003). Several studies have found that the combustion process in the engine generated ion concentrations in the range of 10^8–10^{11} cm^{-3} (Fialkov, 1997; Yu et al., 2004). Nucleation mode UFP formation occurs in the presence of high ion concentrations (Yu, 2001). Once generated, the ion concentration drops rapidly with increasing distance from the source as a result of dissipation through either ion–ion recombination or ion-particle attachment (Arnold et al., 2000). In the process of ion-particle collisions, UFPs take different number of positive or negative charges (n charges).

The presence of the charges on particles may substantially affect coagulation and particle transport mechanisms. Leppa et al. (2011) have shown that charged particles enhanced the coagulation process. They found that particles carrying n charges increased coagulation-driven particle growth rate by a factor of 1.5–2 and resulted in a decreased particle number concentration. The enhanced coagulation not only makes particle grow in size but also changes agglomerate geometry, and thus modifies particle diffusion coefficients (Jacobson and Seinfeld, 2004). Subsequently, the change in diffusion

* Corresponding author. Tel.: +1 310 825 4324; fax: +1 310 794 2106.
E-mail address: Yifang@ucla.edu (Y. Zhu).

1352-2310/$ – see front matter © 2012 Elsevier Ltd. All rights reserved.
http://dx.doi.org/10.1016/j.atmosenv.2012.06.085

coefficient affects particle transport behaviors. For example, electric charges on smaller UFPs were found to contribute to a lower penetration factor across idealized vehicle cracks (Xu et al., 2010).

Besides coagulation and penetration, the electric charges on particles are also important to understand particles scavenged by the atmospheric water droplets. In comparison to neutral particles, the charged particles have about an order of magnitude higher scavenging coefficients than the neutral particles at a diameter of 100 nm; whereas, the scavenging coefficients of charged particles become comparable to those of neutral particles at diameters less than 10 nm (Andronache, 2004). Thereby scavenging effects is more important in the size range of the Greenfield gap (i.e., 10 nm $< D_p <$ 2 μm) (Tinsley et al., 2000). Scavenging coefficients are found approximately two orders of magnitude higher for 1-nm particles than for 100-nm particles (Andronache, 2004). Since the changes in scavenging coefficient occur from the electrical image force of charged particles, scavenging effects are independent from the charges of the water droplets (Tripathi and Harrison, 2002).

Charged particles have been previously observed in combustion processes. Kim et al. (2005) has used a tandem Differential Mobility Analyzer (DMA) system to study charged particle distributions in a lab-scale combustion system with ethylene gas as the fuel. The fraction of charged particles from gasoline and diesel engine exhausts has also been studied with a similar tandem DMA system (Maricq, 2006). Both studies found agreement between the measurements and charge equilibrium theory at high temperature (i.e., 800–1300 K). However, these results may not be directly applicable to charged particles at ambient temperature on and near-roadways since the charge equilibrium theories are a strong function of the temperature.

Previous studies have also reported high concentrations of UFPs in the on- and near-roadway atmosphere with sharp concentration decay downwind from the freeways (Zhu et al., 2002a, 2002b). A recent study found that cluster ion concentrations have even greater decay rates as a function of distance away from a freeway than UFP number concentrations (Jayaratne et al., 2010). An ion concentration in the range of 400–600 cm^{-3} has been reported in the near-roadway atmospheres (Ling et al., 2010).

No study, to the best of our knowledge, has experimentally quantified the fraction of UFPs carrying n charges on and at increasing distances downwind from roadways. This knowledge gap limits our understanding of particle dynamics (e.g., coagulation, transport, transformation, and scavenging) in the on- and near-roadway atmospheres. In this paper, we report the fraction of charged particles observed on and near two major Los Angeles freeways (i.e., I-405 and I-710) and discuss the effects of charge polarity with respect to particle size and number of charges.

2. Methodology

2.1. Instrumentation

2.1.1. Tandem DMA configurations

A tandem DMA system with two differential mobility analyzers (DMA, Model 3080, TSI Inc., St. Paul, MN) in series was used in this study. Fig. 1 illustrates the schematic experimental setup of the tandem DMA system configuration. The selector DMA allows UFPs of a certain electrical mobility to go through. While maintaining the same particle electrical mobility, particles carrying both single and multiple charges pass through the selector DMA. Since the electrical mobility is a function of both number of charges and particle diameter (See Eq. (1)), particles carrying different number of charges have different sizes accordingly. For example, doubly charged particles have a diameter larger than singly charged particles. Similarly, the diameter of particles carrying triple charges is always larger than that of particles carrying double charges.

Particles from the selector DMA are then classified by the number of charges in the following SMPS system – a combination of an electrostatic classifier (Model 3080, TSI Inc., St. Paul, MN), a second DMA (Model 3081, TSI Inc., St. Paul, MN), and a condensation particle counter (Model 3785, TSI Inc., St. Paul, MN). The selected particles first pass through a Kr^{85} neutralizer (Model 3077A, TSI Inc., St. Paul, MN) to redistribute the charges on the particles, whereby most of the multiply charged particles are brought to Boltzmann equilibrium charge distributions with less than 10% remained in multiple charge states (Wiedensohler and Fissan, 1991). The second DMA classifies the particles in 102 channels of particles diameter. Consequently, the tandem DMA system presents particle size distributions with multiple modes. Each mode corresponds to the size of the charged particles carrying different number of charges. The primary mode indicates singly charged particles. Particles having double- and triple-charges can be found at secondary and tertiary modes, respectively. Therefore, number concentration of particles with different number of charges can be determined from the spectra of the tandem DMA system.

2.1.2. Instrument set-up

In this study, the selector DMA was set to sample UFPs of four different electrical mobility diameters (i.e., 30, 50, 80, and 100 nm) representing the typical particle size range observed on- and near-freeways. Scanning in the range of 7–289 nm, the SMPS system characterizes the number concentrations of the charged particles. The experiments were conducted for particles having both positive and negative charges. It should be noted that only particles carrying positive charges were detected with the default electrostatic classifier setup. To measure the concentration of particles with negative charges, the polarity of the high voltage applied to the center DMA rod was reversed by installing a positive high voltage power supply unit (Model 10A12-P4-M, TSI Inc., St. Paul, MN).

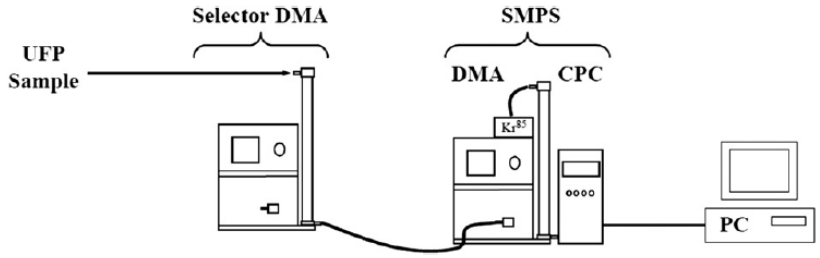


Fig. 1. A schematic of the experimental setup: the tandem Differential Mobility Analyzer (DMA) system includes a selector DMA and a Scanning Mobility Particle Sizer (SMPS). The Kr^{85} charge neutralizer was installed only on the SMPS system.

2.2. Experimental

Using the same instrumental set-up described above, the measurements were repeated in on- and near-freeway environments.

2.2.1. On-freeway environment

A vehicle equipped with the aforementioned tandem DMA system was employed for on-freeway experiments. During on-freeway measurements, a sampling inlet was placed outside the vehicles to bring on-freeway UFPs into the instruments when driving in the middle lane. Since different engine types and loadings lead to different ion concentrations (Yu et al., 2004), two distinguishable freeways were selected to represent different traffic environments: [1)] a gasoline-vehicle dominated freeway (I-405 with less than 5% of heavy-duty diesel truck traffic) and [2)] a diesel-truck dominated freeway (I-710 with approximately 20%

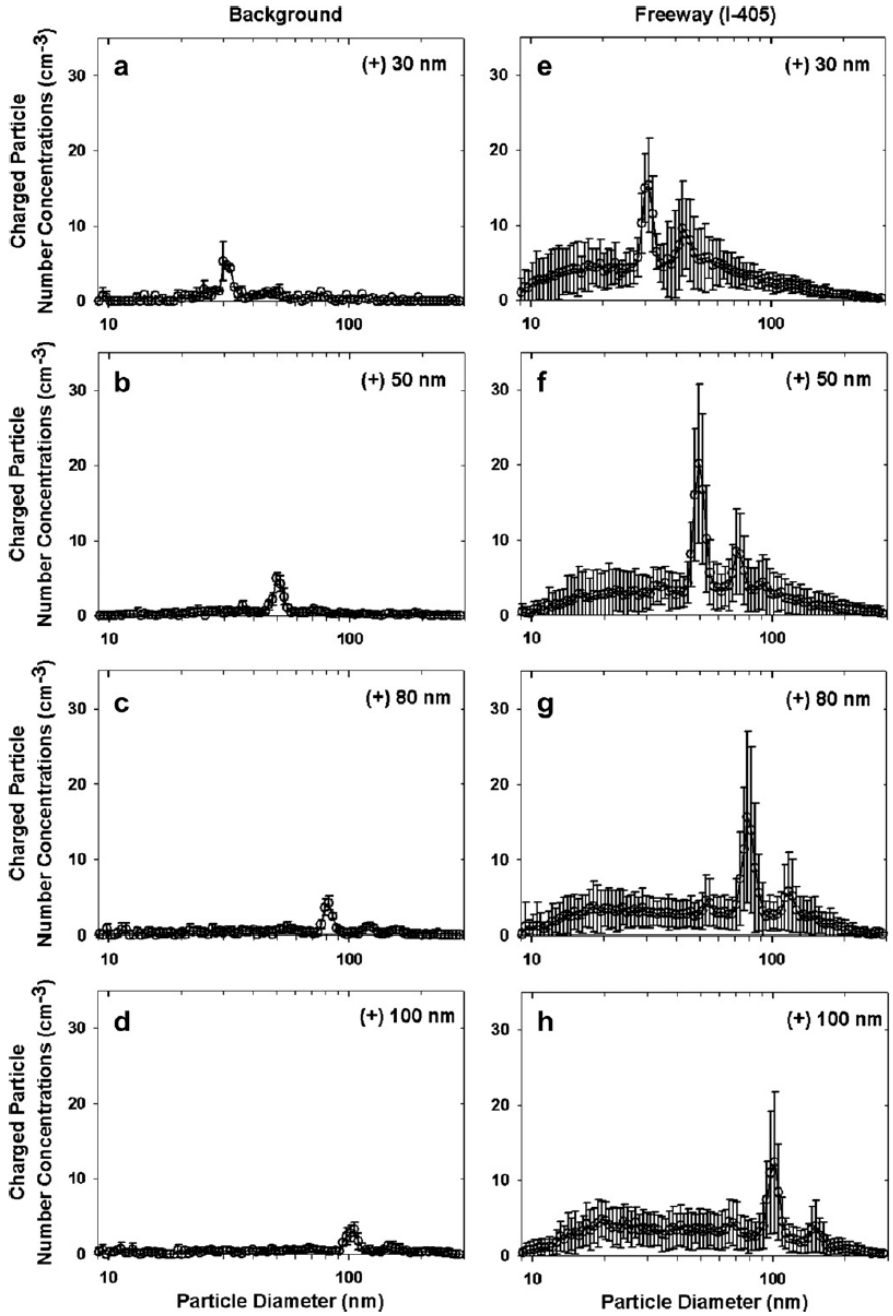


Fig. 2. Size distributions of positively charged particles are presented at different electrical mobility diameters: 30 nm (panels a, e), 50 nm (panels b, f), 80 nm (panels c, g), and 100 nm (panels d, h) in the background (panels a–d) and on the I-405 freeway (I-405, panels e–h). The circle symbols and the error bars are the average and one standard deviation of the observations.

of heavy-duty diesel truck traffic). While I-405 is widely used as a commuting route, I-710 is a major truck route in Southern California. Because diurnal traffic volume changes have regular patterns during weekdays, to minimize the effects of varying traffic volume, measurements were conducted in the afternoon (from 2 to 6 pm) on six different weekdays: four days (i.e., 3/3, 3/29, 4/13, and 4/25 in 2011) on the I-405 and two days (i.e., 12/14/2010 and 1/28/2011) on the I-710. The same instrument set-up and experimental protocols were applied to the measurements on both freeways.

2.2.2. Near-freeway environment

The near-freeway measurements of charged particles were conducted on Constitution Avenue at the Los Angeles National Cemetery, located on the east side of the I-405 freeway. The selected site was desirable because of its proximity to the freeway and the lack of nearby UFP emission sources other than emissions from the freeway traffic. During the sampling periods, there was a consistent eastward sea breeze (1.78 ± 0.89 m s^{-1}) carrying UFPs emitted on the freeway directly to the sampling locations. Measurements were taken upwind and at 10, 20, 50, and 100 m downwind from the edge of I-405 and repeated in the afternoon (from 12 to 3 pm) on four different days (i.e., 2/22, 3/10, 3/29, and 4/25 in 2011). A detailed description of the study site can be found elsewhere (Zhu et al., 2002b).

2.2.3. Electric charge polarity

To characterize charge polarity, both positively and negatively charged particles were measured near the I-710 freeway in Long Beach, CA. The I-710 freeway generally runs from north to south but the studied section runs 30° to the east. A large flood plain and Los Angeles River are located on the immediate east side of the freeway. There is no significant source of UFPs or any charged particles in the study area other than freeway traffic emissions. In a close proximity to the freeway (15 m from the edge of the 710 freeway), we measured both positive and negative charges on particles of predetermined electrical mobility diameters (i.e., 30, 50, 80, and 100 nm). For each combination of particle size and polarity, data were collected for 24 h continuously. The total experimental period lasted for eight days (11/17 through 11/25 in 2011). Only data collected when the wind direction was about perpendicular to the freeway center-line and at a $300° \pm 45°$ angle were used for freeway emissions. Data collected when the wind direction was about perpendicular to the 710 center-line but at a $120° \pm 45°$ angle were classified as background concentration.

2.3. Analytical

We examined the discrete peaks in SMPS size distribution profiles to determine the fractions of particles carrying different numbers of positive or negative charges. For example, for a selected electrical mobility diameter, the singly charged particles were found at the highest peak of the smallest particle size among all concentration peaks. Particle at this peak representing singly charged particles (i.e., $n = 1$ in Eq. (1)), remained at the electrical mobility diameter preset by the selector DMA. The doubly charged particles were found at a secondary mode that was larger than the primary mode diameter in the size distribution. Similarly, the triply charged particles could be found at a tertiary mode diameter: always larger than the secondary mode diameter.

To verify that each mode diameter corresponds to particles carrying n charges but with the same electric mobility, the following particle electrical mobility equation (Willeke and Baron, 1993) was used:

$$Z_P = \frac{neC}{3\pi\mu D_P} \tag{1}$$

$$C = 1 + \frac{2\lambda}{D_P}\left(1.257 + 0.40\cdot\exp^{-\frac{0.55\cdot D_P}{\lambda}}\right) \tag{2}$$

where, Z_P is the particle electrical mobility (m^2 s V^{-1}); n is the number of electric charges (−); e is the elementary charge (1.6×10^{-19} C); μ is air viscosity (1.78×10^{-5} kg m^{-1} s^{-1}); D_P is particle diameter (m); C is Cunningham slip correction factor, which can be calculated from Eq. (2); and λ is the air mean free path (6.8×10^{-8} m).

The fractions of particles carrying different charges (e.g., +1, +2, +3, −1, −2, and −3) were then estimated by dividing the charged particle concentrations with the total particle concentrations of each mode.

$$(\text{Fraction of UFPs carrying } n \text{ charges}) = \frac{(\text{Charged particle number concentration at a mode diameter})}{(\text{Particle number concentration at the corresponding mode diameter})} \times 100 \tag{3}$$

Depending on the number of charges, the corresponding mode can be primary ($n = 1$), secondary ($n = 2$), and tertiary ($n = 3$). Eq. (3) was then applied to determine the fractions of particles carrying n positive or n negative charges on and near freeways.

3. Results and discussion

3.1. Charged UFPs on freeways

Freeway UFPs of four electric mobility diameters of 30, 50, 80, and 100 nm were investigated. Fig. 2 displays the size spectra of particles with n positive charges in the background (Fig. 2a–d) and

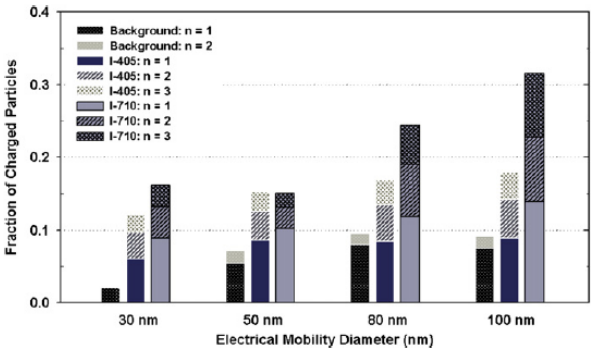


Fig. 3. Average fractions of charged particles measured in the background, and on the freeways I-405 and I-710 with respect to different electrical mobility diameters. Background data were collected near the I-710 freeway under upwind conditions.

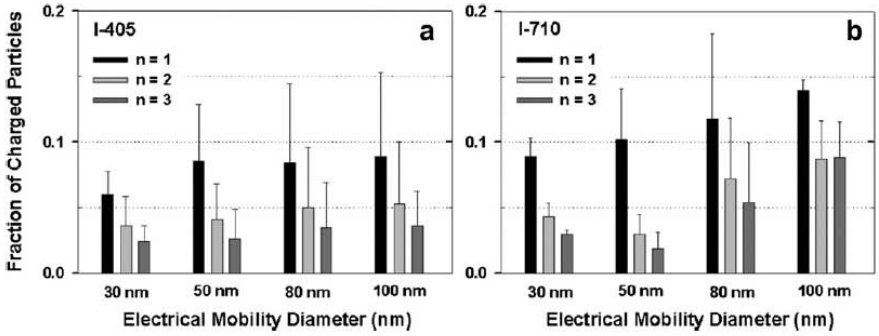


Fig. 4. Fraction of charged particles on (a) the I-405 and (b) the I-710 are plotted by the number of charges (n) at four different electrical mobility diameters: 30, 50, 80, and 100 nm. The error bars represent one standard deviation.

on the I-405 freeway (Fig. 2e–h). Concentrations of charged particles (Fig. 2e–f) were approximately ten-fold higher on the I-405 (Fig. 2a–d), primarily because particle concentrations were much higher on the freeway than in the upwind background. The overall distributions exhibit multi-modes. Primary and secondary modes indicate number concentrations of singly and doubly charged particles, respectively. The diameter (D_P) of the doubly charged particles from the theoretical calculation (Eqs. (1) and (2)) quantitatively matches the experimental measurement shown in Fig. 2. For example, doubly charged particles having an electrical mobility diameter of 30 nm (i.e., $n = 2$ in Eq. (1)) are equivalent to singly charged particles having an electrical mobility diameter of 42 nm, which is close to 43 nm as indicated by the secondary mode in Fig. 2e. Similar results were obtained for other electrical mobility diameters presented in Fig. 2.

UFPs on the freeway can take up to three charges (Fig. 2e–h) whereas the background particles carry only up to two charges (Fig. 2a–d). This is likely because particles emitted from engine combustion processes tend to carry more charges. A previous study reported that UFPs from direct measurements of tailpipe emissions could have up to four charges (Maricq, 2006). Since particles collected on-freeways experienced much longer residence time in the atmosphere than particles directly emitted from the engine exhaust, highly charged ($n = 4$) particles may dissipate immediately in the process of collision with oppositely charged ions or particles before being sampled on the freeway. This may explain why no UFPs with four charges were observed in this study.

Fig. 3 compares the fraction of charged particles in different environments: at the background, and on freeways I-710 and I-405. The fraction of 30 nm particles carrying n charges was the lowest among the four studied electrical mobility diameters. The fraction increases with increasing particle electrical mobility diameter. The highest fractions were commonly found at 100 nm for all comparisons. This observation concurs with Boltzmann charge equilibrium theory in that larger particles would acquire more electric charges due to greater surface areas for ion collisions.

As shown in Fig. 3, the fraction of particles carrying n charges varied substantially under different conditions. In the background, the fraction of particles carrying at least one charge remained less than 10% for the studied electrical mobility diameters. In contrast, a much higher fraction of charged particles (e.g., up to 32% for 100 nm particles) was found on the two freeways. Across all studied

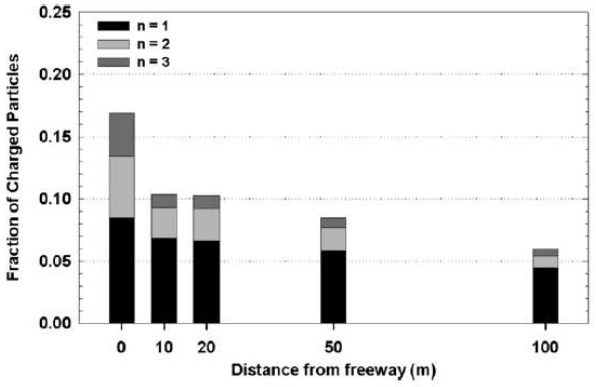


Fig. 5. Fractional changes of charged particles at electrical mobility diameters of 80 nm are presented as a function of downwind distances from the I-405 freeway: 0 m (on the freeway), 10, 20, 50, and 100 m from the edge of the I-405. Different schemes of shade symbolize different number of positive charges (n).

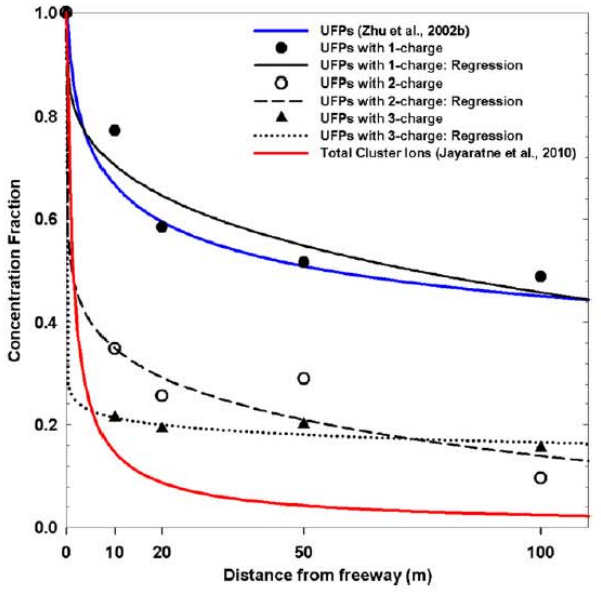


Fig. 6. Normalized concentrations of 80 nm particles carrying n charges as a function of downwind distances from the I-405 freeway. Data were compared to the decay profiles of total particle number concentration (Zhu et al., 2002b) and total cluster ions (Jayaratne et al., 2010) downwind of freeways.

Table 1
A summary of near-freeway pollutant decay functions for ultrafine particles (UFPs) carrying n charges and for total particle number concentration and total cluster ions reported in previous studies.

Measured species near freeways	Number of charges (n)	Regression equations	Determination coefficients (R^2)	Sources
Total particle number concentration	n/a	$y = (x+1)^{-0.18}$	0.84	Zhu et al. (2002b)
UFPs carrying n charges	1	$y = (x+1)^{-0.16}$	0.95	This study
	2	$y = (x+1)^{-0.42}$	0.97	
	3	$y = (x+1)^{-0.51}$	0.97	
Total cluster ions	n/a	$y = (x+1)^{-0.80}$	0.83	Jayaratne et al. (2010)

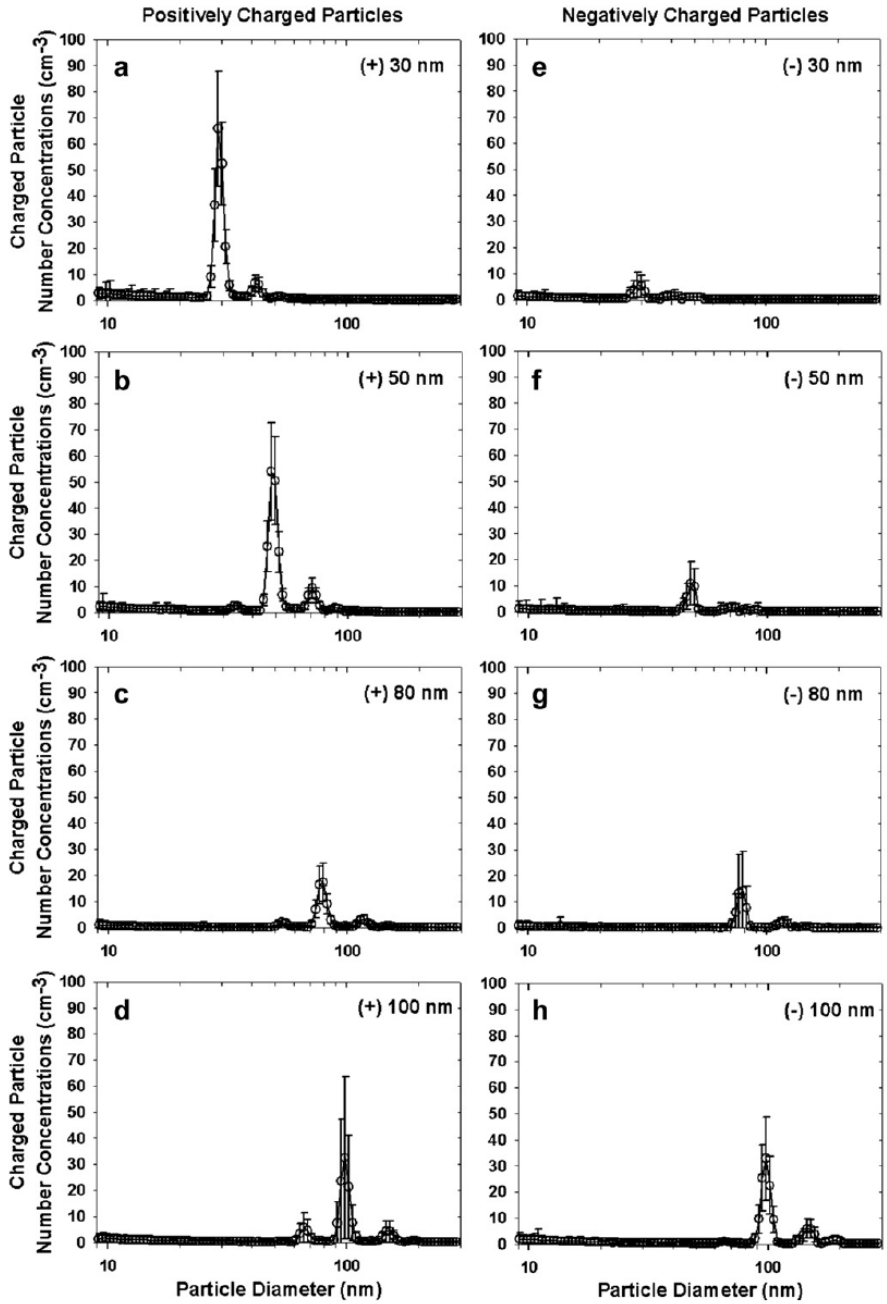


Fig. 7. Positively (panels a–d, on the left) and negatively (panels e–h, on the right) charged particle distributions measured near the I-710 freeway. Data were presented for different combinations of electrical mobility diameters and polarities: ±30, ±50, ±80, and ±100 nm. The circle symbols and the error bars are the average and one standard deviation of the observations.

electrical mobility diameters, the fractions of particles carrying two and three charges were much higher on the freeways than in the background. Specifically, 30 nm particles hardly took more than one charge at the upwind background location. However, higher fractions of particles carrying two or three charges were observed on the freeways. It suggests that motor-vehicle emissions are a strong source contributing to not only UFPs number concentrations but also a high fraction of charged particles in the atmosphere.

The high fraction of charged particles observed on and near freeways will likely increase particle coagulation rates in comparison with the background. As indicated in Leppa et al. (2011), for particles of 1.5–20 nm count median diameter carrying a single charge, the particle growth rate by coagulation could be increased up to a factor of two. The fraction of charged particles reported in this study is within the range of modeling input in Leppa et al. (2011), whereas this study found higher fractions of particles carrying two or three charges. Thus, a factor of greater than two is expected. It should be noted, coagulation is a complicated dynamic process in which particle number concentration and fractal dimension also play important roles. Coagulation rate also changes with time. A full understanding of the impact of particle charge on coagulation rate is beyond the scope of the current work and deserves future research.

Comparing data collected on the two freeways, we found the number concentration of charged particles remained at the same order of magnitude but the fractions were usually higher on the diesel-vehicle dominated I-710 than on the gasoline-vehicle dominated I-405. Fig. 4 further illustrates this point where the fractions of singly charged particles ranged from 0.06 to 0.09 on the I-405 (Fig. 4a) and from 0.09 to 0.14 on the I-710 (Fig. 4b). The differences between the two freeways were relatively small for particles of 30 and 50 nm and even smaller for particles carrying double or triple charges in these size ranges. On the other hand, at 80 and 100 nm, the fractions of charged particles were significantly higher, two times greater for doubly and triply charged particles on I-710 than I-405. Although the fractions of singly charged particles were not as significant as the fractions of particles with double or triple charges, the singly charged particles also showed higher fractions at 80 and 100 nm on I-710 than I-405. Because heavy duty diesel vehicles are a primary source of high ion concentrations on and near a freeway (Jayaratne et al., 2010), the high diesel vehicle traffic was likely causing the high fractions of charged particles on the I-710 freeway.

3.2. Charged UFPs near freeways

Fig. 5 depicts the fraction of charged particles as a function of downwind distances from the I-405 freeway. Overall, the total fraction of all charged particles reduced greatly (i.e., from 0.17 to 0.10) within the first 10 m downwind of the I-405. It then further decayed gradually toward the background level (0.06) at 100 m. In addition, the fractional decay occurred more rapidly for particles with double or triple charges than those with single charge at increasing downwind distances from the I-405. For instance, within 100 m from the freeway, the fractions of singly charged particles reduced by 47% (i.e., from 0.08 to 0.04). However, the fractions of particles with double or triple charges dramatically decrease by 82% (i.e., from 0.05 to 0.01) and 84% (i.e., from 0.03 to 0.01), respectively. The observed decay is likely due to both atmospheric dilution and charge neutralization from particle collision with other ions (or electrons) or to a less extent with other particles carrying opposite charges.

To further investigate the effects of the number of charges on particle concentration decay downwind from freeways, Fig. 6 compares the decay rates of particles carrying different number of charges with previously published data for total particle number concentration and ion concentration near freeways. The downwind concentration was normalized to on-freeway (i.e., 0 m) concentration for particles carrying single, double, and triple charges, respectively. The decay rates of total particle number concentration (Zhu et al., 2002b) and total cluster ions (Jayaratne et al., 2010) were also plotted for comparison. As shown in Fig. 6, in general, the decay rates of charged particles were between total particle (i.e., decay rate of −0.18) and total cluster ions (i.e., decay rate of −0.80) decay curves, with only one exception of singly charged particles (i.e., decay rate of −0.16). Similar to total particle and total cluster ions near freeways, the decay curves of charged particles also stabilized as moving away from the freeway. The decay rates of the charged particles also depended on the number of charges. Particles with triple charges experienced the highest decay rate (−0.51) and followed by those with double charges (−0.42); whereas, particles carrying single charge decreased moderately (i.e., decay rate of −0.16) within the same distance. Table 1 summarizes the regression data of fractional decay functions presented in Fig. 6.

Although particles are a sink for ionic deposition and in return taking on charges, it is a relatively slow process in comparison with ion-electron collision because the mobility of an ion (or electron) is much faster than that of a particle. Ion (or electron) dissipation occurs primarily through bipolar ion-electron collisions so that the fastest decay is found for total cluster ions. The decay of total particle number concentration is primarily a mechanism of [1)] dilution near freeways with minor effects of coagulation by Brownian diffusion. Intrinsically, any charged UFP decay includes the aforementioned two mechanisms: [1)] dilution with minor coagulation by Brownian diffusion and [2)] neutralization by colliding with other ions (or electrons). Moreover, they could also decay via [3)] particle coagulation enhanced by charges on the particle surface. Thus, the downwind decay function of charged particles represented a combined effect of the aforementioned three mechanisms.

3.3. Effects of charge polarities

Fig. 7 shows typical charged particle size distribution for different electrical mobility diameters with different polarities: positive (Fig. 7a–d) and negative (Fig. 7e–h), 15 m from the I-710 freeway. In general, there were more particles with n positive than n negative charges for studied particle sizes. The differences were more significant for 30 and 50 nm particles (Fig. 7a, b vs. Fig. 7e, f) than 80 and 100 nm particles (Fig. 7c, d vs. Fig. 7g, h). For 30 and

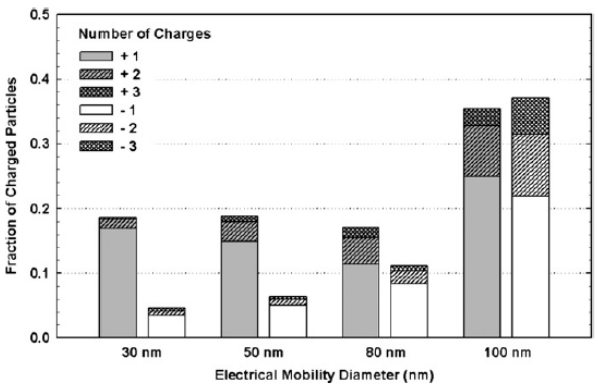


Fig. 8. Fractions of charged particles at four electrical mobility diameters: 30, 50, 80, and 100 nm. The stacked bars represent either positively (gray) or negatively (white) charged particles with different number of charges and polarities (e.g., ±1, ±2, and ±3).

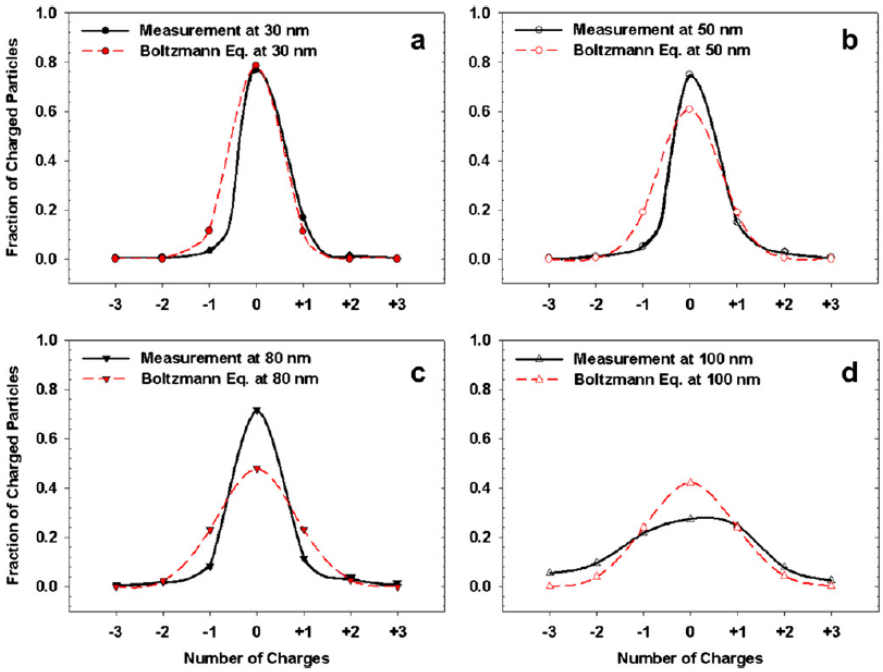


Fig. 9. Measured and Boltzmann equilibrium particle charge distributions at different electrical mobility diameters: (a) 30 nm, (b) 50 nm, (c) 80 nm, and (d) 100 nm. The filled symbols are the averages; note that the uncharged (i.e., $n = 0$) particle fractions were estimated from the measurements of charged particles by subtracting from 1. The dash-lines are the Boltzmann charge equilibrium distributions estimated at temperature of 15 °C for different electrical mobility diameters.

50 nm particles, the number concentrations were much higher for positively than for negatively charged particles (Fig. 7e, f). For larger particles (i.e., 80 and 100 nm), the magnitude of the measured concentrations was similar with minimal differences (Fig. 7c, d, g, h).

Fig. 8 presents the average fractions of particles carrying n charges with respect to different electrical mobility diameters, confirming that these particles, collected near freeways, carried net positive charges. For 30 and 50 nm particles, the total fraction of positively charged could be as high as 0.20 whereas the negatively charged fraction remained less than 0.06. Although different size particles could take different amount of positive vs. negative charges, the differences of the charged fraction with opposite signs were greatly reduced at 100 nm. Net positively charged particles and asymmetric charge distributions have been reported previously in low pressure flames (Wegert et al., 1993). Although Maricq (2008) concluded that charged particles from engine combustion processes followed Boltzmann charge equilibrium showing symmetric charge distributions, a closer examination of the published data suggested net positive charges in somewhat asymmetric distributions. The study also mentioned that steady operation of the engine was required to achieve steady-state Boltzmann equilibrium suggesting unsteady operation may result in unsteady-state charge distributions with net positive charges.

To clarify this, Fig. 9 compares data presented in Fig. 8 to Boltzmann charge equilibrium for different electrical mobility diameters. In general, for 30 nm particles, the magnitude of measured charge distribution agreed with the theoretical equilibrium, but skewed to the right, that is, with more positive charges and less negative charges (Fig. 9a). For 80 and 100 nm particles, we observed more symmetric charge distributions about zero; that is, the fraction of particles with n positive charges equal the fraction with n negative charges. However, the magnitude of measured charge distribution deviated from the Boltzmann equilibrium and the differences increased with increasing particle sizes. This is presumably because the theory assumed that particles were spherical, but larger UFPs tended to be agglomerates having more complex geometries and larger surface areas for potential ion collisions than spherical particles. In addition, the theory assumes steady-state equilibrium but due to the intermittent nature of traffic emissions at the sampling site and short distance to the source, the charged particles might not have reached their steady-state equilibrium. Consequently, nucleation mode particles have a strong tendency of carrying net positive charges at electrical mobility diameter of 30 and 50 nm. The charge distribution became rather symmetric at 80 and 100 nm but had not reached the steady-state or Boltzmann charge equilibrium in the near-freeway environment.

4. Conclusions

A series of field experiments were conducted to quantify the fractions of UFPs carrying n positive or negative charges in on- and near-freeway environments. Using a tandem DMA system, we observed that UFPs took up to three charges on and near freeways. The total fraction of charged particles ranged from 0.12 to 0.32 on the freeways in comparison with less than 0.10 in the background. The total fraction of the charged particles was on the same order of magnitude but higher on the diesel traffic dominated I-710 than the gasoline traffic dominated I-405 across the studied electrical mobility diameters.

Near freeways, the number concentration of charged particle decayed immediately within a short distance (i.e., 10 m) from the freeway and then approached to the background level at ~100 m. The decay rate for charged particles was faster than total particle number concentrations, but slower than total ion concentrations

downwind from the freeway. Among charged particles, the highest decay rate was observed for particles carrying three charges. The near-freeway measurement also found nucleation mode particles (i.e., 30 and 50 nm) had a strong tendency of carrying net positive charges. For 80 and 100 nm particles, we observed more symmetric charge distributions about zero; but the charge distributions had not reached the steady-state or Boltzmann charge equilibrium near freeways.

Acknowledgments

This study complements work in progress partially supported by the National Science Foundation's CAREER Award under contract # 32525-A6010 AI. The authors thank the South Coast Air Quality Management District (AQMD) staff for providing access to the I-710 sampling site. Any opinions, findings, conclusions or recommendations expressed in this report are those of the authors and do not necessarily reflect the views of the National Science Foundation.

References

Andronache, C., 2004. Diffusion and electric charge contributions to below-cloud wet removal of atmospheric ultra-fine aerosol particles. Journal of Aerosol Science 35, 1467–1482.

Arnold, F., Kiendler, A., Wiedemer, V., Aberle, S., Stilp, T., Busen, R., 2000. Chemiion concentration measurements in jet engine exhaust at the ground: Implications for ion chemistry and aerosol formation in the wake of a jet aircraft. Geophysical Research Letters 27, 1723–1726.

Fialkov, A.B., 1997. Investigations on ions in flames. Progress in Energy and Combustion Science 23, 399–528.

Jacobson, M.Z., Seinfeld, J.H., 2004. Evolution of nanoparticle size and mixing state near the point of emission. Atmospheric Environment 38, 1839–1850.

Jayaratne, E.R., Ling, X., Morawska, L., 2010. Ions in motor vehicle exhaust and their dispersion near busy roads. Atmospheric Environment 44, 3644–3650.

Kim, S.H., Woo, K.S., Liu, B.Y.H., Zachariah, M.R., 2005. Method of measuring charge distribution of nanosized aerosols. Journal of Colloid and Interface Science 282, 46–57.

Leppa, J., Anttila, T., Kerminen, V.M., Kulmala, M., Lehtinen, K.E.J., 2011. Atmospheric new particle formation: real and apparent growth of neutral and charged particles. Atmospheric Chemistry and Physics 11, 4939–4955.

Ling, X.A., Jayaratne, R., Morawska, L., 2010. Air ion concentrations in various urban outdoor environments. Atmospheric Environment 44, 2186–2193.

Maricq, M.M., 2006. On the electrical charge of motor vehicle exhaust particles. Journal of Aerosol Science 37, 858–874.

Maricq, M.M., 2008. Thermal equilibration of soot charge distributions by coagulation. Journal of Aerosol Science 39, 141–149.

Shi, Z.B., Shao, L.Y., Jones, T.P., Whittaker, A.G., Lu, S.L., Berube, K.A., He, T., Richards, R.J., 2003. Characterization of airborne individual particles collected in an urban area, a satellite city and a clean air area in Beijing, 2001. Atmospheric Environment 37, 4097–4108.

Tinsley, B.A., Rohrbaugh, R.P., Hei, M., Beard, K.V., 2000. Effects of image charges on the scavenging of aerosol particles by cloud droplets and on droplet charging and possible ice nucleation processes. Journal of the Atmospheric Sciences 57, 2118–2134.

Tripathi, S.N., Harrison, R.G., 2002. Enhancement of contact nucleation by scavenging of charged aerosol particles. Atmospheric Research 62, 57–70.

Wegert, R., Wiese, W., Homann, K.H., 1993. Molecular-beam Wien filter application to the study of charged soot in flames – methodology and mass distributions of particles in butadiene flames. Combustion and Flame 95, 61–75.

Wiedensohler, A., Fissan, H.J., 1991. Bipolar charge-distributions of aerosol-particles in high-purity argon and nitrogen. Aerosol Science and Technology 14, 358–364.

Willeke, K., Baron, P.A., 1993. Aerosol Measurement: Principles, Techniques and Applications. Van Nostrand Reinhold, New York, NY.

Xu, B., Liu, S.S., Zhu, Y.F., 2010. Ultrafine particle penetration through idealized vehicle cracks. Journal of Aerosol Science 41, 859–868.

Yu, F.Q., 2001. Chemiions and nanoparticle formation in diesel engine exhaust. Geophysical Research Letters 28, 4191–4194.

Yu, F.Q., Lanni, T., Frank, B.P., 2004. Measurements of ion concentration in gasoline and diesel engine exhaust. Atmospheric Environment 38, 1417–1423.

Zhu, Y.F., Hinds, W.C., Kim, S., Shen, S., Sioutas, C., 2002a. Study of ultrafine particles near a major highway with heavy-duty diesel traffic. Atmospheric Environment 36, 4323–4335.

Zhu, Y.F., Hinds, W.C., Kim, S., Sioutas, C., 2002b. Concentration and size distribution of ultrafine particles near a major freeway. Journal of the Air and Waste Management Association 52, 1032–1042.

Contents lists available at SciVerse ScienceDirect

Atmospheric Environment

journal homepage: www.elsevier.com/locate/atmosenv

Water-based condensation particle counters comparison near a major freeway with significant heavy-duty diesel traffic

Eon S. Lee [a], Andrea Polidori [b], Michael Koch [b], Philip M. Fine [b], Ahmed Mehadi [c], Donald Hammond [c], Jeffery N. Wright [c], Antonio. H. Miguel [c], Alberto Ayala [c], Yifang Zhu [a,*]

[a] University of California Los Angeles, Los Angeles, CA 90095, USA
[b] South Coast Air Quality Management District, Diamond Bar, CA 91765, USA
[c] California Environmental Protection Agency – Air Resources Board, Monitoring and Laboratory Division, P.O. Box 2815, Sacramento, CA 95812, USA

HIGHLIGHTS

- Three TSI WCPC models (9 units) were compared for one month near a major freeway.
- The 3 models' responses were significantly different under downwind conditions.
- All units showed somewhat size dependency especially for smaller ultrafine particles.
- TSI model 3783 provides relatively consistent data among studied models.

ARTICLE INFO

Article history:
Received 20 April 2012
Received in revised form
28 November 2012
Accepted 3 December 2012

Keywords:
WCPC
Ultrafine particles
Traffic emissions
Freeway

ABSTRACT

This study compares the instrumental performance of three TSI water-based condensation particle counter (WCPC) models measuring particle number concentrations in close proximity (15 m) to a major freeway that has a significant level of heavy-duty diesel traffic. The study focuses on examining instrument biases and performance differences by different WCPC models under realistic field operational conditions. Three TSI models (3781, 3783, and 3785) were operated for one month in triplicate (nine units in total) in parallel with two sets of Scanning Mobility Particle Sizer (SMPS) spectrometers for the concurrent measurement of particle size distributions. Inter-model bias under different wind directions were first evaluated using 1-min raw data. Although all three WCPC models agreed well in upwind conditions (lower particle number concentrations, in the range of 10^3–10^4 particles cm^{-3}), the three models' responses were significantly different under downwind conditions (higher particle number concentrations, above 10^4 particles cm^{-3}). In an effort to increase inter-model linear correlations, we evaluated the results of using longer averaging time intervals. An averaging time of at least 15 min was found to achieve R^2 values of 0.96 or higher when comparing all three models. Similar results were observed for intra-model comparisons for each of the three models. This strong linear relationship helped identify instrument bias related to particle number concentrations and particle size distributions. The TSI 3783 produced the highest particle counts, followed by TSI 3785, which reported 11% lower during downwind conditions than TSI 3783. TSI 3781 recorded particle number concentrations that were 24% lower than those observed by TSI 3783 during downwind condition. We found that TSI 3781 underestimated particles with a count median diameter less than 45 nm. Although the particle size dependency of instrument performance was found the most significant in TSI 3781, both models 3783 and 3785 showed somewhat size dependency. In addition, within each tested WCPC model, one unit was found to count significantly different and be more sensitive to particle size than the other two. Finally, exponential regression analysis was used to numerically quantify instrumental inter-model bias. Correction equations are proposed to adjust the TSI 3781 and 3785 data to the most recent model TSI 3783.

© 2012 Elsevier Ltd. All rights reserved.

* Corresponding author. Tel.: +1 310 825 4324; fax: +1 310 794 2106.
E-mail address: Yifang@ucla.edu (Y. Zhu).

1352-2310/$ – see front matter © 2012 Elsevier Ltd. All rights reserved.
http://dx.doi.org/10.1016/j.atmosenv.2012.12.001

1. Introduction

Ultrafine particles (UFPs, $Dp < 100$ nm) are of a significant health concern. Their small size enables them to penetrate into the pulmonary system at a high deposition rate (Jaques and Kim, 2000), subsequently causing inflammatory responses and chronic cardiovascular diseases (Gilmour et al., 2004). Deleterious health effects from UFPs also include inter-organ translocation, which may potentially impose burdens in the liver, spleen, kidneys, and brain (Donaldson et al., 2002; Kreyling et al., 2002; Oberdorster et al., 2002). Although the degree of the reported particle deposition rates varies, scientists agree that the translocation and deleterious health effects of these particles are primarily due to their chemical composition, small size, high surface area, and high number concentrations.

However, the accurate and precise measurement of UFP number concentration is still a challenge. To overcome this challenge, a fundamental concept of condensation particle counting (CPC) technique was first introduced in the 19th century which then became widely adopted (Aitken, 1890; McMurry, 2000). The CPC approach takes advantage of the heterogeneous particle condensation which promotes the growth of sampled UFPs to micron-sized particles (i.e., a size that can be optically detected by a photodetector) under a controlled super-saturation condition. Therefore, the particle detection efficiency also relies on particle condensation processes in supersaturated working fluid (Stolzenburg and McMurry, 1991). As a result, particle counting efficiency is affected not only by design parameters (e.g., working fluid and temperature between saturator and growth tube) but also by different physico-chemical properties of sample particles (Iida et al., 2009; Kulmala et al., 2007; Petaja et al., 2006).

For a long time, butanol has been used as the working fluid for CPCs. In 2003, TSI introduced the first laminar flow water-based CPC (WCPC), TSI model 3785. Using the laminar flow water condensation methodology (Hering and Stolzenburg, 2005; Hering et al., 2005), this instrument introduced a 1 L min^{-1} sample flow into a wet-walled tube, the second portion of which is heated (TSI, 2003). This creates a region of super-saturation that grows small particles to supermicrometer sized droplets that are counted optically. At low concentrations, the grown particles are counted individually, with a correction for dead time. Above about 3×10^4 cm^{-3}, the WCPC 3785 enters into a photometric mode whereby particle concentration is inferred from the total light scattering from the cloud of droplets within the sensing chamber.

The TSI 3781, introduced in 2005, is a compact unit that has an aerosol flow of 0.12 L min^{-1}, but is otherwise based on the same laminar flow and water condensation technology as TSI 3785, and uses the same operating temperatures. One noted difference is that the 3781 does not have a photometric mode; instead it only uses dead-time corrected single particle counting (TSI, 2005).

The TSI 3783, introduced in 2011, is the first of the next generation of WCPCs. The 3783 uses a new design for the condensation growth tube that improves instrument performance at high particle concentrations and provides consistent lower detectable particle size across all concentrations. The 3783 has the same aerosol flow but different operating temperature, and like the 3781, it does not have a photometric mode, but instead uses dead-time corrected single particle counting throughout its concentration range (TSI, 2011). None of the instruments tested have a sheathed flow.

There is little information available regarding the response differences among different WCPC models, especially in the near-freeway environment. The present study examines and compares the performance (bias, precision, effect of particle number concentration, and particle size) of three different WCPCs, namely TSI models 3781, 3783, and 3785. A detailed investigation on the origin of the observed differences due to instrument design factors is beyond the scope of the current work. A total of nine WCPC units comprising three units of each model were concurrently operated near a major freeway for one month. The most recent TSI model (i.e., TSI 3783) has been promoted as best suited for long-term field operation in both rural and heavily polluted environments (TSI, 2011). An accurate assessment of the performance of this up-to-date model can provide valuable information to assist air monitoring organizations with planning future UFP measurement studies. This intensive WCPC monitoring study was the beginning of an extended monitoring effort ($\sim$6 months) aimed at evaluating TSI 3783 for potential use in a regulatory-like monitoring network.

This paper focuses on intra-model precision and inter-model bias. Since there is no reference instrument for particle number concentrations, bias between instrument units is evaluated in lieu of accuracy. Using the high-resolution data acquired, we evaluated the effects of upwind (low particle concentrations, 10^3–10^4 particle cm^{-3}) and downwind (high particle concentrations, above 10^4 particles cm^{-3}) conditions on WCPC instrument responses in a realistic near-freeway environment and further assessed the effects of particle number concentration and size distribution on intra-model precision and inter-model bias. We also investigated the effect of increasing averaging time intervals so as to increase inter-model correlation. Finally, 3-parameter exponential equations are proposed to provide correction factors to adjust for differences in response between older models (TSI 3781 and 3785) and the most recent model (TSI 3783). Findings regarding the performance and reliability of these three WCPCs and their ability to run unattended for long periods of time will be provided in a subsequent paper.

2. Methodology

2.1. Experimental

2.1.1. Site description

Extensive field measurements were carried out to monitor UFPs near the 710 freeway in Long Beach, California, from May 16th to June 15th, 2011. An *in situ* monitoring trailer equipped with various particle instruments was operated in close proximity to the freeway (15 m from the eastern edge of the 710). The surrounding area was an open flat terrain without a significant source of UFPs other than the traffic emissions from the freeway. The immediate east side of the freeway includes a large flood plain area and the Los Angeles River. The sampling site was located 13 km north of the Long Beach harbor. Therefore, the freeway traffic was the primary source of UFPs at the sampling site. Fig. 1 illustrates the orientation of the freeway and the monitoring station. The 710 freeway generally runs from north to south but the studied section runs 30° to the east. The wind rose chart in Fig. 1 describes the presence of a distinct westerly wind, which is typical for this part of the South Coast Air Basin during this time of the year. In addition to this dominant westerly component, the study period was characterized by the typical afternoon onshore sea-breeze and weaker winds coming from all directions. For the purpose of this study, downwind conditions were defined when the wind direction was about perpendicular to the freeway center-line and at a 300° ± 45° angle. Similarly, upwind conditions referred to time periods when the wind direction was about perpendicular to the 710 center-line but at a 120° ± 45° angle. Upwind and downwind conditions accounted for 14% and 48% of all observed wind directions during the study period, respectively. The remaining 38% of the data were considered under other wind conditions in the analysis.

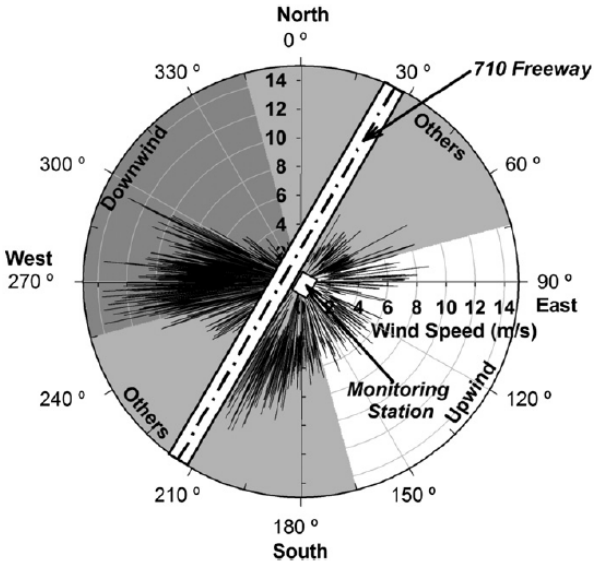


Fig. 1. A schematic of the sampling site including the orientation of the 710 freeway, the monitoring station, wind speed (radial) and wind direction (angular) data during the sampling period, and allocated upwind, downwind, and the other wind directions.

2.1.2. Traffic conditions

Traffic flow data near the sampling site were collected by means of two traffic sensors that are part of the CalTrans Performance Measurement System (PeMS): one for northbound traffic (PeMS ID 717966) and the other for southbound traffic (PeMS ID 717963) (CalTrans, 2010). These sensors were located approximately 600 m and 150 m from the monitoring station, respectively. Fig. 2 presents the overall diurnal traffic pattern changes for weekdays and weekends. The 710 freeway reached up to 1200 vehicles per 5 min around the morning and afternoon rush hours, whereas the minimum traffic volume was 150 vehicles per 5 min overnight. At this site, the 710 freeway traffic includes high heavy-duty diesel truck flow that is approximately 18% of the total daily average.

2.1.3. Sampling and instrumentation

Meteorological parameters were measured by a weather station 10 m above the ground on top of the monitoring trailer. Temperature, humidity, wind direction, and wind speed were recorded at 1-min intervals. At the monitoring site, three units of each of the three WCPC models (3781, 3783, and 3785, TSI Inc., Shoreview, MN) were first synchronized and then set-up to concurrently record UFP concentrations at a 1-min sampling interval. Before doing data analysis, data were checked for alignment. Although all WCPCs have been synchronized, one- to two-minute differences among different units were found and manually corrected for better synchronization. To meet U.S. EPA particulate matter (PM) siting criteria while minimizing particle loss, an air intake manifold supplied the same ambient air sample, which was immediately distributed to each instrument through a series of conductive tubing of the same length (i.e., 1.5 m). All the particle instruments were calibrated by the manufacture prior to deployment and checked for flow and other parameters once every two weeks after deployment.

The manufacture published specifications of the three WCPC models are summarized in Table 1. The three models have a similar detectable particle size range with the same upper limit of 3 μm and lower limits of 5, 6, and 7 nm for models 3785, 3781 and 3783, respectively. Even though maximum detectable particle count

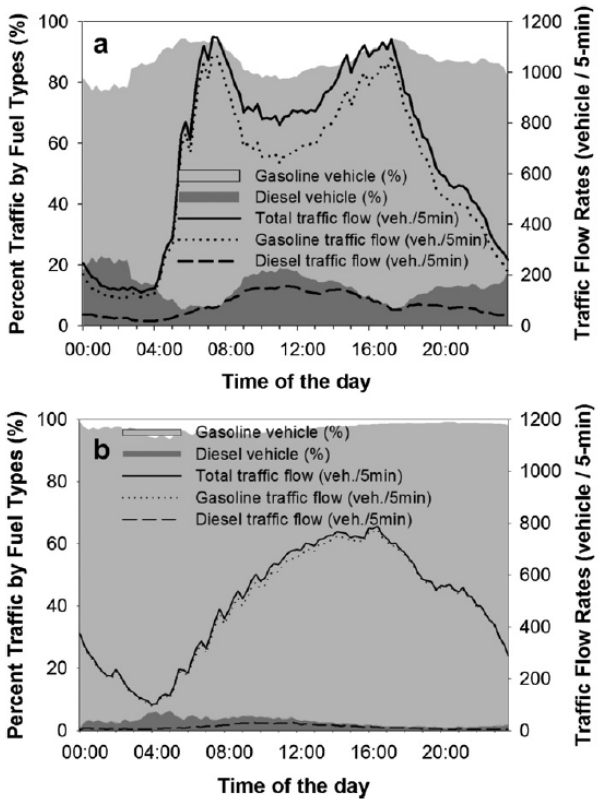


Fig. 2. Comparison of diurnal traffic pattern changes on freeway 710 during (a) weekdays and (b) weekends.

limits vary with different models, the highest particle number concentration measured during this study (approximately 3×10^5 cm^{-3}) was well below any of the highest detectable limits reported by the manufacturer for these three models (see Table 1). It was thus reasonable to expect that the three WCPC models should measure comparable values. However, it should be noted that inlet flow rates are different among the tested WCPCs (see Table 1) which may affect particle diffusion loss in the sampling line. For the average particle size distribution observed in the study, after considering different sampling flow rates, the disparities in diffusion losses to the sampling lines among the tested models were estimated to be less than 5% (i.e., 4.5% between models 3781 and 3783; 2.5% between models 3783 and 3785; and 2.0% between models 3781 and 3785) (Hinds, 1999). These diffusion loss differences were considered negligible and were not accounted for in the following inter- and intra-model comparisons.

Independent from the nine WCPC units, two sets of Scanning Mobility Particle Sizer (SMPS) spectrometers also continually monitored the UFP size distributions from the same sample air flow. The sample aerosols were first classified by particle size with Electrostatic Classifiers (TSI model 3080), and then by two additional WCPCs (TSI models 3785 and 3786) which quantified particle number concentration in each particle size bin. One SMPS was set to measure particles in the size range of 7.6–289 nm with a Long-DMA (TSI model 3081) while the other SMPS was set to measure 2.5–79.1 nm particles with a Nano-DMA (TSI model 3085). A 90-s sampling time and 30-s retrieval time were equally applied to achieve temporally comparable data from the two sets of SMPS systems. The SMPS data were used to better understand the effect

Table 1
Specifications from manufacturer's instrument manuals of the three tested WCPC models (TSI 3781, 3783, and 3785).

Specifications	Model 3781	Model 3783	Model 3785
Year introduced	2005	2011	2003
Single particle counting with dead-time correction	All range	All range	Below 3×10^4 cm^{-3}
Photometric mode	n/a	n/a	Above 3×10^4 cm^{-3}
Detectable particle diameter ranges	6 nm–3 μm	7 nm–3 μm	5 nm–3 μm
Maximum detectable (# cm^{-3}) particle concentrations (cm^{-3})	5×10^5	1×10^6	1×10^7
Particle counting errors	±10% at 5×10^5 cm^{-3}	±10% at 1×10^6 cm^{-3}	±10% at 2×10^4 cm^{-3}
Aerosol flow rates (L min^{-1})	0.12 ± 0.012	0.12 ± 0.012	1.0 ± 0.1
Inlet flow rates (L min^{-1})	0.6 ± 0.12	3 ± 0.3	1.035

of particle size on inter-model precision and intra-model bias as discussed in the result section.

2.2. Analytical

The data analysis focused on quantifying both intra-model precision and potential inter-model biases among three units of different models. The collected 1-min WCPC raw data were first classified with respect to upwind, downwind, and other conditions as illustrated in Fig. 1. The corresponding WCPC data were used to investigate instrument responses under different wind conditions. In an effort to improve inter- and intra-model correlation, we investigated the effect of using longer averaging time intervals (i.e., 5-min and 15-min) regardless of wind directions. It should be noted that only 15-min data resulting from averaging of 15 consecutive 1-min data observations were considered in our analysis. This accounts for more than 99% of the raw data used for analysis. Effects of particle number concentration range and particle count median diameter (CMD) on bias were then investigated. For inter-model comparisons, the 15-min average concentrations from three units of the same model were utilized to represent each model. Biases related to the effect of particle concentration were studied for three particle number concentration ranges: low (10^3–10^4 cm^{-3}), moderate (10^4–10^5 cm^{-3}), and high (10^5–3×10^5 cm^{-3}). Using linear regressions, the coefficient of determination (R^2) of each regression represented data variability in the corresponding concentration range. Furthermore, the investigation of the particle size distribution effects took into account the CMDs from each set of particle size distributions. The particle number concentration data were classified with respect to eight CMD ranges that were selected to include the same number of observations each. The Coefficients of Divergence (COD) was then used to estimate variances of WCPC data between any two compared WCPC models as follows:

$$\mathrm{COD}_{jk} = \sqrt{\frac{1}{n}\sum_{i=1}^{n}\left(\frac{N_{ij}-N_{ik}}{N_{ij}+N_{ik}}\right)^2} \quad (1)$$

where,

COD_{jk}: Coefficients of Divergence between two WCPC models (or units) j and k
n: Total number of observations
i: Individual observation
N: Particle number concentration (cm^{-3})

The COD is a measure of homogeneity between two different WCPC data sets and ranges from 0 (homogeneous) to 1 (heterogeneous). In this study, the COD estimations were repeated for each

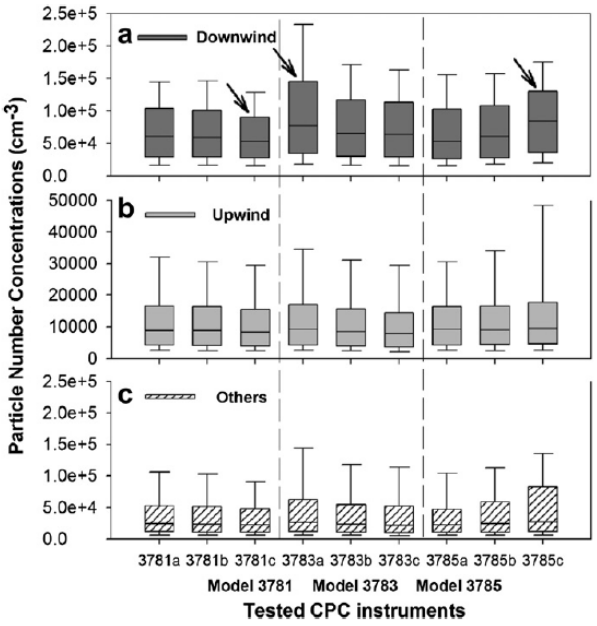


Fig. 3. Comparison among three tested WCPC TSI models (3781, 3783, and 3785) is provided 1-min averaged data for (a) downwind (300° ± 45°), (b) upwind (120° ± 45°), and (c) other wind conditions. Arrows indicate the unit that measured lower (i.e., 3781c) or higher (i.e., 3783a and 3785c) than the other two units of the same model based on visual observations. Under downwind conditions (a), TSI models 3781, 3783, and 3785 showed average concentrations of 69,000 cm^{-3}, 90,000 cm^{-3}, and 80,000 cm^{-3}, respectively.

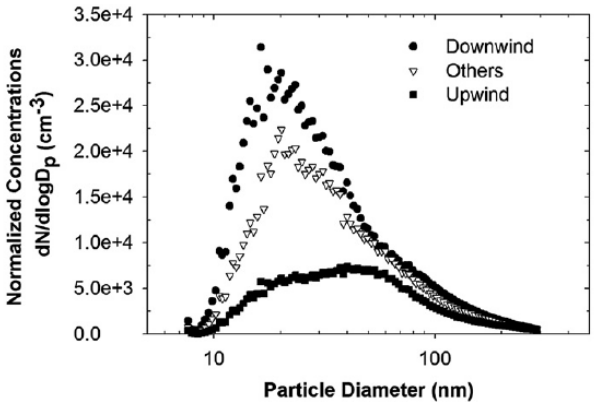


Fig. 4. Comparisons among particle size distributions measured and averaged under different wind directions (i.e., upwind, downwind, and others as depicted in Fig. 1) during the sampling period of one month.

CMD range and each model comparison. The estimated COD data are presented with the average values in each CMD range. Finally, we utilized a 3-parameter exponential regression analysis to numerically quantify potential instrument biases with respect to the observed particle number concentration ranges.

3. Results and discussions

3.1. Inter- and intra-model comparisons under different wind conditions

Fig. 3 shows inter-model biases and intra-model precision using boxplots based on 1-min raw data under different wind directions. Under upwind conditions, all nine units measured an average particle number concentration of approximately 8000 cm^{-3}. However, in downwind conditions one unit for each model provided measurements which, to some extent, were different from those recorded by the other two units of the same model. More specifically, the 3781c underestimated values compared with the other two units of model 3781; the 3783a and 3785c measured higher values than the other two units of the same model. This observation is further discussed in a later section (3.2.3. Effects of particle size distributions). Under other wind conditions (i.e., when the prevailing winds were mostly parallel to the freeway), average particle number concentrations were between the values observed in downwind and upwind conditions. Based on visual

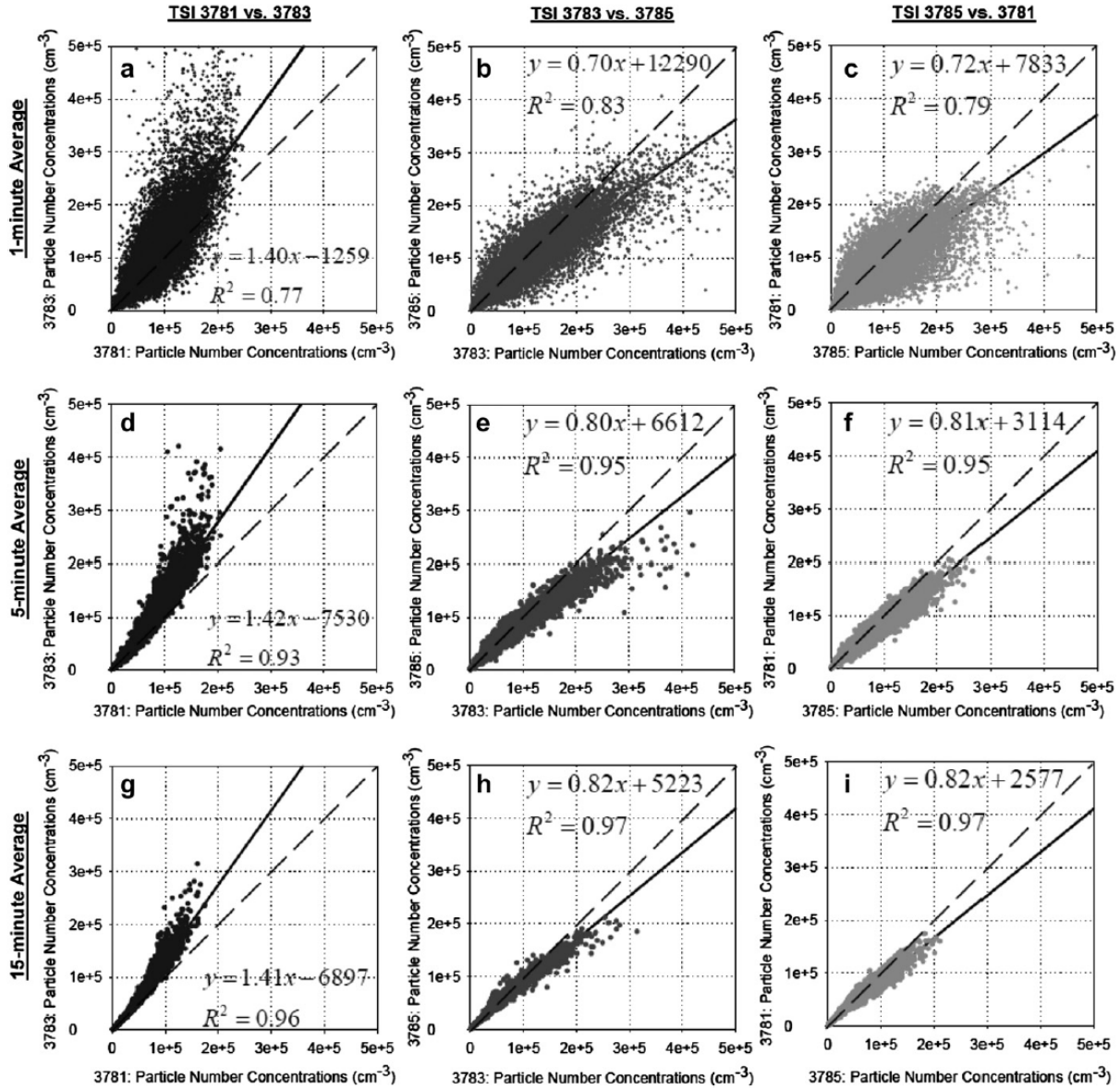


Fig. 5. Instrument response as a function of averaging time periods: 1-min (panels a–c), 5-min (panels d–f), and 15-min (panels g–i). For each panel, both *x* and *y* axis represent particle number concentrations in the range of $0–5 \times 10^5$ cm^{-3}. With increasing averaging time periods (i.e., from top to bottom panels), the variability in the model performances is reduced.

observations, there did not appear to be any inter-model bias under these other wind conditions.

Under downwind conditions the average particle number concentration differed noticeably by different models. Specifically, models 3781, 3783, and 3785 showed average concentrations of 69,000 cm^{-3}, 90,000 cm^{-3}, and 80,000 cm^{-3}, respectively (Fig. 3-a). The largest bias was observed for TSI 3781. It should be noted that the small bias between models 3783 and 3785 was present regardless of wind direction and, thus, for a wide range of particle concentrations. All three TSI 3781 units recorded approximately 26% and 12% lower particle number concentrations than models 3783 and 3785, respectively. The underestimations may have resulted from TSI 3781's poor response to particles with CMD less than 45 nm as discussed in more details later.

To discover the underlying factors causing the observed inter-model biases (Fig. 3), average particle size distributions under upwind, downwind, and other wind conditions were determined (Fig. 4). While there was a predominant mode at 18 nm under downwind conditions, particle number concentrations were more evenly distributed throughout the measured size range under upwind conditions. Although particle size distribution measured under other wind conditions was similar to that under downwind conditions, the magnitude of particle concentration was lower and the size distribution curve lied between downwind and upwind

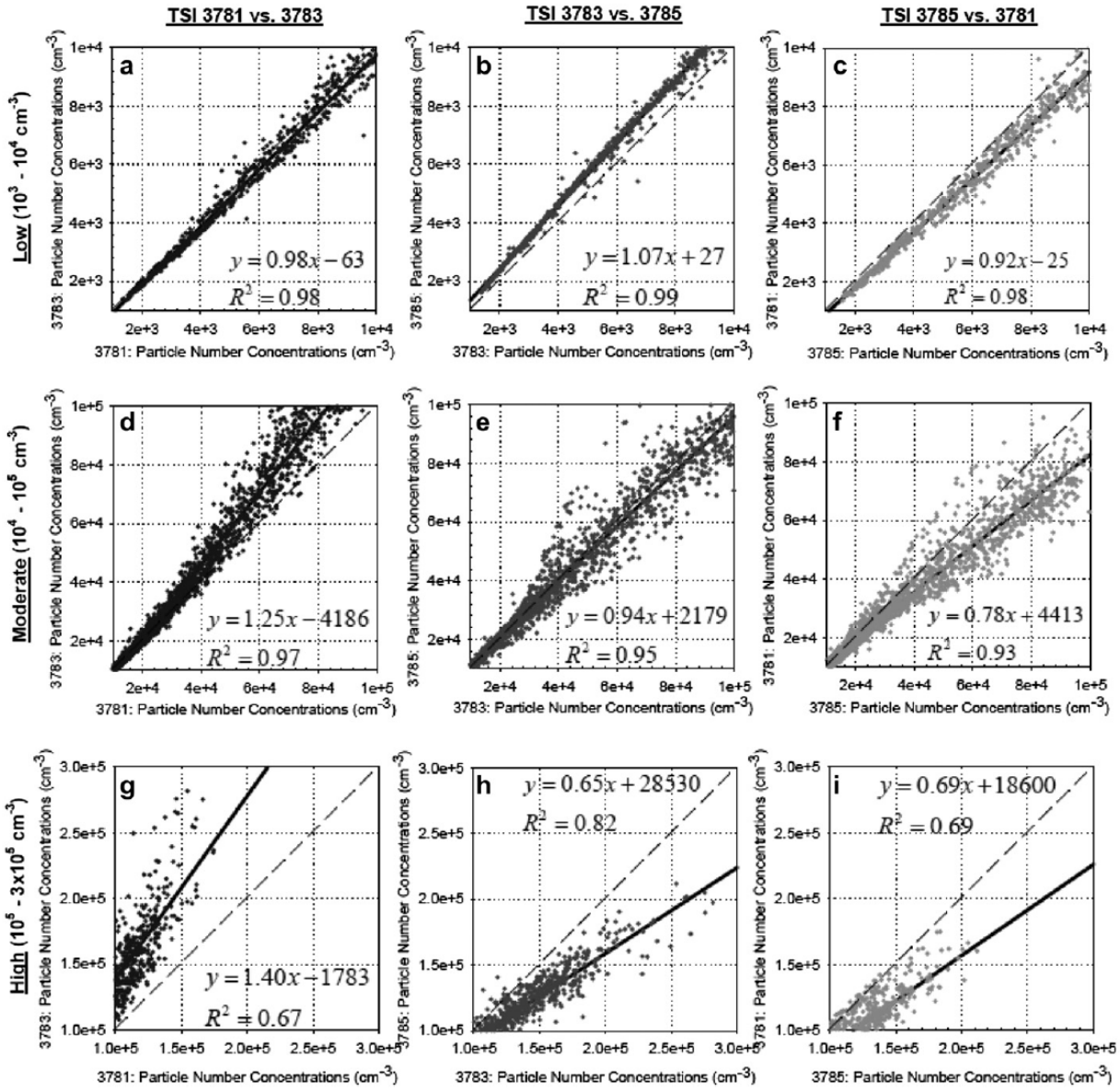


Fig. 6. Instrument response as a function of particle number concentration ranges: low (panels a–c, 10^3–10^4 cm^{-3}), moderate (panels d–f, 10^4–10^5 cm^{-3}), and high (panels g–i, 10^5–3×10^5 cm^{-3}). With increasing source particle number concentrations (i.e., from top to bottom panels), the variability in the model performances also increases to a great extent (15-min averaged data provided).

Table 2
Summary of the linear regression results (i.e., slope (m), intercept (i), coefficient of determination (R^2), and number of observations (n)) of intra-model comparisons by averaging time intervals and concentration ranges. Taking the 15-min averaging for example, we only included data when we had 15 out of the 15 1-min observations. This accounts for more than 99% of our available raw data.

Categories			TSI model 3781			TSI model 3783			TSI model 3785		
			a vs. b	b vs. c	c vs. a	a vs. b	b vs. c	c vs. a	a vs. b	b vs. c	c vs. a
Averaging time	1-min	R^2	**0.89**	**0.79**	**0.91**	**0.74**	**0.98**	**0.73**	**0.83**	**0.83**	**0.94**
		M	0.99	0.75	1.07	0.46	0.94	1.70	0.89	1.05	0.85
		i	−44	7018	2257	21,670	1075	−16,350	5239	9818	−2778
		n	41,848	41,848	41,848	41,847	41,847	41,847	41,848	41,848	41,848
	5-min	R^2	**0.98**	**0.93**	**0.96**	**0.89**	**0.99**	**0.88**	**0.98**	**0.97**	**0.98**
		m	1.02	0.83	1.09	0.58	0.95	1.59	0.97	1.17	0.83
		i	−1291	2987	1137	12,510	229	−10,770	887	3394	−1501
		n	8348	8348	8349	8370	8367	8370	7135	6901	6624
	15-min	R^2	**0.98**	**0.95**	**0.96**	**0.94**	**0.99**	**0.94**	**0.99**	**0.98**	**0.98**
		m	1.02	0.85	1.09	0.64	0.96	1.5	0.97	1.19	0.82
		i	−1110	2389	1018	8758	19	−8515	469	2257	−828
		n	2783	2783	2784	2790	2790	2790	2383	2303	2209
Concentration ranges (15-min)	Low	R^2	**0.97**	**0.96**	**0.99**	**0.99**	**0.99**	**0.99**	**0.99**	**0.97**	**0.98**
		m	0.95	0.95	1.06	0.91	0.93	1.17	0.96	1.09	0.91
		i	44	104	79	23	−1	6	54	17	121
		n	514	1851	418	537	1647	606	407	1263	334
	Moderate	R^2	**0.98**	**0.94**	**0.96**	**0.97**	**0.99**	**0.97**	**0.98**	**0.98**	**0.97**
		m	0.97	0.88	1.10	0.75	0.97	1.35	0.99	1.29	0.74
		i	403	1813	358	4352	−415	−3700	299	−568	2099
		n	514	1851	418	537	1647	606	439	1468	396
	High	R^2	**0.75**	**0.41**	**0.55**	**0.69**	**0.98**	**0.64**	**0.91**	**0.85**	**0.88**
		m	1.04	0.76	0.52	0.33	0.91	2.21	0.88	0.88	1.01
		i	−944	11,270	63,760	69,200	5530	−88,680	13,470	37,270	−22,540
		n	514	1846	417	537	1647	606	402	1388	347

conditions. This agrees well with previous work that documented the same tendency of upwind/downwind particle size distributions near the 710 freeway (Zhu et al., 2002). Thus, the particle number concentration and particle size might play important roles in explaining the observed discrepancies among different WCPC models as discussed in the following sections.

3.2. Factors affecting inter- and intra-model precision and bias

3.2.1. Effects of averaging time intervals

One approach to increasing instrument comparability may be to increase the time-averaging period. Although all measurements aimed to achieve high-resolution (i.e., 1-min) data, interpretation of the data was challenging because of highly variable 1-min responses from the three WCPC models. Increasing averaging time intervals increases instrument precision but information about short-term variability due to sudden increase or decrease in particle number concentration is lost. Although increased averaging-time could not distinctively present abrupt changes in concentration, it may be desirable to achieve appropriate instrument comparisons in a long-term sampling study. The collected 1-min raw data, regardless of wind directions, were then post-processed to produce data with an averaging time of 5 and 15 min(s). With 1-min data, the regression analyses found the lowest R^2 of 0.77 for the comparison between models 3781 and 3783 (Fig. 5-a). Similarly, the R^2 from the other two regressions with 1-min data remained at 0.83 and 0.79 in Fig. 5-b (3783 vs. 3785) and -c (3785 vs. 3781), respectively. The correlation between models 3783 and 3785 was stronger than the other comparisons with model 3781 (i.e., 3781 vs. 3783 and 3785 vs. 3781) for the 1-min data. Thus, it is possible that model 3781 was responsible for the low correlation results shown in Fig. 5-a and -c. The R^2 values increased to 0.93 and higher with 5-min averaging time (Fig. 5-d through -f). With 15-min averaging time interval, all three inter-model comparisons clearly demonstrated correlation among the different models with an R^2 0.96 or above (Fig. 5-g through -i). In the subsequent data analysis, only 15-min averaged data were used.

3.2.2. Effects of particle number concentrations

Fig. 6 illustrates the effect of particle number concentration on the WCPC responses for different models. A slope greater than 1 indicates a positive bias for the instrument along the y-axis, and a slope less than 1 indicates a positive bias for instrument on the x-axis. The intercept also needs to be considered. The confidence of the slope (bias) decreases as R^2 decreases. In particular, inter-model correlations (R^2) were consistently above 0.98 in the low particle concentration range (10^3–10^4 cm^{-3}; Fig. 6-a through -c). However, the R^2 dropped when the particle number concentration ranged between 10^4 and 10^5 cm^{-3} (Fig. 6-d through -f). Finally, all R^2 values decreased further to 0.67 through 0.82 in the concentration range of 10^5–3×10^5 cm^{-3} (Fig. 6-g through -i). Therefore, the variability

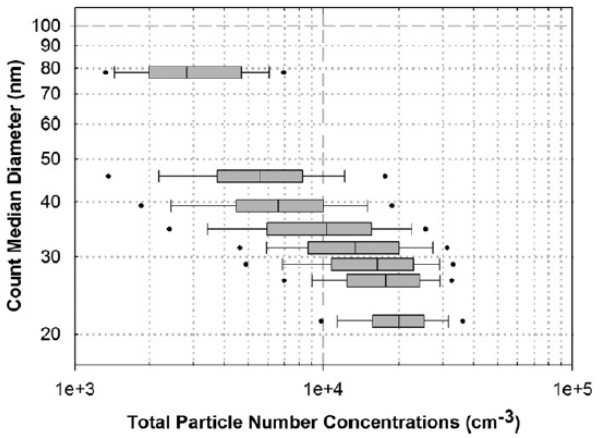


Fig. 7. Relationship between total particle number concentrations and corresponding particle count median diameters (CMD) from measured particle size distributions. The total particle number concentration increases as CMD decreases. Note that the same number of observations is allocated to each box using 15-min average data.

among these WCPC models increases as the particle concentration increases.

As the figures show, the magnitude of the measured concentrations varies by different instrument models and number concentration ranges. It should be noted that model 3781 repeatedly measured the lowest number concentrations for number concentrations above 10^4 cm^{-3}, followed by model 3785. Model 3783 showed higher number concentration readings than the other two models in general. This is not likely due to different detectable particle size ranges by the selected models. For example, Fig. 6 shows model 3783 measured the highest number concentrations in spite that it has a narrower detectable size range than that of the other two models. If detectable particle size ranges were the reason, model 3785 should have measured the highest number concentrations and the lowest number concentration should have been recorded by model 3783 as indicated by the instruments' specifications shown in Table 1. The bias between model 3783 and the other two models also increased as the concentration increased.

Although Fig. 6-h illustrates that model 3783 had the highest variability in particle concentration above 10^5 cm^{-3}, model 3783 responded similarly to model 3785 between 10^4 cm^{-3} and 10^5 cm^{-3} (Fig. 6-e), unlike the other two model comparisons in the same range (Fig. 6-d and -f). For particle concentration ranges below 10^4 cm^{-3}, the overall response of all three models were very similar. Another important observation is that model 3781 did not measure particle count up to the manufacturer-claimed instrument counting limit of 5×10^5 cm^{-3}. As illustrated in Fig. 6-g and -i, model 3781 only measured up to 2×10^5 cm^{-3} while the other two models measured particle number concentrations up to 5×10^5 cm^{-3}. Although our dataset is limited, caution should probably be exercised when using model 3781 near combustion sources where relatively high particle number concentrations is expected.

In addition to inter-model comparisons, Table 2 summarizes linear regression results for correlations between instrument units of the same model, sorted by averaging time and concentration range. Using linear regression, individual instrument units were compared to another unit of the same model. There was strong intra-model variability among all three models indicating individual instrument may perform differently from another unit of the same model. In general, higher R^2 values were observed with increasing averaging time intervals and at lower particle concentrations which corroborates findings in inter-model comparison as shown in Figs. 5 and 6. Conversely, the higher the concentration range, the lower the R^2 values.

3.2.3. Effects of particle size distributions

Differences in inter-model responses were further studied with respect to CMD to assess the impacts of changes in particle size distributions. Fig. 7 illustrates that the total particle number concentration increased when the CMD decreased, especially when the CMDs were between 20 and 30 nm. It should be noted that the same number of observations are presented in each box in Fig. 7. Thus, particle-counting instrument accuracy may be affected to a great extent by particles in this size range which constitute the majority of particles in term of number concentration near roadways.

The observed size-dependent counting efficiency helps to explain the considerable underestimations in particle count measurements for model 3781. Fig. 8 presents COD (Eq. (1)) changes across measured CMD ranges among different tested WCPC models when the particle concentrations are below 1×10^4 cm^{-3} (Fig. 8-a) and above 1×10^4 cm^{-3}. The COD becomes a measure of magnitude of divergence and the gradient of COD value indicates a series of changes in the magnitude of divergence. Fig. 8-a showed CODs were not only comparable (all remained less than 0.01) but also flat across CMDs when particle concentrations are below 1×10^4 cm^{-3}. It suggests that there is hardly any particle size effect on instrument bias in this low particle concentration range. On the other hand, when particle concentrations are above 1×10^4 cm^{-3} (Fig. 8-b), CODs started to diverge when CMDs are less than 45 nm. Models 3783 and 3785 demonstrated consistent performances with a low COD of approximately 0.005. Although there were differences in measurements between models 3783 and 3785 as discussed previously, the magnitude of these differences (i.e., COD) was minimal and consistent throughout all considered CMD ranges. In contrast, the COD between models 3781 and 3783 demonstrated greater divergence when CMDs were less than 45 nm. The divergence significantly increased as the particle CMD decreased. Thereby, the high COD gradient below 45 nm might be due to abrupt changes in performance differences between models 3781 and 3783 for particles with CMD less than 45 nm. When considering that models 3783 and 3785 had comparable performances and model 3783 counted more particles than model 3781, the high COD gradient was likely a consequence of model 3781 under-counting particles smaller than CMD of 45 nm. This is further confirmed by the COD curve from models 3781 and 3785 where the COD also increased below the CMD of 45 nm. In this case, however, the rate of COD changes was lower than the rate of COD changes between models 3781 and 3783. This is presumably because model 3785, in general, counted fewer particles than model 3783. Therefore, the particles with CMD less than 45 nm disrupted model 3781 performance and consequently resulted in underestimation of particle number concentrations as shown in Fig. 3.

For intra-model comparisons, Fig. 9 presents COD changes across measured CMD ranges among the three units of TSI models 3781, 3783, and 3785. As discussed in Section 3.1, units 3781c,

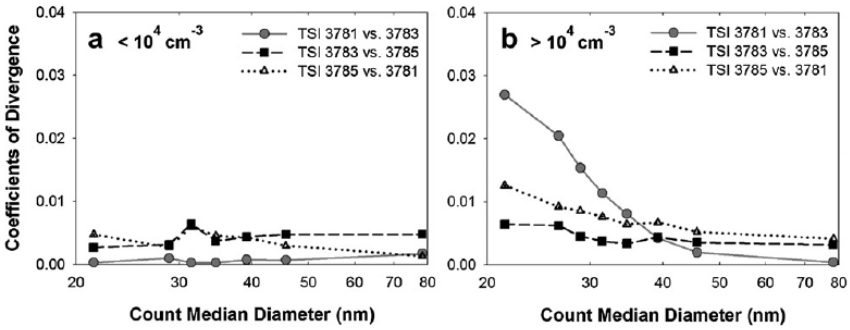


Fig. 8. Inter-model comparisons: the Coefficients of Divergence (CODs) among the three TSI WCPC models are plotted as a function of particle count median diameter (CMD) and particle number concentration ranges: (a) below 10^4 cm^{-3} (i.e., 10^3–10^4 cm^{-3}) and (b) above 10^4 (i.e., 10^4–3×10^5 cm^{-3}).

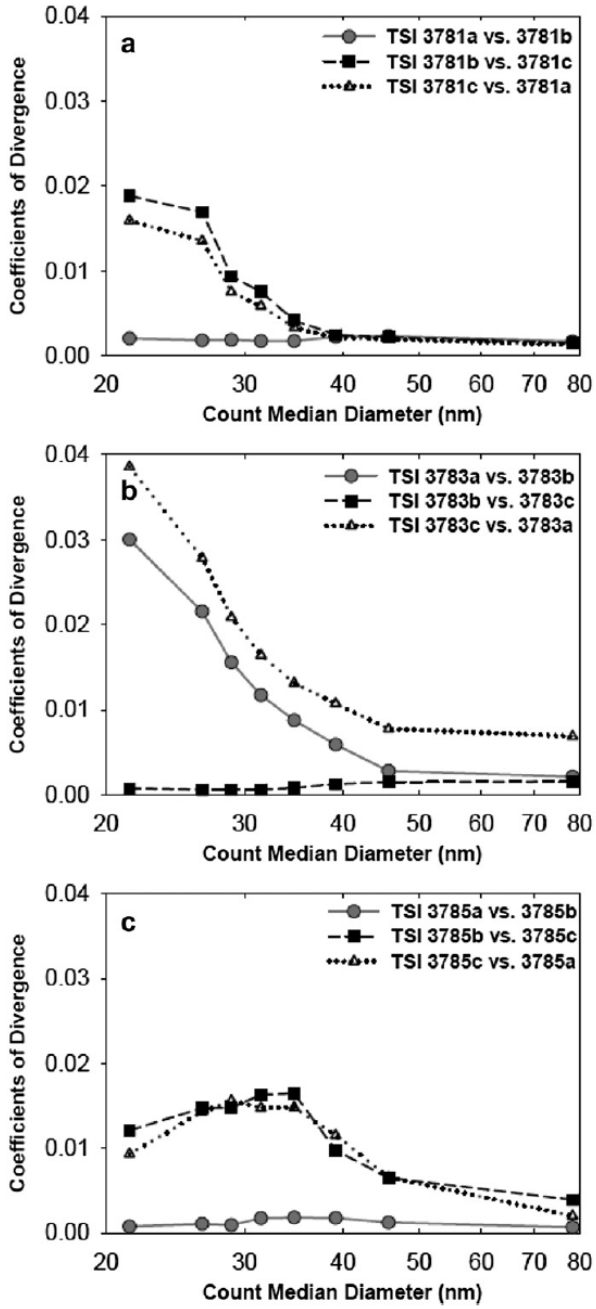


Fig. 9. Intra-model comparisons of the Coefficients of Divergence (CODs) for the three units of TSI WCPC models (a) 3781, (b) 3783, and (c) 3785 are plotted as a function of particle count median diameter (CMD).

3783a, and 3785c measured somewhat higher or lower values than the other two units. This observation is also explained by the data presented in Fig. 9. For example, Fig. 9-b shows that among the three 3783 units, the two high overall CODs were associated with 3783a. This was because concentration readings from instrument 3783a were higher than those from the other two units of the same model. However, the three COD curves are flat over CMD. This pattern is similar to what has been observed in the COD curve for models 3783 and 3785 in Fig. 8. The flat COD curves suggested that CMD changes (i.e., particle size changes) had little impact on model 3783 readings. On the other hand, the cause of intra-model bias for 3781 and 3785 might be different from that of model 3783. Model 3781 presents significant COD increases in CMD less than 45 nm (Fig. 9-a) and model 3785 shows similar trend with less steep gradient of COD curves (Fig. 9-c). Since COD gradient between 3781a and 3781b seems flat and is similar for the case between 3785a and 3785b, the sudden changes in COD seem to be driven by 3781c and 3785c. These observations suggest that particle size may affect particle counting performances not only among different models but also among individual units of the same model. This particle size effect also seems to impact models 3781 and 3785 more dramatically than model 3783 throughout the measured particle size range. Considering that all three instrument units share the similar mechanical design, it is difficult to conclude one direct cause explaining why one instrument from each model behaved differently.

After excluding the data from what we believe to be poorly performed units from each model (i.e., 3781c, 3783a, and 3785c), we repeated the analysis as shown in Fig. 5-g,-h and -i. The magnitude of model differences was reduced by 25% for 3781 and 3783, 9% for 3783 and 3785, and 9% for 3785 and 3781. However, models 3781 and 3785 still measured particle concentrations 16% and 9% lower than model 3783, respectively. Therefore, the observed measurement differences might have been caused by inherent differences in model specific design and/or manufacturing processes which are beyond the scope of current work. For instance, although all three units of model 3783 were directly supplied from the manufacturer, the manufacturer later confirmed presence of problem with the electrical main board of 3783a.

3.3. Correction factors

The current findings lead to the development of post-data correction factors for the older WCPC models (i.e., models 3781 and 3785) to minimize inter-model bias. It should note that currently there is no reference standard instrument for particle number measurement. We chose to fit data to the model 3783 simply because it is the most recently developed TSI WCPC model and data from this study confirmed its superior stability across a wide particle concentration/size range.

In comparison with model 3783 data, the measurement bias of instrument models reached up to approximately 35% for model 3781 and 25% for model 3785 (Fig. 10). Because the theoretical maximum particle diffusion losses in the sampling lines remains less than 5%, the primary cause of model bias is thought to stem from the instrument itself. Therefore, the correction factors were derived from the 3-parameter exponential regression analyses shown in Fig. 10. The correction equations for WCPC models 3781 and 3785 as follows:

$$N_{WCPC3783} = 3.754 \times 10^5 \cdot e^{3.094 \times 10^{-6} \cdot N_{WCPC3781}} - 3.780 \times 10^5 \quad (2)$$

$$N_{WCPC3783} = 3.248 \times 10^5 \cdot e^{2.369 \times 10^{-6} \cdot N_{WCPC3785}} - 3.248 \times 10^5 \quad (3)$$

Eqs. (2) and (3) help minimize the intrinsic discrepancies from using recent WCPC models. The developed equations adjust the number concentration data ($N_{WCPC3781}$ and $N_{WCPC3785}$) collected from the older WCPC models 3781 and 3785 to fit the number concentration data from the most recently developed TSI model,

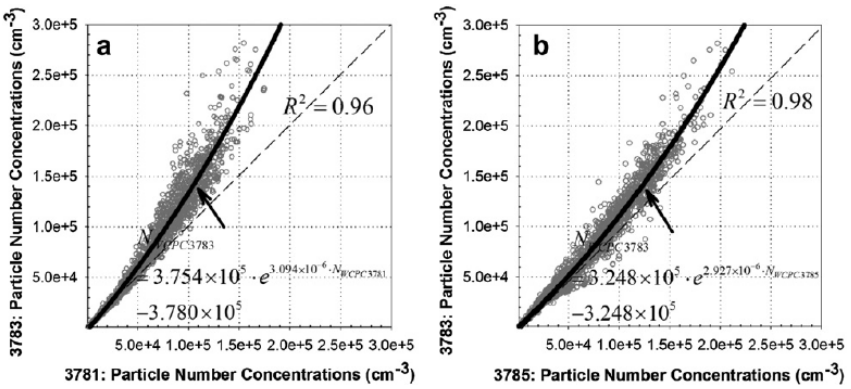


Fig. 10. Comparison between 15-min averaged data collected from TSI WCPC model (a) 3781 and (b) 3785 with model 3783. Solid lines represent 3-parameter exponential correction equations for each model comparison with TSI 3783.

3783 ($N_{WCPC3783}$). The developed correction Eq. (3) results in good data fitting for the one month of data collected in this near-freeway environment. However, it is unknown how well the model would fit under different environments. It should also be noted that Eq. (2) is only applicable for particle number concentrations greater than 1.5×10^4 cm^{-3}. When the particle number concentration is lower than 1.5×10^4 cm^{-3}, the measurements of models 3781 and 3783 match well, and no post-data processing is needed. Eqs. (2) and (3) were derived on the basis that particle number concentration and size distribution are the primary factors affecting WCPC performance. The derived equations may be applicable to other near-freeway environment; however, different near-freeway ambient air might have different site-specific factors such as particle chemical compositions, which this study did not address.

4. Conclusions

Measurements of UFPs were conducted for one month near a major freeway in order to compare the performance of different WCPC instrument units. An evaluation from nine WCPC units of three different models (i.e., TSI 3781, 3783, and 3785) found a certain level of bias between each model, while each unit of the same model resulted in less variability. Despite model differences, all WCPC units responded similarly in low concentration ranges (10^3–10^4 cm^{-3}). However, in high concentration environments which usually occurred under downwind conditions, the variability and bias of each model measurement became larger, with the magnitude of the bias depended on the WCPC model. Specifically, TSI model 3781 consistently recorded the lowest concentrations among the three tested models mainly because of underestimating particles with CMD less than 45 nm. Model 3783 recorded the highest number concentrations, followed by model 3785 for ambient particle number concentrations greater than 10^4 cm^{-3}. The discrepancies between the model 3783 and 3785 measurements were minimal up to a number concentration of 10^5 cm^{-3}, but found higher bias in number concentration above 10^5 cm^{-3}. In an effort to increase the linear relationship, we investigated the effect of using longer averaging time intervals and found that an acceptable data correlation could be achieved using an averaging time of 15 min and above. Based on these one-month data, TSI model 3783, designed for long-term monitoring, provides relatively consistent data with the least sensitivity to particle size among the evaluated models. A long term evaluation of the reliability of TSI 3783 is currently underway and will be discussed in a subsequent paper. To minimize instrumental or model differences, post-data correction equations were proposed to adjust the data from TSI models 3781 and 3785 to model 3783 using 3-parameter exponential models.

Acknowledgments

This study complements work in progress partially supported by the National Science Foundation's CAREER Award under contract # 32525-A6010 AI, and resources from the South Coast Air Quality Management District (AQMD) and the California Air Resources Board (ARB). The authors thank TSI Inc. for providing several WCPC units. The authors also thank AQMD and ARB staff for their assistance with the field measurements. Any opinions, findings, conclusions or recommendations expressed in this report are those of the authors and do not necessarily reflect the views of the National Science Foundation, the AQMD, or the ARB.

References

Aitken, J., 1890. On a simple pocket dust-counter. Proceedings of the Royal Society of Edinburgh 18, 39–53.

CalTrans, 2010. Performance Measurement System (PeMS). California Department of Transportation (CalTrans), Sacramento, CA.

Donaldson, K., Brown, D., Clouter, A., Duffin, R., MacNee, W., Renwick, L., Tran, L., Stone, V., 2002. The pulmonary toxicology of ultrafine particles. Journal of Aerosol Medicine-deposition Clearance and Effects in the Lung 15, 213–220.

Gilmour, P.S., Ziesenis, A., Morrison, E.R., Vickers, M.A., Drost, E.M., Ford, I., Karg, E., Mossa, C., Schroeppel, A., Ferron, G.A., Heyder, J., Greaves, M., MacNee, W., Donaldson, K., 2004. Pulmonary and systemic effects of short-term inhalation exposure to ultrafine carbon black particles. Toxicology and Applied Pharmacology 195, 35–44.

Hering, S.V., Stolzenburg, M.R., 2005. A method for particle size amplification by water condensation in a laminar, thermally diffusive flow. Aerosol Science and Technology 39, 428–436.

Hering, S.V., Stolzenburg, M.R., Quant, F.R., Oberreit, D.R., Keady, P.B., 2005. A laminar-flow, water-based condensation particle counter (WCPC). Aerosol Science and Technology 39, 659–672.

Hinds, W.C., 1999. Aerosol Technology: Properties, Behavior, and Measurement of Airborne Particles, second ed. Wiley, New York.

Iida, K., Stolzenburg, M.R., McMurry, P.H., 2009. Effect of working fluid on sub-2 nm particle detection with a laminar flow ultrafine condensation particle counter. Aerosol Science and Technology 43, 81–96.

Jaques, P.A., Kim, C.S., 2000. Measurement of total lung deposition of inhaled ultrafine particles in healthy men and women. Inhalation Toxicology 12, 715–731.

Kreyling, W.G., Semmler, M., Erbe, F., Mayer, P., Takenaka, S., Schulz, H., Oberdorster, G., Ziesenis, A., 2002. Translocation of ultrafine insoluble iridium particles from lung epithelium to extrapulmonary organs is size dependent but very low. Journal of Toxicology and Environmental Health – Part A 65, 1513–1530.

Kulmala, M., Mordas, G., Petaejae, T., Groenholm, T., Aalto, P.P., Vehkamaeki, H., Hienola, A.I., Herrmann, E., Sipilae, M., Riipinen, I., Manninen, H.E., Haemeri, K., Stratmann, F., Bilde, M., Winkler, P.M., Birmili, W., Wagner, P.E., 2007. The

condensation particle counter battery (CPCB): a new tool to investigate the activation properties of nanoparticles. Journal of Aerosol Science 38, 289–304.
McMurry, P.H., 2000. A review of atmospheric aerosol measurements. Atmospheric Environment 34, 1959–1999.
Oberdorster, G., Sharp, Z., Atudorei, V., Elder, A., Gelein, R., Lunts, A., Kreyling, W., Cox, C., 2002. Extrapulmonary translocation of ultrafine carbon particles following whole-body inhalation exposure of rats. Journal of Toxicology and Environmental Health – Part A 65, 1531–1543.
Petaja, T., Mordas, G., Manninen, H., Aalto, P.P., Hameri, K., Kulmala, M., 2006. Detection efficiency of a water-based TSI condensation particle counter 3785. Aerosol Science and Technology 40, 1090–1097.
Stolzenburg, M.R., McMurry, P.H., 1991. An ultrafine aerosol condensation nucleus counter. Aerosol Science and Technology 14, 48–65.
TSI, 2003. Model 3785 Water-based Condensation Particle Counter: Operation and Service Manual. TSI Inc., Shoreview MN, USA.
TSI, 2005. Model 3781 Water-based Condensation Particle Counter: Operation and Service Manual. Shoreview MN, USA.
TSI, 2011. Model 3783 Water-based Condensation Particle Counter: Operation and Service Manual. TSI Inc., Shoreview MN, USA.
Zhu, Y.F., Hinds, W.C., Kim, S., Shen, S., Sioutas, C., 2002. Study of ultrafine particles near a major highway with heavy-duty diesel traffic. Atmospheric Environment 36, 4323–4335.

Contents lists available at SciVerse ScienceDirect

Atmospheric Environment

journal homepage: www.elsevier.com/locate/atmosenv

Ultrafine particle exposures while walking, cycling, and driving along an urban residential roadway

David C. Quiros [a], Eon S. Lee [b], Rui Wang [c], Yifang Zhu [a,*]

[a] Department of Environmental Health Sciences, Fielding School of Public Health, University of California Los Angeles, Los Angeles, CA 90095-1772, USA
[b] Department of Civil & Environmental Engineering, Henry Samueli School of Engineering and Applied Science, University of California Los Angeles, 405 Hilgard Ave., Los Angeles, CA 90095-1772, USA
[c] Department of Urban Planning, Luskin School of Public Affairs, University of California Los Angeles, Los Angeles, CA 90095-1656, USA

HIGHLIGHTS

- UFP was lower in morning (~60%) and when driving with windows closed (~70%).
- On-roadway $PM_{2.5}$ was substantially lower than the annual NAAQS of 15 μg m^{-3}.
- UFP and $PM_{2.5}$ were similar while walking, cycling, and driving with windows open.
- Respiratory UFP exposure > 7× higher for cycling and walking than driving modes.
- A model showed policy scenarios could reduce background-subtracted UFP by 83%.

ARTICLE INFO

Article history:
Received 1 November 2012
Received in revised form
12 March 2013
Accepted 14 March 2013

Keywords:
Ultrafine particle
$PM_{2.5}$
Exposure science
Cyclist
Pedestrian
Vehicle emissions

ABSTRACT

Elevated concentrations of ultrafine particles (UFPs, <0.1 μm), which have been linked to adverse health effects, are commonly found along roadways. This study reports UFP and $PM_{2.5}$ concentrations and respiratory exposures among four transportation modes on an urban residential street in Santa Monica, California while walking, cycling, and driving with windows open and windows closed (with air recirculation on). Repeated measurements were made for nine days during morning (7:30–9:30), afternoon (12:30–14:30), and evening (17:00–19:00) periods. Median UFP concentrations ranged 1–3 × 10^4 particles cm^{-3}, were 70% lower in afternoon or evening periods compared to the morning, and were 60% lower when driving with windows closed than open. Median $PM_{2.5}$ ranged 2–15 μg m^{-3}, well below the annual National Ambient Air Quality standard of 15 μg m^{-3}. Respiratory UFP exposure (particles inhaled $trip^{-1}$) was ~2 times higher while driving with windows open, ~15 times higher when cycling, and ~30 times higher walking, than driving with windows closed. During one evening session with perpendicular rather than parallel wind conditions, absolute UFP concentration was 80% higher, suggesting influence of off-roadway sources. Under parallel wind conditions, a parameter called emissions-weighted traffic volume, used to account for higher and lower emitting vehicles, was correlated with beach-site-subtracted UFP using second-order polynomial model (R^2 = 0.61). Based on this model, an 83% on-roadway UFP reduction could be achieved by (1) requiring all trucks to meet California 2007 model-year engine standards, (2) reducing light-duty vehicle flows by 25%, and (3) replacing high-emitting light-duty vehicles (pre 1978) with newer 2010 fleet-average vehicles.

© 2013 Elsevier Ltd. All rights reserved.

1. Introduction

Ultrafine particles (UFPs, <0.1 μm) are found in elevated concentrations near roadways with motorized vehicular traffic (Morawska et al., 1999; Westerdahl et al., 2005; Zhu et al., 2002). The average employed Los Angeles County citizen in 2010 spent ~54 min commuting each day (US Census, 2010). Depending on UFP exposure while not commuting, such as occupational and lifestyle exposures, suburban or urban roadway travel could account for 17–50% of daily UFP exposure (Fruin et al., 2008; Wallace and Ott, 2011; Zhu et al., 2007). Exposure to traffic-related UFPs has been shown to be harmful to human health by toxicological and epidemiological studies (Brown et al., 2001;

Abbreviations: PNC, particle number concentration; WCPC, water-based CPC; EUs, emissions units.

* Corresponding author. Tel.: +1 310 825 4324; fax: +1 310 794 2106.
E-mail addresses: Yifang@ucla.edu, yifangzhu06@gmail.com (Y. Zhu).

1352-2310/$ – see front matter © 2013 Elsevier Ltd. All rights reserved.
http://dx.doi.org/10.1016/j.atmosenv.2013.03.027

Strak et al., 2010; Vinzents et al., 2005; Wichmann and Peters, 2000).

Previous studies have quantified UFP concentrations and exposures of street users during active transportation (walking and/or cycling) and motorized transportation. A study in Montreal, Canada found 2.0 times higher particle number concentration (PNC) for motorists than pedestrians, but on separate routes for each mode (Weichenthal et al., 2008). Another similar study in London, England found the average motorist-to-pedestrian UFP ratio, which also used separate routes for the two modes, was 0.7 (Briggs et al., 2008). A study in Copenhagen compared the same urban routes for motorists and pedestrians, and found total particulate matter (PM, total mass with no upper size limit) ratio of motorists to pedestrians was ~2 (Rank et al., 2001). Int Panis et al. (2010) found that for various routes across three Netherlands cities, no differences in UFP, $PM_{2.5}$, or PM_{10} concentrations between driver and cyclist, but reported four times higher respiratory exposure to cyclists from increased particle deposition as a result of elevated breathing rates during exercise (Int Panis et al., 2010). A roadway design study in Portland, Oregon found significantly lower UFP concentrations on the right than left side of parked cars separating motor vehicles from a cycling lane (Kendrick et al., 2011).

These previous studies established ranges of UFP and PM concentrations to which humans are exposed during transportation. They are limited, however, in that they did not control for vehicle ventilation settings that can reduce in-cabin UFP concentrations by up to 85% when recirculation modes were used (Zhu et al., 2007). They are further limited in that transportation modal UFP concentrations were compared across separate routes, or different times of the day, or without comparison of meteorological conditions as in Kendrick et al. (2011). Finally, to the best of our knowledge, no studies have compared air pollutants among transportation modes in the United States.

This study included concurrent measurements of UFP and $PM_{2.5}$ while walking, cycling, and driving. There were nine sampling days between March 22 and April 21, 2011, consisting of measurements in the morning (7:30–9:30), afternoon (12:30–14:30), and evening (17:00–19:00) along a 1-km urban residential roadway, Ocean Park Boulevard, in Santa Monica, CA. The objective of this study is to measure relative concentration and estimate respiratory exposures of UFP and $PM_{2.5}$ among transportation modes. These data can be used to assess the effects of meteorology, roadway design, and mobile source reduction programs on the concentration and respiratory exposure to traffic-related UFPs.

2. Material and methods

2.1. Site location and descriptions

The selected study site was located on Ocean Park Boulevard (Ocean Park) between Neilson Way (Neilson, west boundary) and Lincoln Avenue (Lincoln, east boundary) in Santa Monica, California (Fig. 1). The studied sector of the roadway had a complex terrain with two hills (maximum elevation difference of 20 m) in a length of 1 km. Ocean Park is an arterial residential road, with traffic volume ranging from 900 to 1200 vehicles h^{-1} during the study. The roadway included one lane in each direction, a cycle lane, and an elevated sidewalk for the complete length. The surrounding area consisted mainly of residential houses on both the north and south sides of the roadway; other than emissions from roadways adjacent to Ocean Park, there appear to be no substantial direct PM sources.

The 1-km roadway segment selected for this study enabled repeated measurements to more accurately detect pollutant differences among street users and transportation modes. The authors acknowledge, despite this key advantage, that the segment may not represent a typical street user's daily total on-roadway exposure to UFP and $PM_{2.5}$.

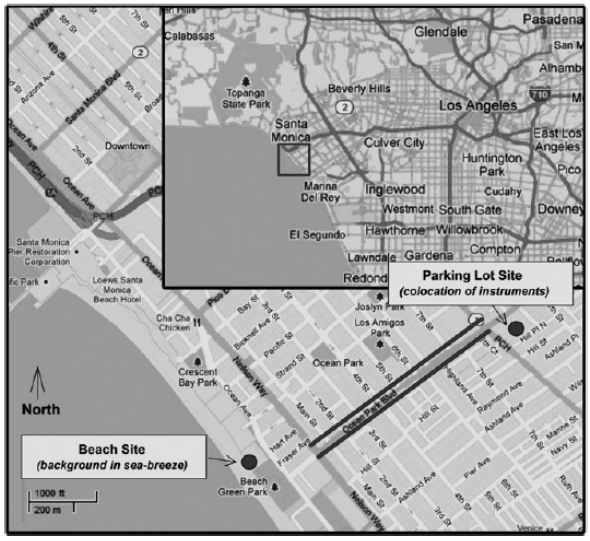


Fig. 1. Area map displaying location of 1-km study site (parallel lines), beach site, and parking lot site.

2.2. Study design

Each of the nine sampling days consisted of three sessions of two-hour continuous sampling in the following periods: morning (7:30 to 9:30), afternoon (12:30 to 14:30), and evening (17:00 to 19:00). In each session, two researchers were sampling in roundtrips along the Ocean Park Blvd (2 km total), one for walking and cycling and the other for driving and beach measurements. Each researcher was carrying one set of instruments to sample UFP, $PM_{2.5}$, and CO_2, as described in Section 2.3 Instrumentation. In each session, two walking trips (one time in each direction), four cycling trips, and six driving trips with windows open, and four driving trips with windows closed were completed. For each driving trip with windows closed, air conditioning recirculation was applied, and two consecutive round-trips were made before opening windows. Measurements while returning the vehicle to the starting location were excluded from analyses. Under typical traffic conditions, driving, cycling, and walking required ~4, ~7 and ~25 min per roundtrip, respectively. Two to three times during each session, ~5 min of measurements took place at the beach site shown in Fig. 1. During sea-breeze conditions (all afternoon and evening sessions except for Thursday evening April 14), this location served as a background monitoring site where no upwind combustion sources were present.

2.3. Instrumentation

UFP, $PM_{2.5}$, and CO_2 sampling instruments were carried in a backpack and by hand for walking modes. For cycling modes, instruments were carried in a backpack and mounted to a seat post-mounted clamp-on rack to a mountain bicycle with low tire pressure (~1.5 bar). A 2002 MY 2-door coupe was used for the driving modes with instruments placed on the passenger seat. Before and after each session, all instruments were synchronized in time, set to record data at 1-s intervals, and collocated for at least five minutes for subsequent data validation at the parking lot site shown in Fig. 1.

We measured PNC from 0.01 to 1.0 μm with a portable condensation particle counter (CPC, TSI model 3007, TSI, Inc., Shoreview, MN,

USA) for walking and cycling. We measured PNC >5 nm with a water-based Condensation Particle Counter WCPC (TSI Model 3785, TSI, Inc., Shoreview, MN, USA) and PNC from 0.02 to 1.0 μm with a P-Trak (TSI model 8525, TSI Inc., Shoreview, MN, USA) for both driving and beach-site measurements. Although UFP refers explicitly to PNC for particles < 100 nm, this term will be applied hereafter in place of PNC for consistent use of terminology. Since near-roadway distributions of PNC are typically >90% within the UFP size range, this terminology is most appropriate for the context of this study.

$PM_{2.5}$ concentrations were measured by two DustTrak units (TSI model 8520, TSI Inc., Shoreview, MN, USA) for all modes. All DustTrak $PM_{2.5}$ data were divided by a factor of 2.4 corresponding to U.S. EPA Federal Reference Method gravimetric values determined by Zhang and Zhu (2010). This conversion factor is within 10% of that reported by a previous study (Yanosky et al., 2002).

CO_2 was measured using two Q-Trak units (TSI model 8554, TSI Inc., Shoreview, USA) for all modes. Elevation, latitude, longitude, speed, and bearing direction were measured by two GPS units (Qstarz model BT-Q1000XT, Qstarz Ltd., Taipei, Taiwan) for all modes. For the first three days of the study (March 22, 24, and 26), the WCPC was not used; instead the CPC 3007 instrument was used for driving and walking modes, and the P-Trak was used for cycling and beach-site measurements. The appropriate corrections were applied to account for instrumental differences, described in the Section 2.5.1.

2.4. Traffic and meteorological data

Video footage was recorded for 5 min each 15 min for the first 90 min of each session. The camera was located on the southeast corner of Ocean Park and Lincoln. Traffic entering and exiting the eastern boundary of the Ocean Park study location was counted and classified by the number of cyclists, pedestrians, and total motorized traffic. Motorized traffic was further classified into the following categories: light-duty vehicles 1978 and after, light-duty vehicles 1977 and before, solid waste collection trucks, class 5 and 6 diesel light-duty trucks, school buses, heavy-duty diesel trucks (class 7 and 8), and public city buses. These classifications were used to calculate emissions-weighted traffic volume (EUs h^{-1}) for each session as described in Section 2.6.

Meteorological data were obtained from a weather station located 7.3 km to the northeast of the study site, operated by the University of California Los Angeles, Department of Atmospheric and Oceanic Sciences. Data presented in this study reflect only those during active measurement periods.

2.5. Analyses

Before statistical analysis, data were plotted in time series and manually analyzed. Due to the nature of performing field measurements, instruments were intermittently malfunctioning (from bumps while cycling from uneven pavement) and recorded data inconsistent with on-roadway distributions. These erroneous data were removed from the dataset.

2.5.1. Instrument validation

Collocation periods, lasting five minutes before and after each sampling session, served to make measurements to relate instrumental readings of UFP, $PM_{2.5}$ and CO_2. Comparative measurements were taken at the parking lot site, shown in Fig. 1, near Lincoln and Ocean Park. All instruments were placed on passenger seat of the vehicle with the doors open for the duration of this five-minute period. The fluctuation of local sources and meteorology provided a wide range of UFP and $PM_{2.5}$ and enabled development of more accurate correlation functions between instruments for all measured ranges.

From the collocation data, all measurements were corrected to readings of instruments used for drive-mode measurements. The UFP concentration from the P-Trak was corrected to WCPC UFP concentration data using a single linear regression from all collocation periods ($\text{P-Trak}_{\text{corrected}} = 1.497{*}\text{P-Trak}_{\text{original}} + 4546$, $R^2 = 0.70$). UFP concentration from the CPC 3007 was corrected to WCPC UFP concentration data using separate regression equations for each period (average $R^2 = 0.48$). It should be noted that measurement bias has been observed not only between handheld and standard-size models (Hämeri et al., 2002), but also among standard-size instruments of the same model (Lee et al., 2013). Stronger correlations were found for $PM_{2.5}$ ($\text{DustTrak}_{\text{corrected}} = 0.91 {*}\text{DustTrak}_{\text{original}} + 1.61$, $R^2 = 0.91$) and CO_2 ($\text{Q-Trak}_{\text{corrected}} = 1.45 {*}\text{Q-Trak}_{\text{original}} - 137$, $R^2 = 0.66$) measurements.

2.5.2. Normality tests

UFP data were log-transformed and tested for normality using a Kolmogorov–Smirnov test for large ($n > 2000$) samples (p-value < 0.01). The results for UFP data are therefore reported as geometric mean with a geometric standard deviation, and resemble a lognormal distribution.

2.5.3. Particle respiratory exposure calculation

UFP and $PM_{2.5}$ respiratory exposures (number or μg inhaled $trip^{-1}$) are functions of arithmetic concentration (concentration $volume^{-1}$) to which the individual is exposed, the length of each trip (time $trip^{-1}$), and gender-average breathing rates available from Hinds (1999): 130, 390, and 580 mL s^{-1} for driving, walking, and cycling modes, respectively. Note that particle respiratory exposure in this study differs from average particle concentration because it includes breathing rates for the average human. Respiratory deposition is not reported because no particle size distribution measurements were included in this study. More specific classifications of breathing rates, accounting for gender, age, and physical condition are important for exposure science and epidemiological studies; however, inclusion of these parameters is beyond the scope of this work.

2.5.4. Beach-site UFP and $PM_{2.5}$

Each five-min beach-site measurement served as a reference for on-roadway UFP and $PM_{2.5}$ measurements. Instances of interference, such as cigarette smoking on the beach were noted in the field log and omitted from the dataset to maintain an accurate reference location. The term beach-site-subtracted UFP refers to on-roadway measurements after subtraction of session-resolved geometric UFP means at the beach site. The rationale for reporting beach-site-subtracted UFP is to differentiate between particles of natural background and anthropogenic (here, motor-vehicle) origin. The "incremental" beach-site-subtracted UFP values are reported throughout this paper.

2.5.5. Spatial UFP profiles

Using longitudinal data from the GPS instruments, data collected while cycling and walking were combined, but segregated by period, and assigned to a location on Ocean Park. Regions near major thoroughfare roadways (Neilson, Main, and Lincoln) were classified as "boundary zones," to ostensibly capture the effects of vehicle idling, acceleration, and pollutants originating from traffic signals. The remaining observations were grouped into 64 evenly-spaced segments of ~13 m each, approximately the width of an intersecting cross street. The influence of roadway grade, the presence of underpasses, and within-route intersections were tested using a multivariable linear regression in

the form UFP = β_1*Grade + β_2*Underpass + β_3*Intersection + Intercept. Roadway grade was calculated as an absolute decimal value (e.g. 0.03 for a 3% grade) and used indicator variables for the presence (=1) or absence (=0) of the underpass beneath 4th Street and intersections. The results of this analysis are reported in Fig. 7 and discussed in Section 3.3.

2.6. Emissions-weighted traffic volume

A novel approach is used to predict pollutant reductions from changes in traffic fleet by accounting for the effects of observed higher and lower-emitting vehicles. Using this approach, 1 emission unit (EU) is defined as the emissions from one fleet average vehicle. Small and Kazimi (1995) estimated the US gasoline fleet average PM_{10} emission factor for 2000 at 10 mg mile^{-1}, but since the on-roadway UFP has decreased by approximately 50% over the past decade (Quiros et al., 2013), the 2011 fleet average is assumed ~5 mg mi^{-1} (8 mg km^{-1}). This value is reasonable considering the maximum PM emissions limit is 10 mg mi^{-1} for most new vehicles, however the exact value is less important than the relative ratios to PM emissions of higher-emitting to fleet-average vehicles. After making total traffic volume counts from recorded video footage, the video was replayed for classification by vehicle type. Literature-derived PM emission factors were applied and the number of EUs was calculated accordingly: light-duty vehicles 1977 and before (50 EUs), solid waste collection trucks (9 EUs), class 5 and 6 light-duty diesel trucks (24 EUs), school buses (26 EUs), class 7 and 8 heavy-duty diesel trucks (39 EUs), and public city buses (6 EUs) (California Air Resources Board, 2002, 2006, 2011; Small and Kazimi, 1995). Categorized video classified vehicle flows were multiplied by the respective EUs to obtain the emissions-weighted traffic volume (EUs h^{-1}). For sessions with a parallel sea breeze (230 ± 15°), emissions-weighted traffic volume was a significant predictor of beach-site-subtracted UFP for the walking mode. Regression results and rationale for methodological selection are found in results and discussion Section 3.4.

3. Results and Discussion

3.1. UFP and $PM_{2.5}$

Fig. 2(a–b) show box and whisker plots of UFP and $PM_{2.5}$ measured for each of the four modes and at the beach site during morning, afternoon, and evening periods. The boxes represent the interquartile range (IQR, 25th to 75th percentile); whiskers indicate one and a half times the IQR; and the "X's" are the 95th percentile extent of the distribution. UFP distributions appear lognormal confirming the result of the normality test (Section 2.5.2). Both UFP and $PM_{2.5}$ were substantially elevated in the morning relative to afternoon and evening periods. This pattern is consistent with previous measurements across the Los Angeles region where higher particle concentrations were observed before the development of the daily sea-breeze under static ground-level mixing conditions (Kim et al., 2002). These concentration data are tabulated in Table 1 alongside respiratory exposure for UFP and $PM_{2.5}$.

As shown in Fig. 2(a) and Table 1, no relevant differences of geometric mean, geometric standard deviation, and 95th percentile extent were observed among cycling, walking, and driving-with-window-open modes. Cycling, walking, and driving-with-windows-open measurements were taken within three lateral meters along the roadway, and all had direct contact to the outside air. Collectively, UFP differed across period and the geometric means for these modes were 3.1, 1.2, and 1.1 × 10^4 particles cm^{-3} for morning, afternoon, and evening respectively. The corresponding

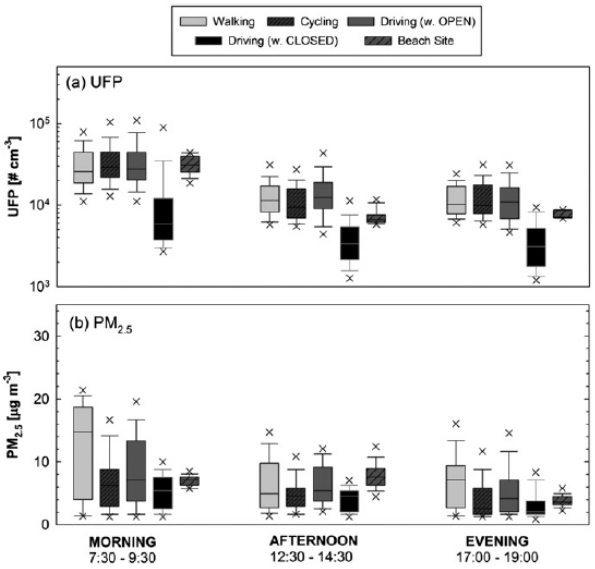


Fig. 2. Boxplots displaying distributions for (a) UFP and (b) $PM_{2.5}$ among each mode and period.

beach-site geometric means were 3.2, 0.8, and 0.9 × 10^4 particles cm^{-3} for these respective periods.

Fig. 2(a) also shows when driving with closed windows and recirculation on, a 75% UFP reduction was observed in the morning, ~40% reductions in the afternoon and evening (geometric means 7.8, 7.2, and 7.7 × 10^3 particles cm^{-3} for morning through evening, respectively). These in-cabin reductions are less substantial than the 85–90% reductions reported in previous Los Angeles vehicle cabin studies with similar vehicle configurations (Zhu et al., 2007). The difference may have been due to the chosen routes, speeds, vehicles tested, and duration of each continuous run with closed windows. Nevertheless, driving with closed windows with recirculation on appears to be an effective technique to mitigate street user exposure on Ocean Park. The build-up of in-cabin CO_2 remained a concern (Zhu et al., 2007) and concentrations > 2000 ppm were found during this study. The National Institute for Occupational Safety and Health designates 1000 ppm as an indoor air quality guideline to limit complaints related to conditions such as headache and fatigue

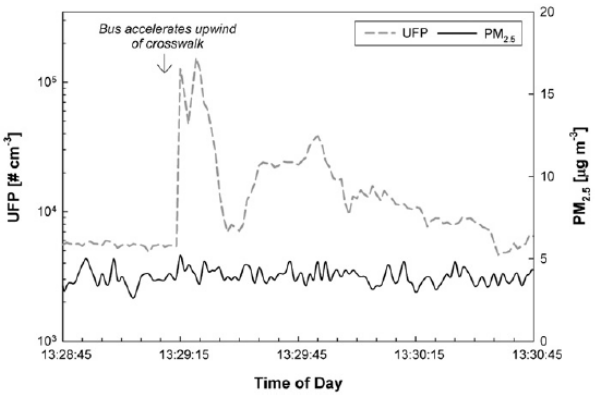


Fig. 3. Time series displaying UFP and $PM_{2.5}$ measurements downwind of an accelerating public bus on Thursday April 14 afternoon.

(NIOSH, 1987). Accordingly, the tradeoff between elevated exposures to in-cabin CO_2 versus UFPs remains a salient issue, but is beyond the scope of this paper.

Fig. 2(b) shows $PM_{2.5}$ concentration while walking had the broadest distribution in terms of IQR and 95th percentile extent of all modes. In addition, walking median $PM_{2.5}$ was higher than other modes in the morning ($\sim$15 versus $\sim$6 μg m^{-3}) and evening ($\sim$8 versus $\sim$4 μg m^{-3}), but not afternoon periods (all modes $\sim$5 μg m^{-3}). When driving with windows closed and recirculation on rather than open windows, $PM_{2.5}$ decreased by $\sim$25%. Beach-site $PM_{2.5}$ during morning and afternoon sessions was $\sim$8 μg m^{-3}, twice the evening value of $\sim$4 μg m^{-3}. Median and mean $PM_{2.5}$ levels for all modes attain the annual National Ambient Air Quality Standards of 15 μg m^{-3}, at the time of this study. However, measurement for regulation requires standardized methods not employed here.

The two right columns of Table 1 show particle number and $PM_{2.5}$ respiratory exposure for a roundtrip (total distance of 2 km) by period and mode. Highest particle number and $PM_{2.5}$ respiratory exposures were for the walking mode (8–21 $\times$ 10^9 particles and 7.7–15.1 μg roundtrip^{-1}), nearly twice the second-highest mode, cycling (4–11 $\times$ 10^9 particles and 3.6–7.0 μg roundtrip^{-1}), fifteen times higher than driving with windows open (4.7–14 $\times$ 10^8 particles and 0.4–0.8 μg roundtrip^{-1}), and thirty times higher than driving with windows closed and recirculation on (1.7–9.0 $\times$ 10^8 particles and 0.2–0.4 μg roundtrip^{-1}). Active transportation modes (cycling and walking) are associated with substantially elevated respiratory exposures to on-roadway pollutant levels than passive modes (driving). Street users while driving can cut in half their particulate respiratory exposure by keeping the windows closed and recirculation on. All street users can reduce particle number and $PM_{2.5}$ respiratory exposure by 25–50% by substituting a morning trip with an afternoon or evening trip.

Fig. 3 illustrates a difference between UFP and $PM_{2.5}$ from a plume of a public city bus fueled by Compressed Natural Gas. The data were measured while walking when the bus accelerated from a complete stop onto the inclined ramp from Ocean Park to the 4th Street. During this isolated incident no other immediate local traffic was present, and the bus was directly upwind (by several meters) of the instruments. There was a dramatic increase in UFP but not $PM_{2.5}$ concentration. The influence of vehicle emissions on $PM_{2.5}$ may be more regional as a result of photochemical formation pathways (Zheng et al., 2002). The influence of secondary formation of PM from mobile-source-emitted constituents is an important, but independent area. The remainder of this paper will characterize on-roadway pollutants with respect to UFP data.

3.2. Meteorology and UFP

This study included a variety of environmental conditions relative to the weather extremes in southern California. The session-average temperature and humidity, defined as the average over each two-hour measurement period, ranged between 10 and 25 °C, and 15 and 95%, respectively. Relative humidity usually was inversely related to temperature. Typically, daily temperature maxima occurred during afternoon and minima during morning and evening sessions. One exception was Thursday April 14, where the highest daily temperature was measured in the evening.

3.2.1. Wind direction and UFP

Fig. 4 is a radial plot of wind velocity for each study session. The location of the points represents the direction from which the wind originated, consistent with standard meteorological practices. The morning wind speed was low (<3 m s^{-1}) and the direction ranged between 60 and 220°. The afternoon wind speed ranged 3–7 m s^{-1} and wind direction was near-parallel ranging between 190 and

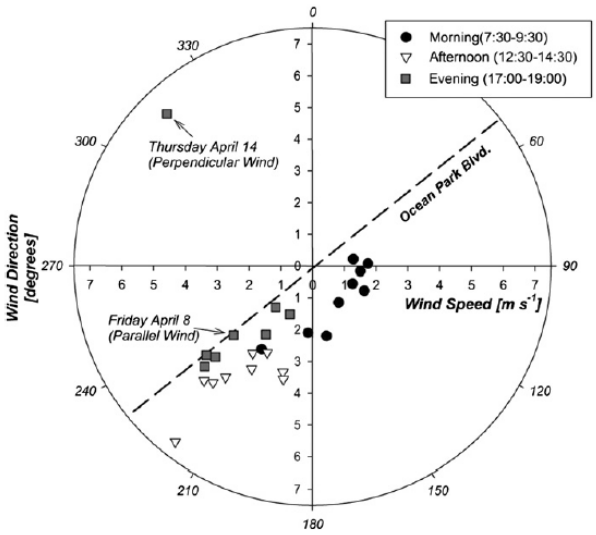


Fig. 4. Average wind velocities for each session grouped by period.

220°. During all but one evening session, wind speed ranged 1–4 m s^{-1}, and wind direction was parallel to Ocean Park ranging between 220 and 230°. On the evening of Thursday April 14, the typical southwesterly parallel wind became a strong northwesterly ($\sim$6 m s^{-1} from 315°). This likely reflects a "Santa Ana Wind" episode, characterized by a warm and dry "land breeze" formed by adiabatic compression of air moving from higher elevations to lower elevations near the coast.

Fig. 5 shows UFP versus time for (a) a typical evening on Friday April 8 with parallel wind (southwesterly) and (b) the evening of Thursday April 14 during the observed perpendicular wind (northwesterly). UFP when driving with windows closed was substantially lower than all other modes and at the beach site. Furthermore, the UFP was appreciably more constant without as many rapid fluctuations observed for modes with direct contact to on-roadway air (driving with windows open, cycling, and walking). These data suggest infiltration of on-roadway UFP is substantially diminished when driving with windows closed and recirculation on, and are consistent with results from Xu and Zhu (2009), which reported delayed and reduced infiltration of UFP into vehicle cabins.

UFP peaks under parallel southwesterly wind conditions (Fig. 5(a)) prevail longer than under perpendicular northwesterly wind conditions (Fig. 5(b)) for all modes with direct contact to outside air. A previous study found the shorter distance along the wind trajectory from the road to the receptor during perpendicular versus parallel winds contributed to the lower UFP concentrations (Molnár et al., 2002). Fig. 5(a) shows during parallel southwesterly wind, incremental values between background and on-roadway minima (defined as the low points between transient UFP spikes) are small and range 1–2 $\times$ 10^3 particles cm^{-3}. This is in contrast to the data measured during perpendicular northwesterly wind as shown in Fig. 5(b), where the same incremental values range 6–9 $\times$ 10^3 particles cm^{-3}. Furthermore beach-site-subtracted UFP and absolute UFP were 25 and 80% higher than parallel wind evenings, respectively.

3.2.2. UFP concentration frequency distributions

Fig. 6 compares frequency distributions of UFP concentrations for cycling and walking modes within each period under consistent wind velocities. Data were sorted into bins of one thousand

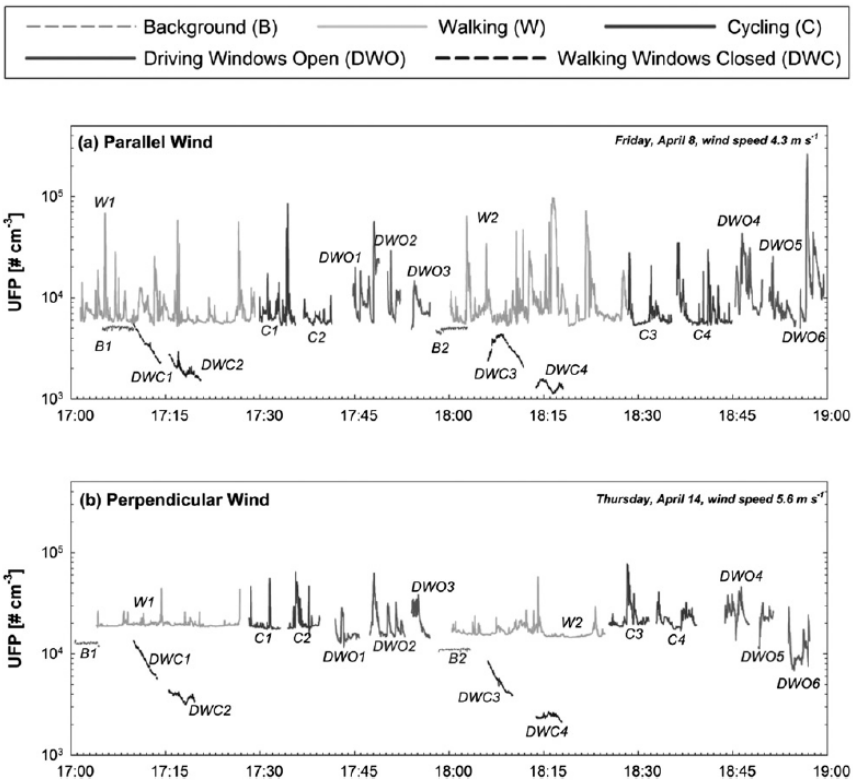


Fig. 5. UFP versus time among for an evening session with (a) a parallel wind direction on Friday April 8, and (b) perpendicular wind direction on Thursday April 14. Continuous line segments on the figure represent one round-trip. Each trip is labeled with a mode abbreviation followed by a trial number. Mode abbreviation *B* stands for beach site, *W* for walking, *C* for cycling, *DWC* for driving with windows closed (and recirculation on), and *DWO* for driving with windows open (e.g. *DWO3* represents the third run of the session for driving with windows open).

particles cm^{-3} (i.e. $2–3 \times 10^3$, $3–4 \times 10^3$ particles cm^{-3}, etc.) and are plotted on the *x*-axis as a function of beach-site-subtracted UFP. This figure compares relative distributions of sessions in order to better identify the sources of observed UFPs on Ocean Park.

The morning UFP distribution, shown by the black solid line, had the most constant frequency distribution for beach-site-subtracted-UFP bins between -5×10^3 and 1.5×10^4 particles cm^{-3}. During the breakup of the nocturnal surface inversion layer, wind speeds were low (Fig. 4), which may have subjected the beach site to inland combustion sources and roadway emissions were likely diluted less quickly. The afternoon and evening parallel-wind UFP distributions, both had beach-site-subtracted-UFP modes between -1 and 2×10^3 particles cm^{-3}. The parallel-wind evening mode was greater compared to the afternoon mode (~15% versus

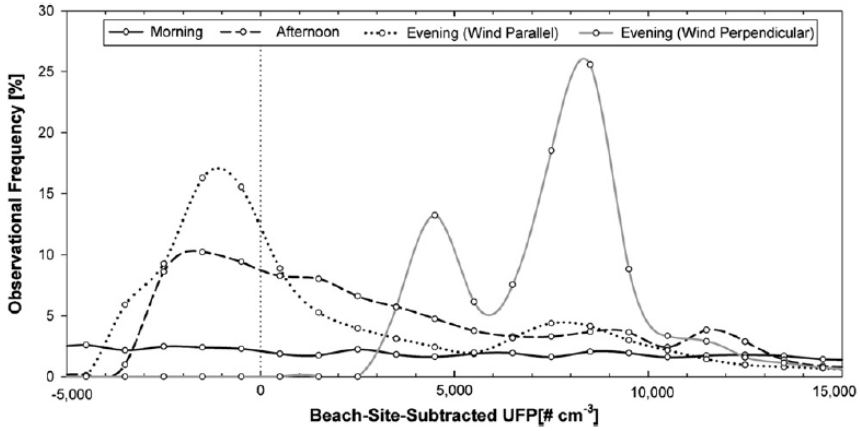


Fig. 6. UFP frequency distributions as a function of beach-site-subtracted UFP during morning, afternoon, evening (wind parallel), and evening (wind perpendicular) sessions. White circles denote the midpoint of beach-site-subtracted UFP bins of one thousand particles cm^{-3}.

10% observation frequencies, respectively). The negative mode values suggest that on-roadway minima were lower than the geometric mean of the beach-site UFP, possibly due to external influences such as cigarette smoke at the beach site not flagged in the field log. Afternoon and evening UFP frequency distributions both appear lognormal, with the majority of the positive values between 0 and 15,000 particles cm^{-3}. The morning UFP frequency distribution is also lognormal, as shown in Fig. 2, but not easily deduced from Fig. 6 because the *x*-axis only extends to 15,000 particles cm^{-3}.

The evening beach-site-subtracted-UFP distributions measured under perpendicular-wind show two distinct modes at $4-5 \times 10^3$ and $8-9 \times 10^3$ particles cm^{-3}. These peaks account for 86% of the total observed UFP frequency, with 14% of observations $>10^4$ particles cm^{-3}. The UFP time series in Fig. 5(b) shows baseline minima values are notably more frequent than transient UFP concentrations. Accordingly, the two distinct UFP frequency distribution peaks consisting of 86% UFP distributions likely correspond to off-roadway rather than transient UFP peaks from on-roadway sources.

These off-roadway sources also appear to affect beach-site UFP, which was also elevated in the perpendicular-wind evening (11,500 particles cm^{-3}) relative to the evening-study average (6100 particles cm^{-3}). Major upwind sources during this wind condition include Pico Boulevard (850 m) and the I-10 Freeway (1230 m). Previous studies of major traffic emissions sources in this region have shown little influence beyond 300 m downwind during daytime conditions (Zhu et al., 2002). Off-roadway emissions transported perpendicular to Ocean Park from the major cross street (Main) and at boundary intersections (Neilson and Lincoln) is another possibility; however Fig. 5(b) does not show patterns of UFP increases among runs (e.g. W1-W2 or C1-C4) that could reflect off-roadway contributions measured at intersections of main cross streets.

Overall, the evening with a dominant northwesterly perpendicular wind was the only instance where the UFP frequency distribution completely greater than the beach-site UFP. These results indicate perpendicular wind, depending on upwind sources, can contribute to greater beach-site-subtracted and absolute UFP. In addition, this discussion highlights the challenge and importance of identifying a suitable background monitoring location for air quality studies.

3.3. On-roadway UFP by location

Fig. 7 displays UFP as a function of location within the study site. Spatial heterogeneity was greatest during morning; the range of segment-average UFP concentration was larger in the morning (~15,000 particles cm^{-3}) than during the afternoon or evenings (~6000 particles cm^{-3}). Higher wind speeds during afternoons and evenings (Fig. 4) may have transported the pollutants more rapidly from emission locations. Alternatively, a higher proportion of recently cold-started vehicles may have been on the roadways in the morning relative to the afternoon or evening periods. Moreover, UFP peaks were measured during all three periods near the underpass at 4th Street (between 0.3 and 0.4 km) and on either side of the hill centered at Highland Avenue (~0.65 and ~0.8 km). The lowest concentrations for all periods were observed between 2nd and 4th streets (~0.2 km).

Roadway grade was significant for daily average ($\beta_1 = 134$ particles cm^{-3} grade-percent^{-1}, p-value = 0.007) and morning ($\beta_1 = 430$ particles cm^{-3} grade-percent^{-1}, p-value 0.001) datasets. These observations are consistent with previous studies that found an increase in hydrocarbon emissions with increased roadway grade (Cicero-Fernândez et al., 1997; Pierson et al., 1996). There were no statistically significant UFP concentration increases in the underpass or at intersections including at the traffic signal located at 6th Street. Boundary zones were generally lower than within-roadway UFP, except for evening period when UFP was ~3000 particles cm^{-3} higher within proximity to Lincoln. Although roadway grade predictor coefficients were significant, they don't fully explain UFP concentrations (multivariate $R^2 \approx 0.2$), and are not very practical to change for mitigating on-roadway UFP exposures.

3.4. Traffic volume and UFP

Fig. 8 shows traffic volume by period, grouped by weekends and weekdays. Fig. 8(a) shows total motorized traffic volume (including public city buses) and emissions-weighted traffic volume (Section 2.6). Fig. 8(b) shows traffic volumes for pedestrians, cyclists, and public city buses on a different *y*-axis scale. Upward gray error bars indicate one standard deviation of observed variance of five-minute observations. Downward error bars were omitted for visual clarity.

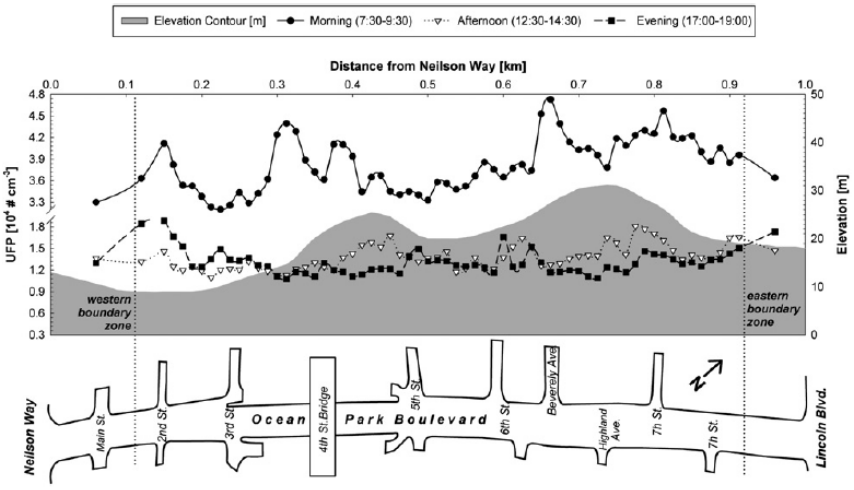


Fig. 7. UFP as a function of location on Ocean Park Boulevard. Data used were from walking and cycling modes combined, from all sessions available for each period in the legend.

Table 1
UFP and $PM_{2.5}$ concentration and respiratory exposures categorized by mode and period. The units for each category as specified under each column heading. GSD denotes geometric standard deviation; SD denotes one arithmetic standard deviation.

	UFP		$PM_{2.5}$	
	Average concentration geometric mean (GSD) [# cm^{-3}]	Respiratory exposure arithmetic mean ± SD [# inhaled $trip^{-1}$]	Average concentration arithmetic mean ± SD [μg m^{-3}]	Respiratory exposure arithmetic mean ± SD [μg inhaled $trip^{-1}$]
Walking, 25 min $trip^{-1}$				
Morning	2.84×10^4 (1.83)	$2.15 \pm 1.04 \times 10^{10}$	11.0 ± 6.6	15.1 ± 9.0
Afternoon	1.27×10^4 (1.73)	$8.60 \pm 2.72 \times 10^9$	6.58 ± 4.27	9.27 + 5.59
Evening	1.16×10^4 (1.64)	$7.83 \pm 2.60 \times 10^9$	5.57 ± 4.98	7.67 + 6.12
Cycling, 7 min $trip^{-1}$				
Morning	3.18×10^4 (1.85)	$1.08 \pm 0.54 \times 10^{10}$	10.5 ± 7.3	6.95 ± 3.79
Afternoon	1.06×10^4 (1.77)	$4.13 \pm 1.93 \times 10^9$	7.11 ± 4.31	4.56 ± 3.27
Evening	1.32×10^4 (1.98)	$4.59 \pm 2.13 \times 10^9$	5.24 ± 4.00	3.61 ± 2.64
Driving with windows OPEN, 4 min $trip^{-1}$				
Morning	3.15×10^4 (1.95)	$1.39 \pm 1.00 \times 10^9$	8.65 ± 8.00	0.74 ± 0.50
Afternoon	1.32×10^4 (1.98)	$5.98 \pm 3.34 \times 10^8$	6.47 ± 3.38	0.56 ± 0.35
Evening	1.11×10^4 (1.85)	$4.73 \pm 2.30 \times 10^8$	5.20 ± 4.28	0.44 ± 0.35
Driving with windows CLOSED, 4 min $trip^{-1}$				
Morning	7.83×10^3 (2.73)	$8.99 \pm 1.18 \times 10^8$	5.23 ± 2.96	0.44 ± 0.23
Afternoon	3.50×10^3 (1.97)	$2.18 \pm 2.04 \times 10^8$	4.15 ± 1.82	0.35 ± 0.13
Evening	3.12×10^3 (1.94)	$1.70 \pm 0.92 \times 10^8$	2.86 ± 2.29	0.25 ± 0.21

Motorized traffic was the lowest in the morning both on weekdays and weekends (~1110 and ~430 vehicles h^{-1}, respectively), peaking evenings on weekdays (~1400 vehicles h^{-1}) and afternoons on weekends (~1210 vehicles h^{-1}). Pedestrian and cyclist activity closely followed these trends; weekday and weekend flows ranged 50–60 and 20–50 pedestrians h^{-1}, and 10–20 h^{-1} and 10–30 cyclists h^{-1}, respectively. Public city bus flows were the highest in the morning at ~13 and ~6 buses h^{-1} weekdays and weekends respectively, and gradually decreased respectively by one half by the evening periods. Pedestrians, cyclists, and public city accounted for 3%, 2%, and 1%, of motorized traffic volume.

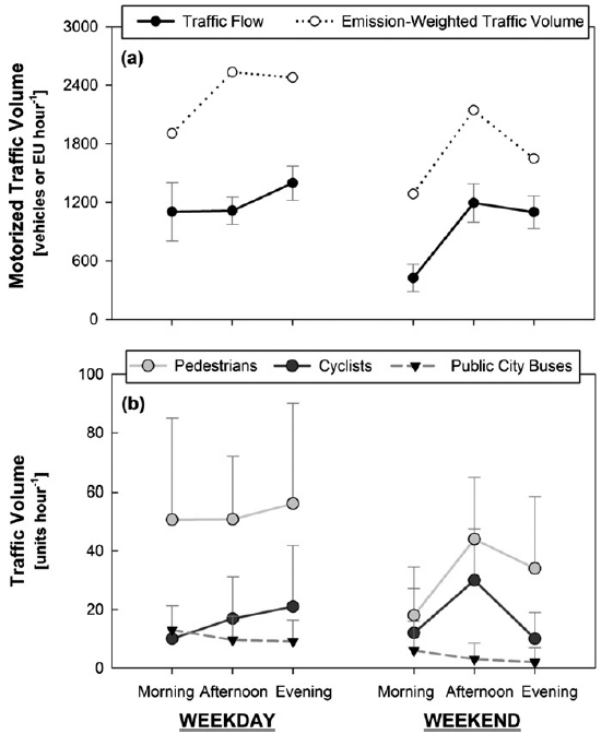


Fig. 8. (a) Total motorized traffic and emissions-weighted traffic volumes, and (b) pedestrian, cyclist, and public city bus traffic volumes, segregated by weekday versus weekend, and sampling period. Total motorized traffic includes public city buses. For measured data only (all data shown except emissions-weighted traffic volume) error bars are displayed, and show one standard deviation of observed variance of five-minute observations.

Fig. 8(a) also shows morning through evening average emissions-weighted traffic volumes were 1,910, 2,540, and 2480 EU h^{-1} on weekdays and 1,290, 2,150, and 1650 EU h^{-1} on weekend days, respectively. The ratios of emissions-weighted traffic volume to motorized traffic volume were 1.6, 2.1, and 2.1 EUs $vehicle^{-1}$ on weekdays and 2.8, 1.7, and 1.4 EUs $vehicle^{-1}$ on weekends. These ratios indicate motorized traffic fleet emissions differed quite significantly among these time periods.

3.4.1. Emissions-weighted traffic volume

Fig. 9 shows emissions-weighted traffic volume versus beach-site-subtracted UFP measured walking for parallel sea-breeze conditions (230 ± 15°). These criteria were met during six evening and five afternoon periods, each represented by a data point in the figure. A second-order polynomial relationship was found between beach-site-subtracted UFP while walking and emissions-weighted traffic volume ($R^2 = 0.61$). The curve is forced through the origin (point shown is not a data point) since on-roadway minima are typically equal or even less than beach-site UFP during parallel wind conditions (Fig. 6).

No relationship with beach-site-subtracted $PM_{2.5}$ was found with emissions-weighted traffic volume, consistent with the relationship presented in Fig. 3. However, gravimetric emissions factors were used to calculate emissions-weighted traffic volume for the three following reasons. First, tailpipe emission factors for particle numbers from individual vehicles have not been established. On-roadway tunnel studies (Geller et al., 2005; Kirchstetter et al., 1999) have defined number-based emission factors for broad vehicle classifications (i.e. gasoline and diesel). Moreover, these factors were estimated by fuel-efficiency generalizations and source apportionment assumptions. Second, dynamometer studies measuring tailpipe emission number vary greatly by protocol, have cycle-to-cycle variability, and are confined to laboratory settings with filtered dilution air (Dwyer et al., 2010). Third, a zero-emissions mobile platform following high-emitting light-duty and heavy-duty vehicles in the Los Angeles region found a moderate Spearman rank correlation ($r = 0.41$) between UFP number and $PM_{2.5}$ mass concentrations (Park et al., 2011).

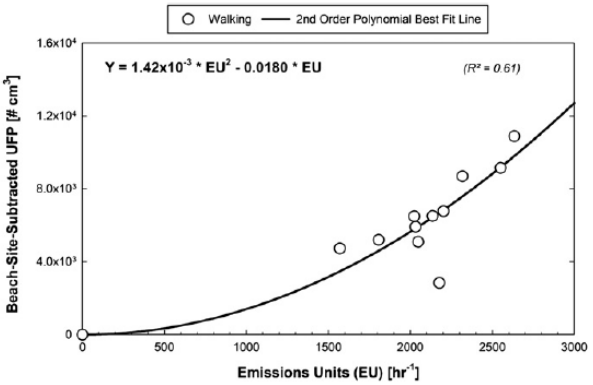


Fig. 9. Second order polynomial regression between beach-site-subtracted UFP while walking versus emissions-weighted traffic volume (EUs h^{-1}) for sessions with parallel wind.

3.4.2. Modeled emission reduction scenarios

For the *ad hoc* purpose of selecting emissions-weighted traffic volume reduction scenarios, we assume light-duty vehicles are for "personal" use (i.e. work, leisure, etc.) and have some degree of trip optionality and mode flexibility. This flexibility could mean greater use of public transit, cycling or walking, or carpooling options. This is in contrast to "service vehicles" (trucks and public buses), which are assumed more necessary to serve the fundamental role of public transportation and goods movement within the community.

If personal vehicle flow were to be reduced by 25%, where personal vehicles are all motorized light-duty vehicles (including high-emitting light-duty) but not trucks or buses, then weekday average emissions-weighted traffic volume would decrease from 2160 to 1730 EUs h^{-1}, and beach-site-subtracted UFP by 36% (CI: 11–61%). This one-quarter reduction of personal vehicles is plausible through increased ridership of public transportation, or adoption of alternative transportation modes including cycling and walking. If the remaining 75% of the high-emitting light-duty fleet were substituted with fleet average light-duty vehicles (5 mg mi^{-1}, 1 EU), weekday average emissions-weighted traffic volume would decrease further to 1230 EUs h^{-1} and beach-site subtracted UFP in total would be reduced by 68% (CI: >36%). This scenario will likely result as the older vehicles in the fleet age and newer low-emitting vehicles are registered. If we assume no change to personal vehicles, but all service vehicles (i.e. light- and heavy-duty trucks, school buses, public buses, etc.) met the California MY 2007 emission standards (10 mg brake-horsewpower-h^{-1}, ~2 EUs), weekday average emissions-weighted traffic volume would decrease to 1790 EU and beach-site-subtracted UFP would decrease by 31% (CI: 9–53%). Combining both described reduction scenarios for "personal" and "service" vehicles, predicted emissions would equal 890 EUs h^{-1}, translating into a 83% decrease (CI: >53%) in beach-site-subtracted UFP.

This approach to estimate UFP reductions is novel but approximate and is limited in the following ways. First, a meaningful relationship was only found from walking data. This may be attributed to the greater number of data points in each session (Table 1), thereby sampling emissions from a greater proportion of vehicles classified by video at the intersection of Ocean Park and Lincoln. Second, an element of bias was introduced when classifying vehicles. Whereas some classifications are simple (e.g. public city buses and refuse trucks), accurate classification was not always possible among other vehicles (e.g. pre-1978 and post-1977 light-duty vehicles). Third, the relationship was only established under parallel wind conditions, hypothetically from isolation of emissions within the roadway environment, which is consistent with previous discussion of wind direction (Section 3.2.1). Finally, the regression does not have constant variance; the majority of the emissions-weighted traffic volume values fall between 1230 and 2500 EUs h^{-1}. Since the reduction scenarios calculate emissions-weighted traffic volume to values < 1230 EUs h^{-1}, the beach-site-subtracted UFP estimates should be carefully interpreted within the context of the presented 95% CIs.

4. Conclusions

This study reports UFP and $PM_{2.5}$ concentration and respiratory exposure among four transportation modes on an urban residential street in Santa Monica, CA. Median UFP concentrations ranged $1-3 \times 10^4$ particles cm^{-3}, were 70% lower in afternoon or evening periods compared to the morning, and were 60% lower when driving with windows closed. For each session, median $PM_{2.5}$ ranged 2–15 μg m^{-3}, which is well below the annual National Ambient Air Quality standard of 15 μg m^{-3}. UFP respiratory exposure per roundtrip, relative to driving with windows closed, was ~2 times higher while driving with windows open, ~15 times higher when cycling, and ~30 times higher walking.

During the morning period, wind speed was low with no predominant direction. These low mixing conditions may have explained the elevated pollutant concentrations reported. During afternoon and evening periods, the wind speed was higher and was predominantly southwesterly – parallel to Ocean Park. Higher UFP levels were observed on the roadway under parallel wind when vehicular emissions were isolated within the roadway environment. As a result of a Santa Ana wind episode, the wind direction for one evening session was northwesterly perpendicular, and on-roadway influences were more transient. However, likely due to off-roadway sources not on Ocean Park, there was an absolute 80% UFP increase. The only significant roadway design factor was roadway grade, but explained only ~20% of the observed UFP variability.

In order to account for emissions from higher and lower emitting vehicles, a parameter called emissions-weighted traffic volume was calculated using gravimetric PM emission factors of six classes of high-emitting vehicles. A second-order polynomial relationship was found from beach-site-subtracted UFP versus emissions-weighted traffic volume for walking mode data under parallel wind conditions ($R^2 = 0.61$). The model predicted on-roadway UFP reductions as a result of three plausible policies reducing vehicle emissions. First, a 31% reduction is predicted if all diesel trucks meet California 2007 MY PM standards. Second, a 36% reduction is predicted if one-quarter of the personal traffic volume is removed (e.g. increased usage of public transit, cycling, or walking or trip consolidation). Third, a total 68% reduction is predicted if the remaining three-quarters of the high-emitting light-duty vehicles (pre-1978) were substituted with fleet-average vehicles. With simultaneous adoption of these three plausible policies, the model predicts an 83% reduction of on-roadway UFPs.

Acknowledgments

This work was partially supported by California Air Resources Board under contract number 11-312. The authors thank the graduate students in the UCLA Luskin School of Public Affairs Chen Liu, Lu Lu, and Jinghua Suo for assistance in the field.

References

Briggs, D.J., de Hoogh, K., Morris, C., Gulliver, J., 2008. Effects of travel mode on exposures to particulate air pollution. Environment International 34, 12–22.

Brown, D.M., Wilson, M.R., MacNee, W., Stone, V., Donaldson, K., 2001. Size-dependent proinflammatory effects of ultrafine polystyrene particles: a role for surface area and oxidative stress in the enhanced activity of ultrafines. Toxicology and Applied Pharmacology 175, 191–199.
California Air Resources Board, E.P.A., 2002. Fleet Rule for Transit Agencies: Urban Bus Requirements.
California Air Resources Board, E.P.A., 2006. Facts About the California Air Resources Board's Waste Collection Vehicle Regulation.
California Air Resources Board, E.P.A., 2011. Facts About Truck and Bus Regulation School Bus Provisions.
Cicero-Fernândez, P., Long, J.R., Winer, A.M., 1997. Effects of grades and other loads on on-road emissions of hydrocarbons and carbon monoxide. Journal of the Air & Waste Management Association 47, 898–904.
Dwyer, H., Ayala, A., Zhang, S., Collins, J., Huai, T., Herner, J., Chau, W., 2010. A study of emissions from a Euro 4 light duty diesel vehicle with the European particulate measurement programme. Atmospheric Environment 44, 3469–3476.
Fruin, S., Westerdahl, D., Sax, T., Sioutas, C., Fine, P.M., 2008. Measurements and predictors of on-road ultrafine particle concentrations and associated pollutants in Los Angeles. Atmospheric Environment 42, 207–219.
Geller, M.D., Sardar, S.B., Phuleria, H., Fine, P.M., Sioutas, C., 2005. Measurements of particle number and mass concentrations and size distributions in a tunnel environment. Environmental Science & Technology 39, 8653–8663.
Hämeri, K., Koponen, I.K., Aalto, P.P., Kulmala, M., 2002. The particle detection efficiency of the TSI-3007 condensation particle counter. Journal of Aerosol Science 33, 1463–1469.
Hinds, W.C., 1999. Aerosol Technology: Properties, Behavior, and Measurement of Airborne Particles, second ed. Wiley, New York.
Int Panis, L., de Geus, B., Vandenbulcke, G., Willems, H., Degraeuwe, B., Bleux, N., Mishra, V., Thomas, I., Meeusen, R., 2010. Exposure to particulate matter in traffic: a comparison of cyclists and car passengers. Atmospheric Environment 44, 2263–2270.
Kendrick, C., Moore, A., Haire, A., Bigazzi, A., Figliozzi, M., Monsere, C., George, L., 2011. Impact of bicycle lane characteristics on exposure of bicyclists to traffic-related particulate matter. Transportation Research Record: Journal of the Transportation Research Board 2247, 24–32.
Kim, S., Shen, S., Sioutas, C., Zhu, Y., Hinds, W.C., 2002. Size distribution and diurnal and seasonal trends of ultrafine particles in source and receptor sites of the Los Angeles Basin. Journal of the Air & Waste Management Association 52, 297–307.
Kirchstetter, W.T., Harley, R.A., Kreisberg, N.M., Stolzenburg, M.R., Hering, S.V., 1999. On-road measurement of fine particle and nitrogen oxide emissions from light- and heavy-duty motor vehicles. Atmospheric Environment 33, 2955–2968.
Lee, E.S., Polidori, A., Koch, M., Fine, P.M., Mehadi, A., Hammond, D., Wright, J.N., Miguel, A.H., Ayala, A., Zhu, Y., 2013. Water-based condensation particle counters comparison near a major freeway with significant heavy-duty diesel traffic. Atmospheric Environment 68, 151–161.
Molnár, P., Janhäll, S., Hallquist, M., 2002. Roadside measurements of fine and ultrafine particles at a major road north of Gothenburg. Atmospheric Environment 36, 4115–4123.
Morawska, L., Thomas, S., Gilbert, D., Greenaway, C., Rijnders, E., 1999. A study of the horizontal and vertical profile of submicrometer particles in relation to a busy road. Atmospheric Environment 33, 1261–1274.
NIOSH, 1987. Guidance for Indoor Air Quality Investigations. NIOSH, Cincinnati.
Park, S.S., Kozawa, K., Fruin, S., Mara, S., Hsu, Y.-K., Jakober, C., Winer, A., Herner, J., 2011. Personal communication regarding future work related to: "Emission factors for high-emitting vehicles based on on-road measurements of individual vehicle exhaust with a mobile measurement platform". Journal of the Air & Waste Management Association 61, 1046–1056.
Pierson, W.R., Gertler, A.W., Robinson, N.F., Sagebiel, J.C., Zielinska, B., Bishop, G.A., Stedman, D.H., Zweidinger, R.B., Ray, W.D., 1996. Real-world automotive emissions — summary of studies in the Fort McHenry and Tuscarora Mountain Tunnels. Atmospheric Environment 30, 2233–2256.
Quiros, D.C., Zhang, Q., Choi, W., He, M., Paulson, S.E., Winer, A.M., Wang, R., Zhu, Y., 2013. Air quality impacts of a scheduled 36-h closure of a major highway. Atmospheric Environment 67, 404–414.
Rank, J., Folke, J., Homann Jespersen, P., 2001. Differences in cyclists and car drivers exposure to air pollution from traffic in the city of Copenhagen. Science of The Total Environment 279, 131–136.
Small, K.A., Kazimi, C., 1995. On the costs of air-pollution from motor-vehicles. Journal of Transport, Economics and Policy 29, 7–32.
Strak, M., Boogaard, H., Meliefste, K., Oldenwening, M., Zuurbier, M., Brunekreef, B., Hoek, G., 2010. Respiratory health effects of ultrafine and fine particle exposure in cyclists. Occupational and Environmental Medicine 67, 118–124.
US Census, 2010. American FactFinder, United States Census Bureau.
Vinzents, P.S., Moller, P., Sorensen, M., Knudsen, L.E., Hertel, O., Jensen, F.P., Schibye, B., Loft, S., 2005. Personal exposure to ultrafine particles and oxidative DNA damage. Environmental Health Perspectives 113, 1485–1490.
Wallace, L., Ott, W., 2011. Personal exposure to ultrafine particles. Journal of Exposure Science and Environmental Epidemiology 21, 20–30.
Weichenthal, S., Dufresne, A., Infante-Rivard, C., Joseph, L., 2008. Determinants of ultrafine particle exposures in transportation environments: findings of an 8-month survey conducted in Montreal, Canada. Journal of Exposure Science and Environmental Epidemiology 18, 551–563.
Westerdahl, D., Fruin, S., Sax, T., Fine, P.M., Sioutas, C., 2005. Mobile platform measurements of ultrafine particles and associated pollutant concentrations on freeways and residential streets in Los Angeles. Atmospheric Environment 39, 3597–3610.
Wichmann, H.-E., Peters, A., 2000. Epidemiological evidence of the effects of ultrafine particle exposure. Philosophical Transactions of the Royal Society of London. Series A: Mathematical, Physical and Engineering Sciences 358, 2751–2769.
Xu, B., Zhu, Y., 2009. Quantitative analysis of the parameters affecting in-cabin to on-roadway (I/O) ultrafine particle concentration ratios. Aerosol Science and Technology 43, 400–410.
Yanosky, J.D., Williams, P.L., MacIntosh, D.L., 2002. A comparison of two direct-reading aerosol monitors with the federal reference method for PM2.5 in indoor air. Atmospheric Environment 36, 107–113.
Zhang, Q., Zhu, Y., 2010. Measurements of ultrafine particles and other vehicular pollutants inside school buses in South Texas. Atmospheric Environment 44, 253–261.
Zheng, M., Cass, G.R., Schauer, J.J., Edgerton, E.S., 2002. Source apportionment of PM2.5 in the southeastern United States using solvent-extractable organic compounds as tracers. Environmental Science & Technology 36, 2361–2371.
Zhu, Y.F., Hinds, W.C., Kim, S., Sioutas, C., 2002. Concentration and size distribution of ultrafine particles near a major highway. Journal of the Air & Waste Management Association 52, 1032–1042.
Zhu, Y., Eiguren-Fernandez, A., Hinds, W.C., Miguel, A.H., 2007. In-cabin commuter exposure to ultrafine particles on Los Angeles freeways. Environmental Science & Technology 41, 2138–2145.